

UNIVERSITY OF NAPLES FEDERICO II

Department of Structures
for Engineering and Architecture

Ph.D. Programme in Materials and Structures
XXVI Cycle



VINCENZO GIAMUNDO

Ph.D. Thesis

SEISMIC ASSESSMENT AND RETROFIT OF HISTORICAL MASONRY BARREL VAULTS

TUTORS: PROF. GIAN PIERO LIGNOLA
PROF. GAETANO MANFREDI

2014

“Per aspera sic itur ad astra”
Seneca, Hercules furens, act II, v.437

Acknowledgements

Before all, I would like to express my deepest gratitude to Prof. Gian Piero Lignola. I am very grateful to him for his encouragement, interest, stimulus and guidance. It was mainly due to his initiatives, valuable instructions and constant help that the development of this work has been possible. Special thanks go to both Prof. Gaetano Manfredi and Prof. Andrea Prota for giving me the chance to be part of such outstanding research group. I would like to thank Prof. Stephen Garrity for his support and precious advices during my time spent at the University of Leeds.

Furthermore, I would like to acknowledge all the people with whom I collaborated during these years, in particular: Prof. Edoardo Cosenza, Prof. Giuseppe Maddaloni, Prof. Francesca da Porto, Prof. Yong Sheng, Dr. Vasilis Sarhosis, Prof. Gianluigi De Martino and Prof. Renata Picone.

I would like to acknowledge past and present PhD colleagues and all the members of staff at the Department of Structures for Engineering and Architecture at the University of Naples Federico II. In particular my officemates: Alberto Zinno, Andrea Calabrese, Anna Bozza, Claudio D'Ambra, Concetta Onorii, Daniele Losanno, Eugenio Chioccarelli, Giancarlo Ramaglia, Loredana Napolano and Raffaele Frascadore. Thank you guys for your precious help!

I wish to express my gratitude to my good friends Barbara Polidoro, Carmine Galasso, Michele Franzese, Emiliano and Peppe Petix who directly or indirectly helped me during this period. I would also like to thank my colleagues and friends at the University of Leeds whom provided friendly cooperation and useful discussions throughout my time in Leeds; I would particularly like to mention: Abdulrahman Bashawri, Rachel Albinson, Guy Brackenbury, Omar Alzayani, Kalhed, Laura Davis, Silvia Purin, Alessia Perego, Liting Lin, Anton Dmitriev, Marion Goemans and Chin Wei Lim.

Special thanks are due to my family for their constant support, love, and encouragement. Finally, I would like to thank Silvia for her sacrifice and for having shared my successes and disappointments. Without their full support and encouragement, this thesis would not have been completed.

Vincenzo Giamundo

Abstract

Recent earthquakes in Italy highlighted the extreme vulnerability of historical buildings. Masonry vaults, which represent artistic valuable elements, have been recognised as the most vulnerable elements of such buildings. Therefore, the knowledge of their seismic performances, as well as potential retrofit techniques, meets the need to protect cultural heritage buildings which are prone to natural hazards. Vault dynamic behaviour is generally studied according to simplified methods or, as an alternative, to complex Finite Element (FE) analyses. However, a deep knowledge of their dynamic behaviour is still lacking from an experimental point of view. In order to investigate the seismic behaviour of masonry vaults, shaking table tests have been performed of a full scale masonry barrel vault. After the tests, the vault has been retrofitted by means of mortar joint repointing, grout injections and Inorganic Matrix FRP Grid (IMG). Then shaking table tests have been performed on the retrofitted vault. By means of the experimental tests outcomes, reliable numerical models able to predict the dynamic behaviour of the masonry vault (before and after the retrofit) have been developed. This aspect is relevant for studying characteristics which cannot be investigated by means of the experimental test monitoring. In this thesis a comprehensive overview of the main results of the experimental tests is reported. The unreinforced vault exhibits a good seismic behaviour, showing very slight damage up to a horizontal acceleration of about 4.8 m/s^2 (measured at the keystone location). The retrofit resulted in a significant increase of both stiffness and capacity. Indeed, very slight damages only after the last test (performed with an achieved PGA of 11.70 m/s^2) were detected on the retrofitted vault. However the retrofit did not drastically change the global dynamic behaviour of the vault.

KEYWORDS: •*Seismic Assessment* •*Masonry Vaults* •*Seismic Retrofit* •*Dynamic Tests* •*FEM Analysis*.

Table of Contents

Abstract.....	1
Table of Contents	1
List of Tables	4
List of Figures.....	5
Chapter 1 Introduction.....	10
1.1. General context	10
1.2. Research significance.....	13
1.3. Outline of the thesis	14
Chapter 2 Literature review.....	15
2.1 Brief historical overview of the masonry curved elements.....	16
2.2 Arch static analysis methods.....	19
2.2.1 Equilibrium methods.....	19
2.3 Arch dynamic analysis methods.....	25
2.3.1 Finite Element Method (FEM) analysis	26
2.4 Retrofit of historical buildings	27
2.4.1 Retrofit of vaulted structures.....	28
2.4.2 Overview on the main retrofit techniques for the vaults	30
2.4.2.1 Innovative retrofit techniques.....	38
2.5 Experimental studies	44
2.5.1 Tests on reinforced arches and vaults	45
Chapter 3 Experimental tests: unreinforced vault.....	52
3.1 Specimen.....	53
3.1.1 Material characterization	55

3.2	Experimental facilities	58
3.3	Testing structure.....	59
3.3.1	Testing frame design.....	60
3.3.2	Lifting structure design	70
3.4	Instrumentation	75
3.5	Input and test programme.....	77
3.6	Outcomes of the shaking table tests	81
3.6.1	RND test results (Dynamic identification).....	81
3.6.2	STR test results (Sturmo earthquake)	82
3.6.3	ART test results (artificial earthquake).....	88
3.7	Conclusions	96
Chapter 4	Experimental tests: retrofitted vault	97
4.1	Specimen retrofit.....	98
4.2	Instrumentation	102
4.3	Input and test programme.....	103
4.4	Outcomes of the shaking table tests	106
4.4.1	RND_R test results (Dynamic identification)	106
4.4.2	ART_R test results (artificial earthquake)	108
4.5	Outcomes comparison: retrofitted/unreinforced vault	119
4.5.1	Dynamic characteristics	119
4.5.2	Maximum acceleration profiles	122
4.5.3	Dynamic amplification profiles	124
4.6	Conclusions	126
Chapter 5	Numerical modelling.....	128
5.1	FE Models.....	129

5.1.1	Modelling of the retrofit interventions	134
5.2	Calibration of the model.....	137
5.2.1	Calibration of the interface stiffness	137
5.2.2	Calibration of the interface cohesion	139
5.3	Dynamic linear analyses	143
5.3.1	Unreinforced vault	143
5.3.2	Retrofitted vault	146
5.4	Static nonlinear analyses	149
5.4.1	Unreinforced vault	149
5.4.2	Retrofitted vault	152
5.5	Dynamic nonlinear analyses	155
5.5.1	Rayleigh damping coefficients.....	156
5.5.2	Input signals	159
5.5.3	Unreinforced vault: experimental-numerical comparison.....	162
5.5.4	Retrofitted vault: experimental-numerical comparison.....	164
5.6	Influence of the damage on the numerical results.....	167
5.6.1	ART7: experimental-numerical comparison.....	168
5.6.2	ART7_R: experimental-numerical comparison	170
5.6.3	Parametric analyses (damping influence)	172
5.7	Conclusions	175
Chapter 6	Conclusions	177
References	181
Appendix A	188
Appendix B	193
Appendix C	195

List of Tables

Table 3.1: Material mechanical properties.....	56
Table 3.2: Experimental test programme (unreinforced vault).....	80
Table 3.3: Natural frequencies and damping ratios (unreinforced vault).....	82
Table 3.4: STR test results: horizontal maximum accelerations.....	85
Table 3.5: STR test results: vertical maximum accelerations.....	85
Table 3.6: STR test results: dynamic amplifications.....	87
Table 3.7: STR test results: maximum relative displacements.....	87
Table 3.8: ART test results: horizontal maximum accelerations.....	90
Table 3.9: ART test results: vertical maximum accelerations.....	91
Table 3.10: ART test results: dynamic amplifications.....	92
Table 3.11: ART test results: maximum relative displacements.....	93
Table 4.1: Experimental test programme pt. 1 (retrofitted vault).....	104
Table 4.2: Experimental test programme pt. 2 (retrofitted vault).....	105
Table 4.3: Natural frequencies and damping ratios (retrofitted vault).....	107
Table 4.4: ART_R test results: horizontal maximum accelerations.....	110
Table 4.5: ART_R test results: vertical maximum accelerations.....	111
Table 4.6: ART_R test results: dynamic amplifications.....	113
Table 4.7: ART_R test results: maximum relative displacements.....	114
Table 5.1: Interface elements properties.....	133
Table 5.2: IMG mechanical properties.....	136
Table 5.3: Unreinforced vault: modal properties.....	145
Table 5.4: Retrofitted vault: modal properties.....	148
Table 5.5: Unreinforced vault: Rayleigh coefficients.....	158
Table 5.6: Retrofitted vault: Rayleigh coefficients.....	158

List of Figures

Figure 1.1 Example of vaults damaged: (a) Emilia-Romagna Earthquake (2012) [2]; (b), (c) and (d) L’Aquila earthquake (2009) [2, 3];	11
Figure 2.1 Arch as a subdivision of stone beams into smaller single elements [10].....	16
Figure 2.2 Arches in Roman architecture: (a) Colosseum; (b) Segovia’s aqueduct	17
Figure 2.3 Vaulted structure in Romanesque architecture [12]	17
Figure 2.4 Gothic architecture: (a) Cathedral; (b) Flying buttress	18
Figure 2.5 Forces through arches [18]	20
Figure 2.6 Sketch of the thrusts in a generic masonry arch	21
Figure 2.7 Hanging chain (catenaria).....	22
Figure 2.8 Graphical method by Snell [32]	23
Figure 2.9 Graphical methods by Huerta [30]	24
Figure 2.10 Masonry arch model under horizontal load [36]	25
Figure 2.11 Typical four hinges mechanism due to vertical load [49].....	30
Figure 2.12 Example of ordinary buttresses [50].....	31
Figure 2.13 Typologies of buttress through the history: (a), (b), (c), (d) ordinary buttress; (e) flying buttress [12].....	32
Figure 2.14 Tying scheme for a two span vaulted ceiling [50].....	33
Figure 2.15 Examples of curved element retrofit by means of ties of ties: (a) steel; (b) wood ..	34
Figure 2.16 Reinforced concrete jacketing at the extrados of the vault	36
Figure 2.17 Examples of grout injections [53]	36
Figure 2.18 Mortar joint repointing process: (a) Joint after cleaning; (b) detail of the joint depth; (c) joint’s repointing; (d) after intervention [56].	37
Figure 2.19 Detail of the anchorage of the cable to the extrados [57]	39
Figure 2.20 Force interaction between the cable (in tension) and the vault (in compression): (a) reinforcement at the extrados; (b) reinforcement at the intrados [58].....	39
Figure 2.21 Bed joint NSM reinforcement for a masonry representative element [61].....	40
Figure 2.22 Possible retrofit layouts for barrel vaults [62]	41
Figure 2.23 Debonding in curved structures [62]	42
Figure 2.24 IMG retrofit system scheme	43
Figure 2.25 Geometry of the specimens and load conditions [63].....	45
Figure 2.26 Reinforcement configuration [68]	46
Figure 2.27 Extrados of the vault after the intervention [46].....	47
Figure 2.28 Experimental test setup [71]	49
Figure 2.29 Experimental test setup [72]	49
Figure 2.30 Experimental test setup [73]	50
Figure 3.1 Geometry of the specimen: 3D view	53

List of Figures

Figure 3.2 Geometry of the specimen: plan and section views (dimension in cm).....	54
Figure 3.3 Specimen during construction phases: (a) polystyrene centring; (b) construction of the imposts; (c) curved element construction; (d) specimen completed	55
Figure 3.4 Material characterization: mortar specimen preparation	57
Figure 3.5 Earthquake simulator system (ESS) scheme	58
Figure 3.6 Testing structure overview	59
Figure 3.7 FE model of the specimen	61
Figure 3.8 Static nonlinear analyses results: horizontal load multiplier-base reacting forces (horizontal and vertical).....	62
Figure 3.9 Static nonlinear analyses results: horizontal load multiplier-displacement curves....	62
Figure 3.10 Geometry of the steel plane frame (plan and laterals view)	63
Figure 3.11 Detail of the U shaped beam	65
Figure 3.12 Calculation scheme: simple supported beam with uniformly distributed load	65
Figure 3.13 Detail of the H shaped beam	66
Figure 3.14 Calculation scheme: cantilever beam with point load	66
Figure 3.15 detail of the bolted connection: 3D view	68
Figure 3.16 Force acting on the single bolted connection	69
Figure 3.17 Bolt holes spacing reference scheme	69
Figure 3.18 Connections between the lifting structure and the testing frame	71
Figure 3.19 FEM model of the lifting/moving system.....	72
Figure 3.20 Calculation scheme: simply supported beam with point load	73
Figure 3.21 Detail of the Lifting pipe-plate class A connection: 3D view	74
Figure 3.22 Instrumentation layout: plan view (dimensions in cm)	76
Figure 3.23 Instrumentation layout: front view (dimensions in cm).....	77
Figure 3.24 Time-history accelerograms at 100% intensity: (a) STR; (b) ART;.....	78
Figure 3.25 Time-history accelerograms at 100%: (a) FFT STR; (b) FFT ART.	79
Figure 3.26 Test setup and specimen: shaking direction (unreinforced vault).	80
Figure 3.27 Natural frequency decay of the specimen (unreinforced vault).	81
Figure 3.28 Sturmo earthquake, test STR4: recorded time-history in acceleration at the impost (in black) and keystone (in grey) of the vault (a) and relative keystone-impost displacement (b).	83
Figure 3.29 STR: Maximum acceleration profiles (values expressed in m/s^2).	84
Figure 3.30 STR: Horizontal dynamic amplifications (values expressed in %).	86
Figure 3.31 Artificial earthquake, test ART7: (a) recorded time-history in acceleration at the impost (in black) and keystone (in grey) of the vault; (b) relative keystone-impost displacement.	88
Figure 3.32 ART: Maximum acceleration profiles (values expressed in m/s^2).	89
Figure 3.33 ART: Horizontal dynamic amplifications (values expressed in %).	91
Figure 3.34 Unreinforced vault: damages detected (intrados)	94

List of Figures

Figure 3.35 Unreinforced vault: damages detected (extrados)	95
Figure 4.1 Repointing of the cracked joints at the front of the vault.	98
Figure 4.2 Repointing of the cracked joints at the intrados of the vault	99
Figure 4.3 Grout injections at the extrados of the vault	100
Figure 4.4 IMG system at the extrados of the vault	101
Figure 4.5 Resume of the retrofit process: (a) Repointing of the cracked joints at the intrados; (b) Grout injections at the extrados; (c) Grid installing layer at the extrados.	102
Figure 4.6 Test setup and specimen: shaking direction (retrofitted vault).	103
Figure 4.7 Natural frequency decay of the specimen (retrofitted vault).	107
Figure 4.8 Artificial earthquake, test ART7_R: (a) recorded time-history in acceleration at the impost (in black) and keystone (in grey) of the vault; (b) relative keystone-impost displacement.	108
Figure 4.9 ART_R: Maximum acceleration profiles (values expressed in m/s^2).	109
Figure 4.10 ART_R: Horizontal dynamic amplifications (values expressed in %).	112
Figure 4.11 Retrofitted vault: damages detected (front view).	116
Figure 4.12 Retrofitted vault: damages detected (rear view)	117
Figure 4.13 Retrofitted vault: damages detected (intrados)	118
Figure 4.14 Natural frequency comparison: retrofitted vault/unreinforced vault	120
Figure 4.15 Comparison: frequency decay-achieved PGA trends	121
Figure 4.16 Comparison: damping ratios-achieved PGA trends.....	122
Figure 4.17 Achieved input signals FFT: (a) ART2; (b) ART2_R.....	123
Figure 4.18 Maximum acceleration profiles comparison: ART2-ART2_R (values expressed in m/s^2).....	124
Figure 4.19 Dynamic amplification profiles comparison: ART2-ART2_R (values expressed in %).	125
Figure 5.1 Masonry vault FE model.	129
Figure 5.2 Masonry vault FE model: detail of the adopted mesh.	130
Figure 5.3 CQ16M element [80].....	131
Figure 5.4 CL12I element: (a) topology; (b) displacement [80]	131
Figure 5.5 Nonlinear elastic friction model [80].....	132
Figure 5.6 Truss element: (a) characteristics; (b) axes [80].....	135
Figure 5.7 IMG constitutive models adopted: (a) grid; (b) matrix.....	136
Figure 5.8 Calibration of the interface stiffness: interface stiffness-natural frequency curve ..	138
Figure 5.9 Vertical load test: instrumentation and load layout	140
Figure 5.10 Vertical load test: (a) loading phase; (b) maximum load.....	140
Figure 5.11 Vertical load test: experimental load-displacement curves	141
Figure 5.12 Calibration of the interface cohesion: numerical load-displacement curves	142
Figure 5.13 Calibration of the interface cohesion: numerical-experimental comparison	143
Figure 5.14 Unreinforced vault: modal shapes (mode 1-4)	144

List of Figures

Figure 5.15 Unreinforced vault: modal shapes (mode 5-10)	146
Figure 5.16 Retrofitted vault: modal shapes (mode 1-4)	147
Figure 5.17 Retrofitted vault: modal shapes (mode 5-10)	147
Figure 5.18 Static nonlinear analysis: unreinforced vault load-displacement curve.....	150
Figure 5.19 Static nonlinear analysis: unreinforced vault principal stresses in tension (values expressed in MPa).....	150
Figure 5.20 Static nonlinear analysis: unreinforced vault principal stresses in compression (values expressed in MPa)	151
Figure 5.21 Static nonlinear analysis: unreinforced vault stresses and enlargements of joint openings at the interfaces (values expressed in MPa).....	152
Figure 5.22 Static nonlinear analysis: retrofitted vault load-displacement curve	153
Figure 5.23 Static nonlinear analysis: retrofitted vault principal stresses in tension (values expressed in MPa).....	154
Figure 5.24 Static nonlinear analysis: retrofitted vault principal stresses in compression (values expressed in MPa).....	154
Figure 5.25 Static nonlinear analysis: retrofitted vault stresses and stresses and enlargements of joint openings at the interfaces (values expressed in MPa)	155
Figure 5.26 Variation of damping ratio with natural frequency	159
Figure 5.27 ART2: (a) time-history accelerogram; (b) elastic spectrum	160
Figure 5.28 ART7: (a) time-history accelerogram; (b) elastic spectrum	160
Figure 5.29 ART2_R: (a) time-history accelerogram; (b) elastic spectrum.....	161
Figure 5.30 ART7_R: (a) time-history accelerogram; (b) elastic spectrum.....	161
Figure 5.31 ART15_R: (a) time-history accelerogram; (b) elastic spectrum.....	161
Figure 5.32 Experimental-numerical comparison test ART2: Maximum acceleration profiles (values expressed in m/s^2).....	162
Figure 5.33 Experimental-numerical comparison test ART2: Dynamic amplification profiles (values expressed in %).	163
Figure 5.34 ART2: numerical force-displacement trend	164
Figure 5.35 Experimental-numerical comparison test ART2_R: Maximum acceleration profiles (values expressed in m/s^2).....	165
Figure 5.36 Experimental-numerical comparison test ART2_R: Dynamic amplification profiles (values expressed in %).	165
Figure 5.37 ART2_R: numerical force-displacement trend.....	166
Figure 5.38 Experimental-numerical comparison test ART7: Maximum acceleration profiles (values expressed in m/s^2).....	168
Figure 5.39 Experimental-numerical comparison test ART7: Dynamic amplification profiles (values expressed in %).	169
Figure 5.40 ART7: numerical force-displacement trend	169

List of Figures

Figure 5.41 Experimental-numerical comparison test ART7_R: Maximum acceleration profiles (values expressed in m/s^2).....	170
Figure 5.42 Experimental-numerical comparison test ART7_R: Dynamic amplification profiles (values expressed in %).	171
Figure 5.43 ART7_R: numerical force-displacement trend.....	171
Figure 5.44 ART15_R: experimental (in black) and numerical 2.8% damping (in grey).....	173
Figure 5.45 ART15_R: experimental (in black) and numerical 5% damping (in grey).....	173
Figure 5.46 ART15_R: experimental (in black) and numerical 10% damping (in grey).....	173
Figure 5.47 Experimental-numerical comparison test ART15_R: Maximum acceleration profiles (values expressed in m/s^2)	174
Figure 5.48 Experimental-numerical comparison test ART15_R: Dynamic amplification profiles (values expressed in %)	175

Chapter 1

Introduction

1.1. General context

Masonry is the generic term for a composite material made of a large number of separate small elements bonded together by some binding filler in many different arrangements. The quality of the bond, materials used, workmanship and the masonry textures significantly affect the mechanical performance of the overall masonry structure. For these reasons, the prediction of masonry behaviour is generally extremely hard.

Masonry constructions were widespread in the ancient world, and masonry is one of the most used materials in ancient times. Furthermore the most of the European cultural heritage buildings are constituted by masonry. Despite their past and present spread, and their long existence, masonry constructions are prone to damage under seismic actions. Moreover, a relevant part of these buildings are located in areas of high seismic risk.

Recent earthquakes in Italy (Umbria and Marche, 1997-1998; L'Aquila, 2009; Emilia Romagna, 2012) have produced significant damages to several historical and cultural heritage sites [1]. In many of these historical buildings the vertical masonry elements were connected by means of curved elements, such as arches or vaults. The inspections of the damaged building, after the earthquakes (e.g. San Paolo Cathedral in Mirabello, San Francesco church complex in Assisi, Estense Fortress in Finale Emilia [1]), have shown that masonry arches and vaults are the most critical elements in the seismic vulnerability of such structures (Figure 1.1).

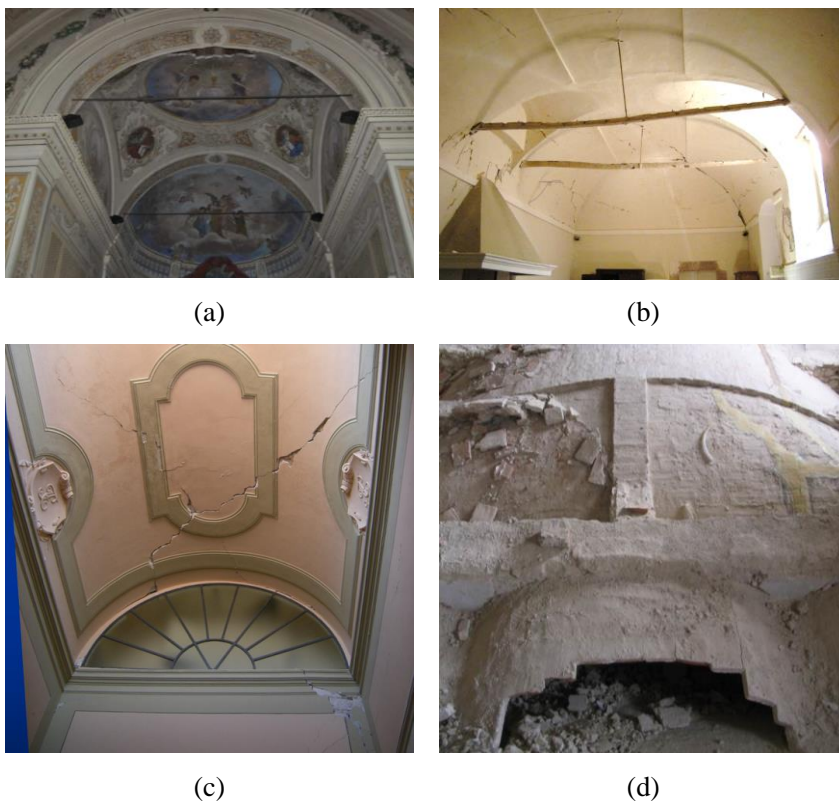


Figure 1.1 Example of vaults damaged: (a) Emilia-Romagna Earthquake (2012) [2];
(b), (c) and (d) L'Aquila earthquake (2009) [2, 3];

Therefore, the preservation and, in particular, the retrofit of curved masonry structural elements is a crucial structural issue.

Recent developments in materials, manufacturing, mechanics and design of composite materials allowed the growth of such materials as retrofit of masonry elements.

In the last years the most of composites strengthening research has involved fibre reinforced polymers (FRP). However, resin-based composites have shown several drawbacks such as: inappropriate bond to existing masonry substrates, flammability, sensitivity to high temperatures and moisture permeability [4]. Such problems can be overcome by innovative applications which involve inorganic matrix composite grids (IMG). Cement based matrixes are, indeed, highly compatible to the masonry substrate in terms of bond, moisture permeability, and thermal properties preventing therefore the main critical issues [5]. These retrofit techniques applied to masonry elements have demonstrated to significantly improve the stiffness, ductility and the ultimate strength, preventing the element from a brittle collapse [6-8].

So far, however comprehensive knowledge on the effectiveness of such retrofit applied to masonry vault elements under dynamic load is still lacking.

In this thesis, the dynamic behaviour of both unreinforced and retrofitted masonry vault elements has been investigated. The vault has been retrofitted by means of mortar joint repointing, grout injections and IMG. Moreover, the experimental data allowed developing reliable numerical models able to predict the dynamic behaviour of masonry vault (before and after the retrofit).

1.2. Research significance

Masonry is the simplest construction material. Despite its straightforwardness, however, the seismic behaviour of masonry structures is hard to predict. In many masonry buildings, the vertical elements are connected by means of curved elements, such as arches or barrel vaults. Furthermore the vaults represent an artistic valuable element in the historical heritage buildings. Consequently, the understanding of their seismic performance, as well as potential retrofit techniques, meets also the need to protect cultural heritage buildings against earthquakes. Nowadays, however, a better knowledge on the dynamic behaviour of masonry vaulted elements is still a need. These motivating factors provide the purposes of this thesis, which are:

- improving the knowledge on the dynamic behaviour of masonry vaulted elements;
- studying the impact of innovative retrofit techniques such as IMG on the dynamic behaviour of masonry vaulted elements;
- developing reliable numerical models able to predict the dynamic behaviour of masonry vaults (before and after the retrofit)

In order to achieve this goal a multi-scale approach has been adopted. Both experimental shaking table tests and numerical analyses have been performed on the vault before and after the retrofit. In order to calibrate the numerical models, further experimental vertical load tests been performed.

1.3. Outline of the thesis

The thesis has been structured into 5 chapters, included the *Chapter 1*, which briefly introduces to the general context and states the objectives and strategies adopted to achieve them. *Chapter 2* provides for a review the previous researches by means of an accurate literature review. In particular the following aspects have been treated: static and dynamic analysis methods; retrofit techniques for historical vaulted structures; previous experimental studies on the theme. In the *Chapter 3* the experimental shaking table tests on the unreinforced vault have been presented. In particular, specimen characteristics, test setup design, monitoring instrumentation and seismic inputs have been described. The test outcomes have been presented in terms of: relative displacement, maximum acceleration and dynamic amplification profiles and time histories. *Chapter 4* deals with the experimental shaking table tests on the retrofitted vault. In particular, specimen retrofit, monitoring instrumentation and seismic inputs have been described. Furthermore, a comparison between the test outcomes of reinforced and retrofitted vault has been provided. Both the test and the outcomes of comparisons have been presented in terms of: relative displacement, maximum acceleration and dynamic amplification profiles and time histories. In the *Chapter 5* is presented the finite elements modelling of the tested specimens (i.e. both unreinforced and retrofitted vaults). Micro-modelling approach has been adopted and the nonlinear characteristics of the vault have been calibrated by means of experimental tests. Dynamic linear, static nonlinear and dynamic nonlinear analyses have been performed in order to validate the numerical models. Furthermore, the influence of the damping parameters has been investigated.

Chapter 2

Literature review

Vaults are spatial three-dimensional structures which were usually built in order to provide a space with a ceiling or roof. In the history several types of vaults have been built. The simplest type of vault is the “barrel vault” which consists of a continuous ongoing series of semi-circular arches. Barrel vaults can be schematized as sum of series of elementary arches (neglecting potential mutual interaction between the arches). Thus the structural analysis of barrel vaults is practically a problem which can be solved by studying the elementary arch in its own plane [9]. Therefore, the methods developed for the arches can be expanded to three dimensions, in order to study behaviour of the barrel vaults.

Masonry arches have been studied for many centuries and several methods and tools have been developed to understand their behaviour. In the following sections a brief overview on the historical evolution of the masonry curved elements has been provided. Then the mechanical and analytical methods adopted to study the arch behaviour have been addressed.

2.1 Brief historical overview of the masonry curved elements

The use of arches and vaults is thousand years old. It exists in nature as a consequence of natural lack of tensile strength of the stones. Several theories have been formulated on how this type of structure has started to be used in architecture. Probably it has conceived as a refinement of support stone elements [10], or as a subdivision of stone beams into smaller single elements (Figure 2.1)

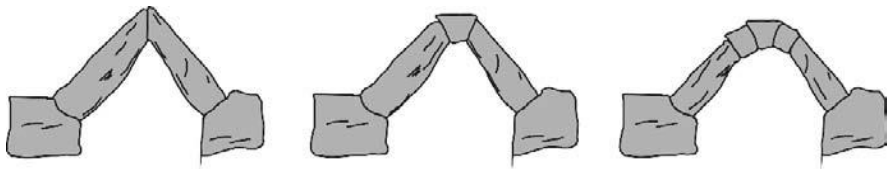


Figure 2.1 Arch as a subdivision of stone beams into smaller single elements [10]

Primitive examples of curved masonry elements date back to the prehistory. Stone arches appeared in Babylon about 6,000 years ago. The first small-span vaults, dated back about 5,000 years ago, are clear in Mesopotamic burial chambers [10, 11]. Several examples of vaults were also found in Sumerians and Old Egyptians architecture. A step forward in the development of curved elements was done during the time of the Roman Empire. In this time the placement of the stones was improved and the mortar started to be used. These improvements allowed the construction of wide-span vaults. Roman bridges, amphitheatres and aqueducts are clear example of the considerable usage of curved masonry elements in the Roman architecture (Figure 2.2).

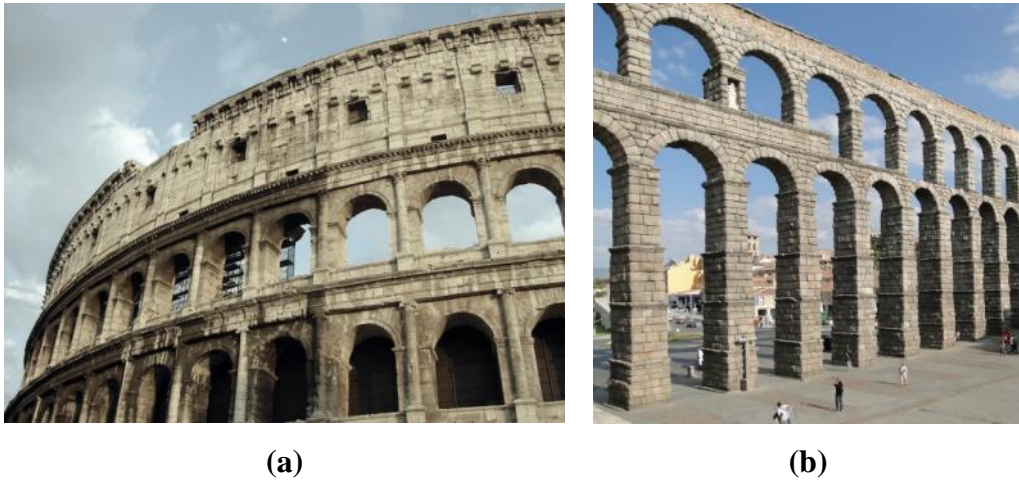


Figure 2.2 Arches in Roman architecture: (a) Colosseum; (b) Segovia's aqueduct

After the Roman Empire fall, the use of curved masonry elements was remarkable in the Byzantine architecture, where new arch typologies were developed (i.e. lancet and ogee arches). Later, during the Middle Age, in the Romanesque architecture the use of round arches and barrel vaults was massive once again (Figure 2.3).

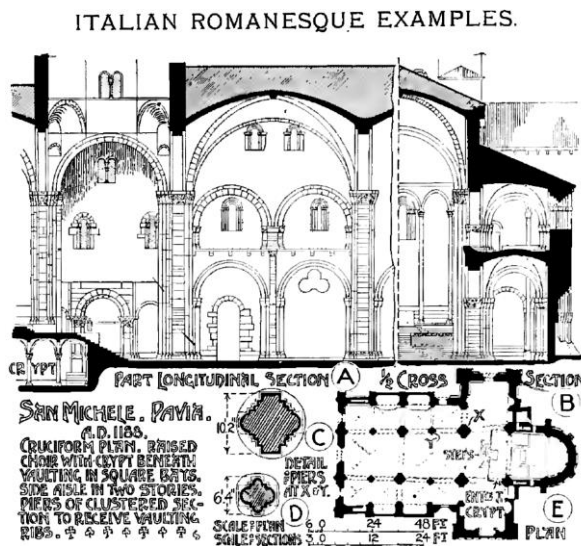


Figure 2.3 Vaulted structure in Romanesque architecture [12]

The use of vaulted structures was largely adopted in the Gothic architecture as well. In this historic period the use of curved masonry elements allowed the perfect integration of architectural and structural functions. In particular the main innovations of the use of curved masonry elements in Gothic architecture were: the use of flying buttress and the use of the pointed arch (Figure 2.4).



(a)

(b)

Figure 2.4 Gothic architecture: (a) Cathedral; (b) Flying buttress

During the Renaissance, symmetry, proportion, geometry and the regularity of parts were the main architectural points, and the application of circular segments became very popular. In the 19th centuries, due to the gradual introduction of iron and then steel, to be followed by reinforced concrete the decline of the use of masonry structures has started. Nowadays masonry constructions do not have a central role in the building trade. However their preservation and retrofit represents a challenging structural matter.

2.2 Arch static analysis methods

A large amount of literature has been published on the arch static analysis. It represents a solid base to the proper study of the arch behaviour. Since the dynamic effects are neglected, these methods are not as accurate as the modern dynamic methods are. On the other hand, they are practical and they can be applied when high computational power is not available. Therefore, these methods represent a good compromise between the approximation and computational expense.

2.2.1 Equilibrium methods

The static behaviour of masonry structures can be studied according to three simple key assumption proposed in the 1730 by Couplet [13, 14]:

- masonry has no tensile strength;
- sliding failure does not occur;
- stresses are so low that masonry compressive strength can effectively be considered unlimited.

Each one of these assumptions could not be strictly true. Therefore it must be hedged with qualifications and it must, in any case, be tested [14].

However, for historical masonry structures, the Couplet assumptions are largely acceptable in the most of the cases. Thus, they still provide the basic principles used for the masonry structural analysis [14, 15]. The analysis methods based on this assumptions are usually known as “*equilibrium methods*” [16]. Since the main field of application of these methods are the pure compression structures, they are particularly suitable, for the structural analysis of arches and vaults.

The arch is the fundamental structural element in the masonry architecture [17]. However, it is worth to briefly introduce the basic concepts of the arch

mechanical behaviour. Masonry arches are made of blocks assembled each other with or without mortar. Let us consider a masonry arch in an equilibrium configuration. Since the arch is in equilibrium, each block is in equilibrium. The equilibrium of the single block is achieved by means of the *thrusts* given by the two adjacent blocks (Figure 2.5).

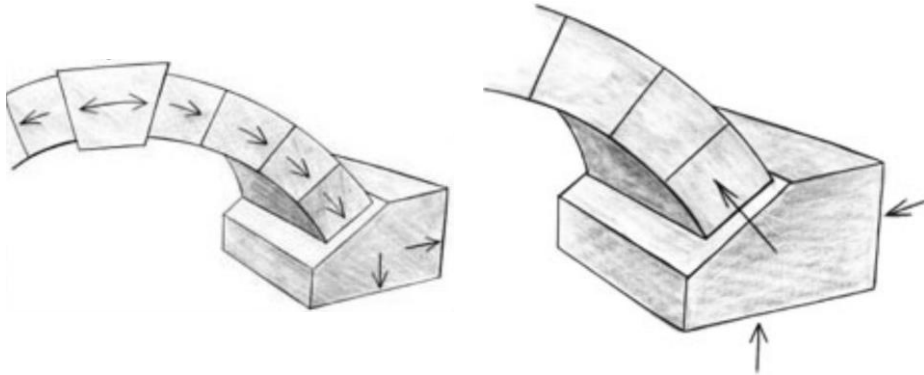


Figure 2.5 Forces through arches [18]

The thrusts are defined as the resultants of the compressive stress distributions in the joints. The point of application of any single thrust (i.e. *centre of thrust*) is contained within the plane of the joint.

The envelope of all the centres of thrust is a curve named *thrust line* (Figure 2.6). Whether all the blocks are compressed, the thrust line lies entirely within the arch boundary. Its shape depends on the arch geometry, loads and family of plane joints considered [19, 20]. Therefore the geometry of the thrust line is, actually, the shape of the ideal arch able to bear the load accounted to draw the thrust line. Nevertheless, there is not only one thrust line which guarantees the arch to be in equilibrium. In particular, to each possible thrust line lying within the arch boundaries, corresponds an equilibrium configuration of the arch.

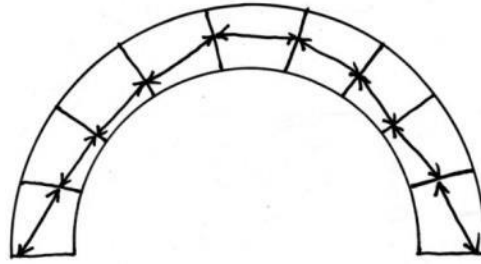


Figure 2.6 Sketch of the thrusts in a generic masonry arch

Given an arbitrary masonry arch, ideally inverting his curvature (Figure 2.7), the compression forces will become tension forces.

Thus the blocks constituent the arch, will hang like a chain [21, 22]. Therefore, according to Heyman [23] is possible to re-assert the previous statements as “...none but the catenaria is the figure of a true legitimate arch, or fornix. And when an arch of any other figure is supported, it is because in its thickness some catenaria is included”.

The solution of the equilibrium problem is not unique. Infinite thrust lines or catenaries can lie within the arch boundaries. The arch is, indeed, a hyperstatic structure. Thus the equilibrium equations are not enough to give the solution. In order to achieve the actual thrust line, statements about both material properties and boundary condition are required. Applying the elastic analysis (equilibrium, congruence and compatibilities equations) it is possible to achieve the stresses in the arch [23-26]. However, the resultant equation system found applying the elastic analysis is highly sensitive to small changes in boundary conditions (i.e. hinges formation) [14, 17].

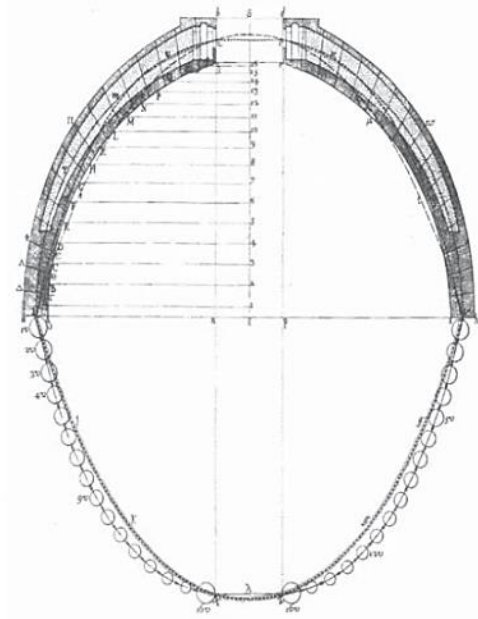


Figure 2.7 Hanging chain (catenaria)

Furthermore, even if small cracks are not dangerous for the safety of masonry structure, they determine changes in the position of the thrust line. These arguments make clear that the assessment of the actual thrust line is impossible. However, according to the safe theorem of the limit analysis [23, 27, 28] it is unnecessary to achieve of the actual thrust line. In fact, if it is possible to find an internal system of forces, in equilibrium with the loads, which does not violate material assumptions, the structure will not collapse. Therefore the existence of a thrust line (equilibrium) within the boundary of the arch (no-tensile material) is a sufficient condition of stability for a masonry arch.

The equilibrium methods to achieve the thrust line in a masonry arch have been developed both in graphical and in numerical way. Graphical methods, which have been used for centuries [29, 30], are nowadays considered time consuming and laborious. Some examples of graphical methods used for the assessment of

the arch analysis are proposed in [30-34]. In particular in [32] the thrust line (the red line in Figure 2.8), is drawn by means of the force polygon. Lying the thrust line within the arch boundaries the arch stability is achieved.

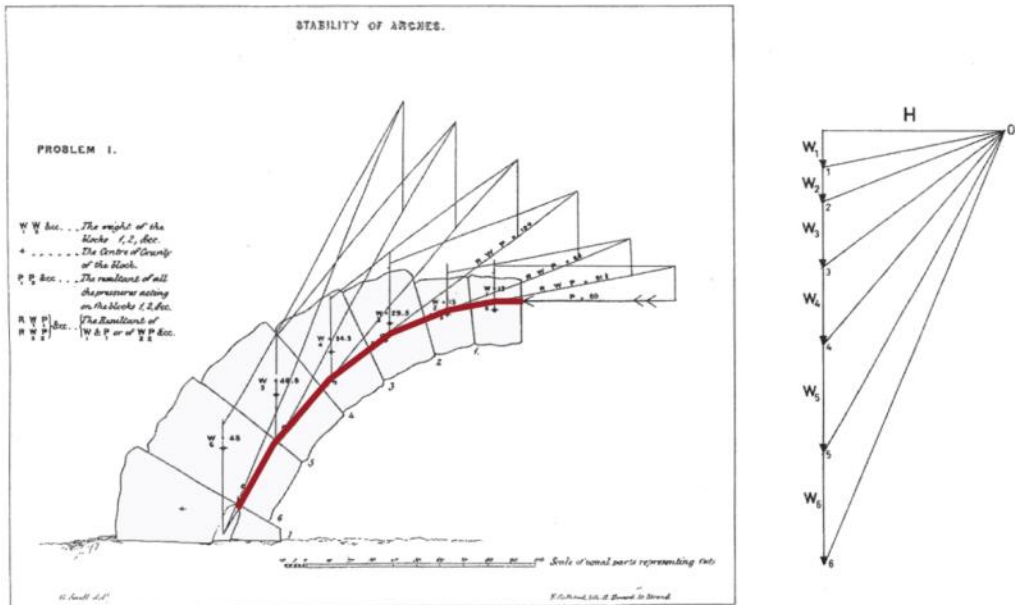


Figure 2.8 Graphical method by Snell [32]

However, as previously discussed, infinite thrust lines can lie within the arch boundaries. In [30], indeed, by adjusting the horizontal thrust, three more different graphical thrust line solutions (Figure 2.9) were proposed.

A more recent application of *graphical statics* [31] has been proposed in [33]; in particular, this application allows performing the graphical statics in a computational geometry framework.

Graphical methods have been nowadays almost replaced by numerical methods. However, methods such as graphic statics have been demonstrated to be still worthwhile and powerful, as shown in [35].

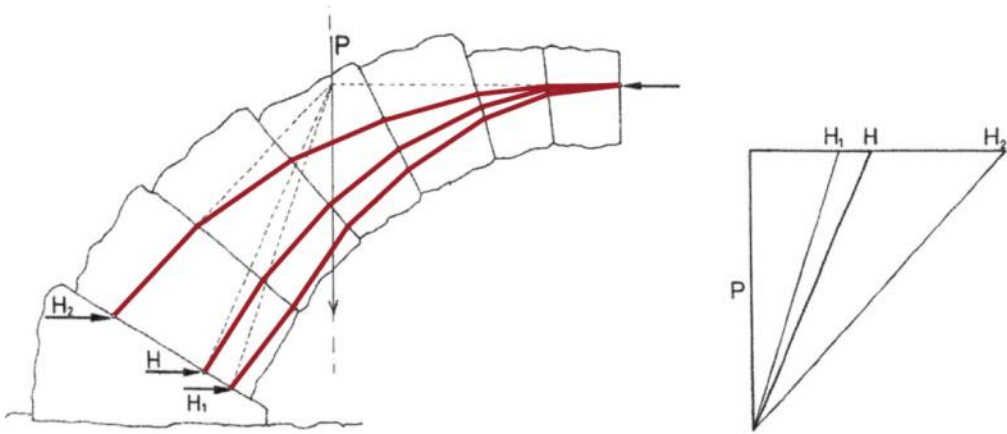


Figure 2.9 Graphical methods by Huerta [30]

Numerical methods can be applied to assess both the stability and the seismic behaviour. In the case of seismic assessment all the equilibrium numerical methods simulate the ground motion effects by means of a constant horizontal force. In [36] the problem of the masonry arch under seismic load has been studied by modelling the arch as a single degree of freedom (SDOF) system. The system consisted of a rigid body made up of three hinged bars and four hinges as shown in Figure 2.10. Once assumed the position of the four hinges, the equation of motion were derived by means of Hamilton's Principle and Lagrange equations for SDOF rigid body systems. The minimum acceleration required activating the collapse mechanism and the correspondent mechanism were achieved by iteration.

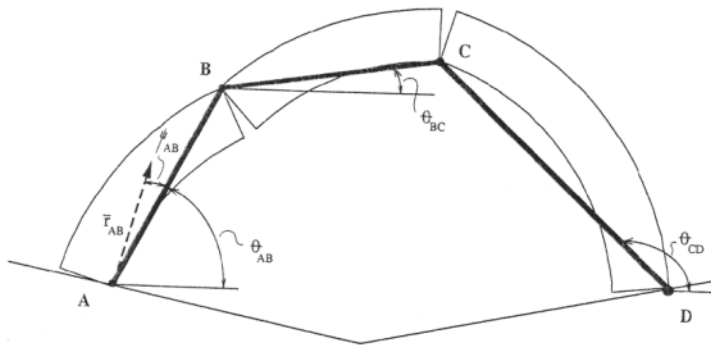


Figure 2.10 Masonry arch model under horizontal load [36]

The same structural scheme has been used in [37]. In this study, once assumed the position of the four hinges, the equilibrium equations were written in terms of virtual powers. The acceleration required to cause the collapse mechanism and the hinges positions (at the collapse) were achieved by iteration for several arch geometries. Other authors [38, 39] studied the same problem by means of the principle of virtual works.

2.3 Arch dynamic analysis methods

Analytical model builds upon the works first presented in [36] are presented in [16, 40]. However, the dynamic behaviour of arches is mainly studied by means of numerical methods. The authors of [36, 37], by extending their mechanism methods to the dynamic loading, found that:

- both the duration and magnitude of the ground acceleration highly influence the allowable ground acceleration;
- the allowable acceleration asymptotically decreases to the quasi-static allowable acceleration when the impulse duration increases;

- the acceleration impulse required to let the arch collapse, almost increase by the square root of the arch radius;

It is worth noting that none of the authors validated experimentally their modelling. However the main results of their findings are rational. An alternative to these methods is the Numerical finite elements method (FEM). FEM is, nowadays, one of the mainly used methods for the arch dynamics assessment. FEM analysis is, indeed, a powerful tool for the assessment of both dynamic linear and dynamic nonlinear response of the arches.

2.3.1 Finite Element Method (FEM) analysis

The FEM in the past was used to study masonry arch behaviour, mainly by means of static linear elastic analyses. The arch was usually modelled by means of one-dimensional elements (i.e. beam elements) [41, 42]. The FEM modelling techniques have been gradually refined and improved. Thus nowadays FEM is typically applied to study the dynamic behaviour of arches by means of both linear and nonlinear dynamic analyses.

In particular, FEM linear dynamic analyses are performed to study the fundamental dynamic properties (e.g. fundamental frequency, damping) and the steady-state dynamic response. By means of linear dynamic analyses is possible to assess the stress state, thus the location in which the cracking might occur. However, since masonry is a complex nonlinear material, in order to perform an accurate dynamic analysis, its nonlinear behaviour should be considered.

The nonlinear dynamic analysis is the more accurate approach to numerically assess the seismic response of a structure. In particular nonlinear dynamic analyses are performed in order to assess the evolution of stresses and strains in the time domain.

Both material nonlinearities and stress redistribution due to cracking are accounted. However, the results obtained are highly sensitive to the seismic input adopted for the analyses. Several examples of application of dynamic nonlinear analysis can be found in literature [43, 44].

2.4 Retrofit of historical buildings

Recent seismic events which affected the historical heritage buildings in Italy remarked the importance of a proper seismic retrofit intervention. Retrofit of historical masonry buildings is not an easy task. Indeed common retrofit techniques cannot be arbitrarily applied to historical buildings. On this matter the International council on monuments and sites (ICOMOS), which offers advice to UNESCO on World heritage sites, provided important recommendations [45]. Few of these recommendations are resumed in the following bulleted list (references to the ICOMOS recommendation articles are reported).

- The restoration of monuments must have recourse to all the techniques which can contribute to the safeguarding of the architectural heritage. (Article 2)
- The intention in conserving and restoring monuments is safeguard them no less as works of art, than as historical evidence. (Article 3)
- Where traditional techniques prove inadequate, the restoration of a monument can be achieved by the use of any modern techniques of construction, the efficacy of which has been shown by scientific data and proved by experience. (Article 10)

- The valid contributions of all periods to the building of a monument must be respected, since unity of style is not the aim of a restoration. When a building includes the superimposed work of different periods, the revealing of the underlying state can only be justified in exceptional circumstances. (Article 11)
- Replacements of missing parts must integrate harmoniously with the whole, but at the same time must be distinguishable from the original, so that the restoration does not falsify the artistic or historical evidence. (Article 12)

Therefore, depending on the cultural relevance of the studied building, the final choice could be either a stronger or a softer retrofit intervention.

For instance, for a highly vulnerable building, without any artistic value, the replacement of deficient structural elements could be a quick and efficient solution. Otherwise, if the same building would have a high artistic value, the same solution could even not to be feasible. In particular, according to [45] any retrofit intervention should be minimal and easily recognisable, in order to prevent any potential fabrication of the historical meaning of the building.

2.4.1 Retrofit of vaulted structures

As discussed in the previous Chapter 1, vaults are among the more vulnerable elements in historical masonry building. The damage of the vaults can be induced by several reasons, such as: variations in the acting loads, instability of the piers, and material degradation. The unexpected variation of either horizontal or vertical loads (or a combination of both) is among the more common cause of damage of vaults. The variation in the horizontal load frequently is due to a seismic event. Otherwise, the variation of vertical loads

often is due to a change of use of the structure. For instance, some historical buildings become museum, bearing loads which were not expected in the original design phase. The instability of the piers can be due to either subsidence of the foundation soil or changing in the pier constraint conditions. Furthermore, the mechanical behaviour of the vaults can be strongly influenced by the degradation of its constituent materials. For instance, an aggressive environment can lead to a reduction of the mechanical performances of materials such as: clay, tuff, or natural stones. Such materials are commonly used in vault construction. However, vaults geometry allows the distribution of the strains along the joints preventing significant cracking in the masonry units. Therefore, rather than the lack of strength, their collapse is generally due to the inability of the structure to follow the displacement of the piers [46].

A retrofit intervention should be able to provide its strengthening action only in case of changing of boundary conditions. Indeed, such intervention allows retrofitting the vault without changing its constitutive global response. Inappropriate retrofit interventions could even lead to an increase of the vulnerability of the retrofitted building.

A proper retrofit intervention starts with an accurate survey of the structure in order to assess the main vulnerabilities and potential instability sources. The survey has to take into account of: material and geometrical properties, crack patterns and degradation. According to [47, 48] the instability sources can be sort as follow:

- pier failure;
- vault spontaneous collapse;
- pier failure mixed with vault spontaneous collapse.

However, often the assessment of the instability sources is not straightforward. Indeed, it requires a strong knowledge and experience on masonry structural analysis together with a deep knowledge of the analysed structure.

Several simultaneous instability sources could coexist in the same structure making hard their recognition.

The analysis of damaged vaults shows that frequently the damages are restricted only in few locations which can be assumed as plastic hinges. The collapse mechanism will occur with the formation of the fourth plastic hinge (Figure 2.11). Traditional retrofit interventions on vaulted structures are based on the basic idea of improving the strength of the structure. Otherwise innovative retrofit techniques are based on the idea of improving both the capacity and the ductility of the structure, without increasing its mass and stiffness.

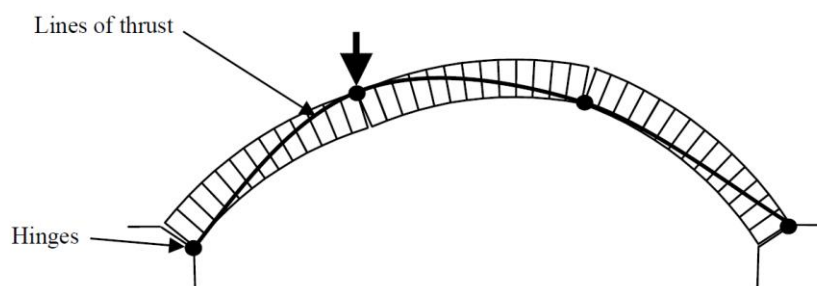


Figure 2.11 Typical four hinges mechanism due to vertical load [49]

2.4.2 Overview on the main retrofit techniques for the vaults

In the following a brief overview on the main retrofit techniques adopted for masonry vaults is provided. The aim of the following overview is to present a list of such systems. For each system a brief description and a review of both the main values and weaknesses is provided.

Buttresses

Several typologies of retrofit techniques can concern the piers of the vaulted structure. However buttresses are among the most commonly adopted retrofit techniques for historical buildings. The buttresses (Figure 2.12), which were widely adopted in the past, work by applying a counterforce opposing the thrust induced by the vault. Various materials can be employed for the construction of buttresses. They could be made of masonry as well as either non-reinforced or reinforced concrete. The main purposes of the buttresses are:

- preventing the distancing of the imposts;
- bearing the horizontal thrusts given by the vault together with the piers.

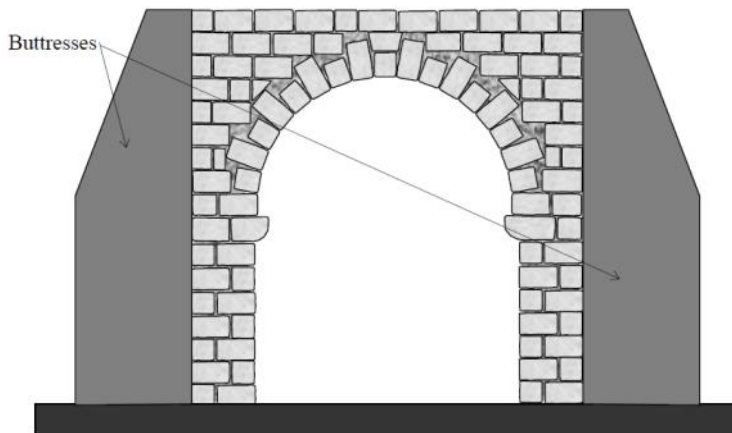


Figure 2.12 Example of ordinary buttresses [50]

The presence of a buttress results in a variation in the boundary conditions of the piers (i.e. the buttress improve the constraint condition). The variation in boundary conditions, in turn, results in a variation of magnitude of the reacting forces. As a consequence of the new force configuration, a new configuration of the thrust line will be achieved.

By analysing the load distributions inside the buttress it is clear that the loads are mostly located in the upper part of the buttress. In particular the analyses showed that the buttress works just like an arch. For this reason, in the ancient architecture (mostly in the gothic period), instead of the ordinary buttresses the flying buttresses were often adopted. In Figure 2.13 a brief illustrated overview of the main typologies of buttress through the history is reported. Nevertheless, despite its past wide spread, this strengthening technique, could not to be feasible for historical building. Indeed, the buttresses have a high shape factor which results in a high *visual impact*.

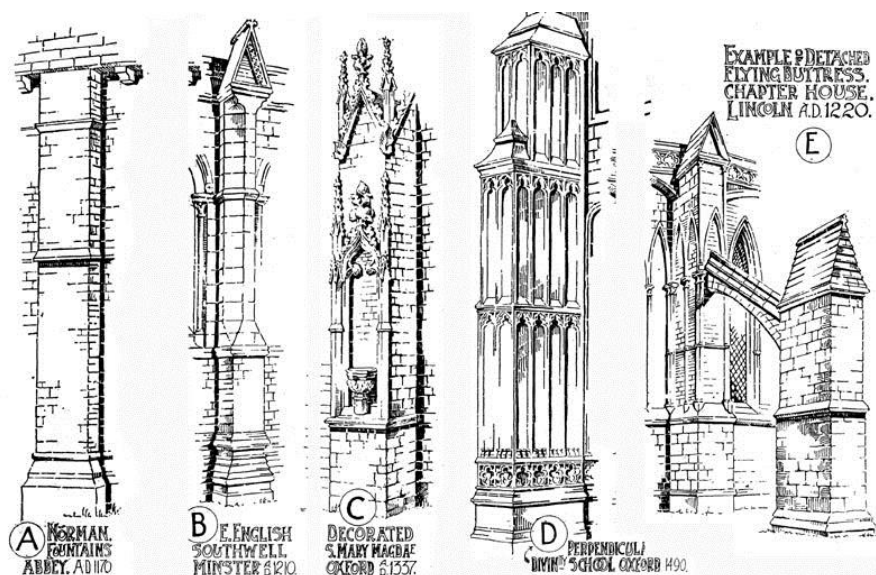


Figure 2.13 Typologies of buttress through the history: (a), (b), (c), (d) ordinary buttress; (e) flying buttress [12]

Ties

The ties (Figure 2.14) are the simplest way to counterbalance the thrust of the vault without imposing it to the piers. Their main purpose is, therefore, preventing the distancing between the imposts. Retrofit interventions by means

of ties were widely adopted in the past; however they are still widely adopted. Ties are mostly built up of either steel or wood (Figure 2.15); nevertheless usually the selection of the proper material is depending on the environment aggressiveness.

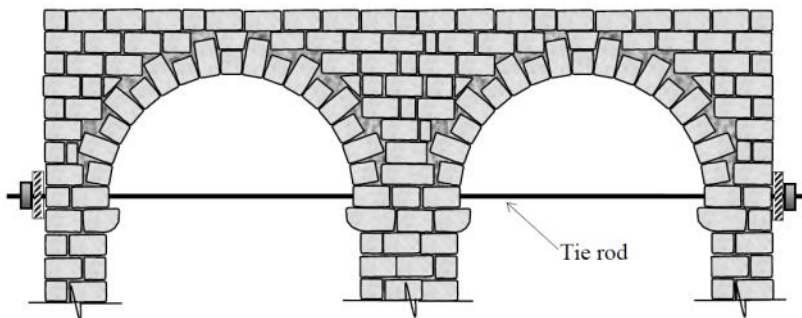


Figure 2.14 Tying scheme for a two span vaulted ceiling [50]

Tie retaining system can be passive (no pre-tensioned) or active (pre-tensioned). The former starts to work only once a relative displacement between the piers occur. Conversely, the latter does not need a relative displacement between the piers to start working. Tie dimensional design is crucial; it should be performed with regard to prevent any damage to the piers masonry due to the traction of the tie.

Compared to buttresses, ties certainly have a lower visual impact. However, depending on their positioning, they could potentially obstruct the view of artistic elements such as painting and frescoes located at the intrados of the vault. Depending on either architectural or structural reasons, ties can be applied both at intrados and extrados. From a structural point of view, ties located at the intrados have shown to be more effective in contrasting vault's thrust [51]. On the other hand ties located at the extrados, having a lower visual impact, could be a more suitable solution for historical buildings. In this case,

flexural forces acting on the portion of pier between the tie and the pier have to be taken into account.



(a)



(b)

Figure 2.15 Examples of curved element retrofit by means of ties of ties: (a) steel; (b) wood

In order to improve the flexural capacity of the piers post-tensioned ties can be applied in vertical. Usually this intervention is adopted when the vertical load is not sufficient to guarantee the stability of the piers. Frequently post-tensioned vertical ties are combined with horizontal ties. In this case, the anchorage of the vertical ties has to be at a higher quota compared to the horizontal ties location. This expedient allows the proper distribution of the stresses due to the tensioning of the vertical ties.

In addition to the retrofit intervention on the piers, several typologies of retrofit intervention can concern the vault itself. It is worth remarking that the conservation of any artistic/historical element, such as frescoes, paints or decorations, on the vault is the governing factor in the selection of the retrofit solution. However, when the vault itself is clearly damaged (e.g. cracking at either the intrados or the extrados), these interventions could be crucial for the

safety of the structure. In the following the main typologies of retrofit intervention on the vault are briefly presented.

Dead load reduction

An alternative solution to reduce the thrusts of the vault on the piers is to reduce the dead loads. Reducing the dead loads acting on the vault, results in improving the capacity of the vault to bear live loads. Basically the filling material (which is usually made up of earth) is replaced with a lighter material such as hollow bricks. Studies show that by means of this solution it is possible to reduce the dead loads of about 50% [52]. It is crucial during the intervention design phase, checking whether the new thrust line lies within the arch bounds or not. In order to achieve the new thrust line both the new dead and the new live loads have to be taken into account.

Reinforced concrete jacket

A solution frequently adopted, is the creation of a reinforced concrete jacket at the extrados of the vault (Figure 2.16). This solution sometimes is coupled with the previous discussed intervention of reduction of the dead load. In fact it is used in case in which the thrust line, due to the new loads, does not lie within the arch bounds. In order to let the reinforced concrete jacket works together with the old masonry vault, metal connectors between the two structures, have to be installed. The reinforced concrete jacketing improves both stiffness and strength of the vault. On the other hand, the high self-weight of the jacket may cause damages on both the structures and the foundations.

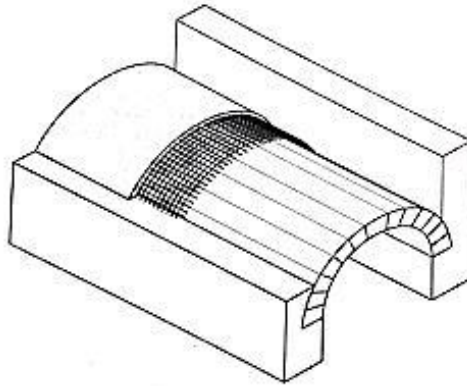


Figure 2.16 Reinforced concrete jacketing at the extrados of the vault

Furthermore the increase in mass due to the jacket could become disadvantageous, especially in case of earthquakes.

Grout injection

In recent years, the use of the grout injection as a retrofit technique is became common for curved masonry elements. The grout injections consist in filling: cracks, void, collar joints, or cavities within masonry (Figure 2.17). Usually the mixture injected is cement based. However the mixture composition depends on the characteristics of both the masonry and the crack to be filled.

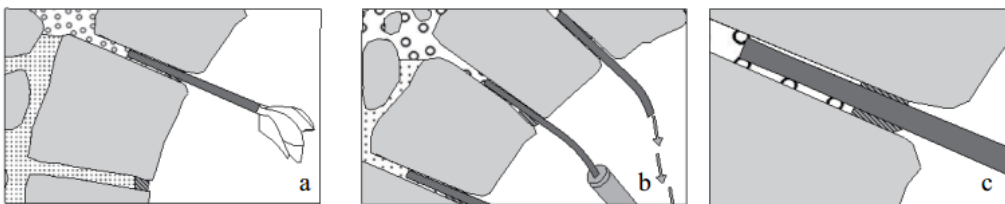


Figure 2.17 Examples of grout injections [53]

For instance cement-based grout is frequently used in the case of wide cracks [54]; while epoxy resin or cement fluid hydraulic binder are used in the case of

small cracks (less than 2 mm). The grout injection prevents the crack spread and improves the overall behaviour of the masonry [55]. Moreover, since the grout injection does not alter the aesthetic features of the retrofitted element, it is particularly suitable for historic buildings.

Mortar joint repointing

Mortar joint repointing is one of the basic procedures in the refurbishment of masonry elements. It consists in removing damaged (or deteriorated) mortar from masonry joints and replacing it with new mortar. In Figure 2.18 is reported the typical repointing process. Repointing allows improving the strength and the stiffness of masonry [56] and it reduces the water effect. Usually the mortar joint repointing is coupled with other retrofit techniques such as grout injection or near surfaces mounted reinforcements.

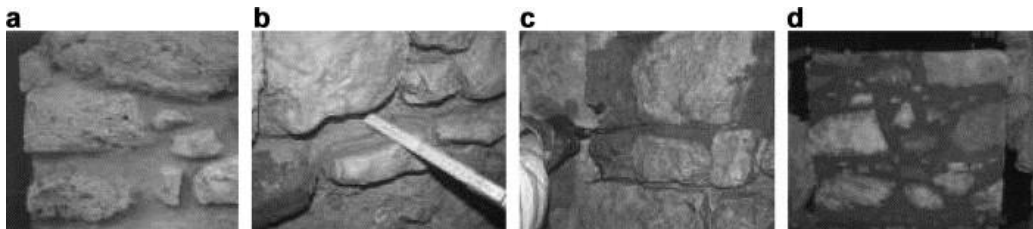


Figure 2.18 Mortar joint repointing process: (a) Joint after cleaning; (b) detail of the joint depth; (c) joint's repointing; (d) after intervention [56].

An efficient repointing retrofit starts with the assessment of the existing materials. Such knowledge is crucial in the selection of the mortar to be used for the repointing intervention. Indeed, the selection of the mortar is critical to the long-term durability and performance of the intervention. In particular, the new mortar has to be durable and compatible with existing masonry. If the mortar is too strong or too stiff than the adjacent materials, it can even damage the masonry units reducing the durability of the intervention.

Moreover, both the old mortar removing and cleaning operations are crucial as well. Improper joint preparation frequently results in falling out of the repointed joint within a few years. Otherwise a proper repointing intervention can last between 25 and 30 years.

2.4.2.1 Innovative retrofit techniques

The raising awareness for the preservation of historical buildings, together with the development in the innovative materials technologies, has supported the growth of innovative retrofit techniques. Traditional retrofit techniques are based on the idea of improving the strength of the structure. Otherwise the approach of innovative techniques is based on the idea of improving both capacity and ductility. The choice among solutions traditional or innovative is controversial. However, depending on the specific case, innovative techniques can either coexist with the traditional techniques, or be used as their alternative. In the following a brief overview of the main innovative retrofit techniques for vaults and curved elements is presented.

Reinforced arch method (RAM)

The Reinforced Arch Method (RAM) is often presented as an innovative alternative to the reinforced concrete jacket. It consist in a distributed reinforcement, applied to the extrados (or the intrados) of the vault. The basic concept of this retrofit intervention (introduced for the first time in [57, 58] is to modify the distribution of loads acting on the arch in order to let the thrust line lie within the arch bounds. Therefore this intervention is suitable to be coupled with the reduction of the dead loads. Both steel and FRP reinforcing cables can be used as a tensile resistant reinforcement. The installation of the RAM is

made up by means of post-tensioned cable yarns fixed to the extrados of the vault as shown in the Figure 2.19.

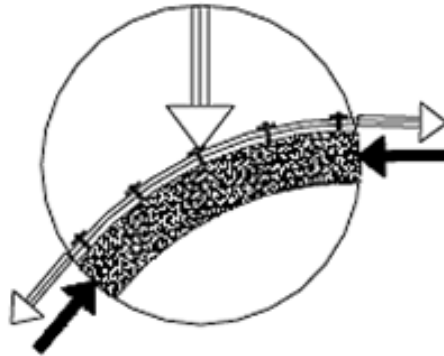


Figure 2.19 Detail of the anchorage of the cable to the extrados [57]

The cables can be fixed at both the intrados and the extrados. However, due to the necessity of cable deviator, the installation at the intrados could be difficult. The post-tensioned cables application results in a radial distribution of forces on the vault. In Figure 2.20 is reported the force interaction scheme in both the cases of reinforcement at the extrados and reinforcement at the intrados.

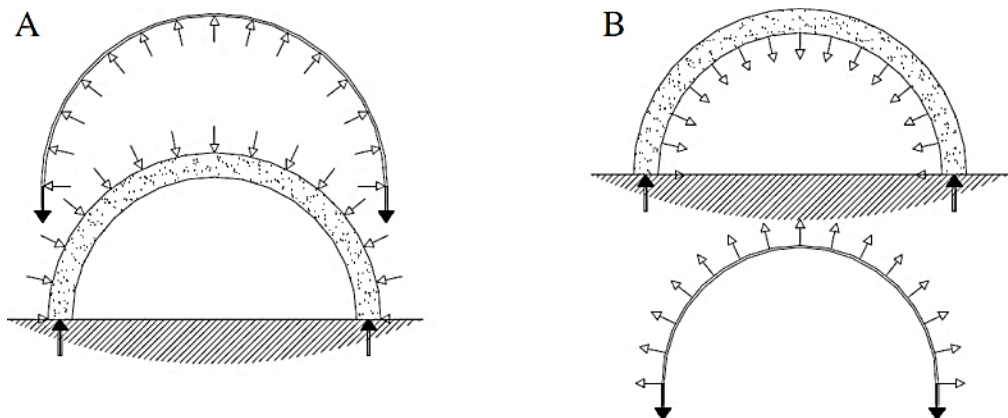


Figure 2.20 Force interaction between the cable (in tension) and the vault (in compression): (a) reinforcement at the extrados; (b) reinforcement at the intrados [58]

The RAM improves the seismic behaviour of the vault. In fact, it improves both capacity and ductility of the vault, without increasing its mass and stiffness.

Near Surface Mounted (NSM) reinforcement

The near surface mounted (NSM) reinforcement consists in installing FRP or stainless steel reinforcing bars in a groove cut into the surface of the masonry [59, 60]. Depending on the desired strengthening (i.e. either flexural or shear) the location of the bar application can change. For instance, in the case of flexural strengthening, bars are vertically applied. Otherwise, in the case of shear strengthening, bars are inserted horizontally in the masonry bed joints (see Figure 2.21).

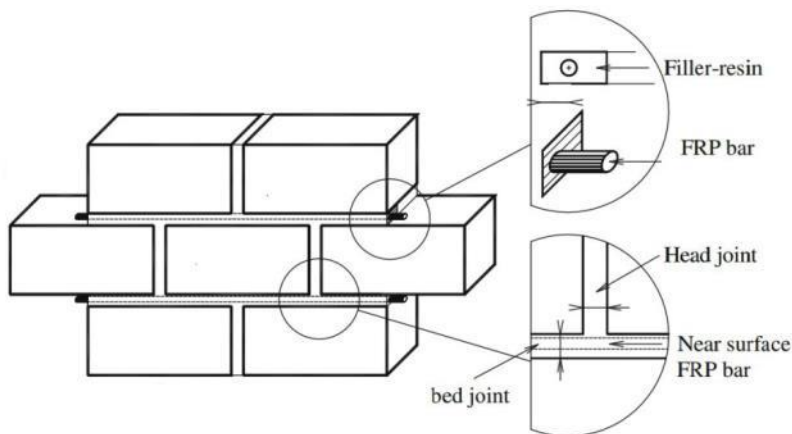


Figure 2.21 Bed joint NSM reinforcement for a masonry representative element [61]

NSM reinforcement in masonry curved elements improves the load carrying capacity, reduces the hinge formations and reduced the crack development [59]. Low aesthetic impact and easy installation are among the values of this retrofit technique. Furthermore the NSM reinforcement provides no mass improvement which is crucial in seismic retrofit. Experimental and theoretical studies show the effectiveness of this retrofit technique.

FRP laminates/fabric

Another innovative solution for the retrofit of vaults is the use of FRP laminates. The FRP laminates can be installed at the extrados, at the intrados or at both the intrados and the extrados of the vault. Figure 2.22 shows the three possible retrofit layouts for barrel vaults.

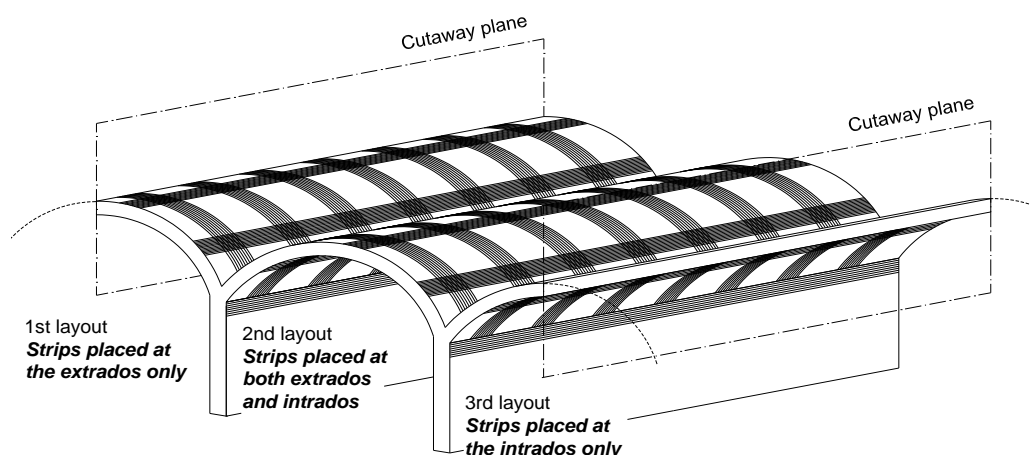


Figure 2.22 Possible retrofit layouts for barrel vaults [62]

However, the installation at the intrados is not always possible. For instance, in the case of historical buildings, the presence of valuable stuccoes and frescoes, preclude the chance of removing the plaster. Thus the reinforcement can be only installed at the extrados. On the other hand, whether valuable tiles or floorings, which cannot be removed, are present, the chance of retrofit at the extrados is precluded. However, it is worth remarking that, due to tensile stresses normal to the reinforcement (Figure 2.23), the application of FRP laminates at the intrados is the most critical with respect to the debonding failure. The basic concept of the retrofit with FRP is to prevent the hinge mechanism and, therefore, the brittle collapse. This result is achieved moving the failure mechanism from brittle to ductile, by improving the energy

dissipation. Several experimental tests [63, 64] showed the effectiveness of retrofit with FRP in preventing the hinge formations. Then, according to [62] in the case of retrofit with FRP the main potential failure modes are: debonding, FRP rupture, crushing and sliding.

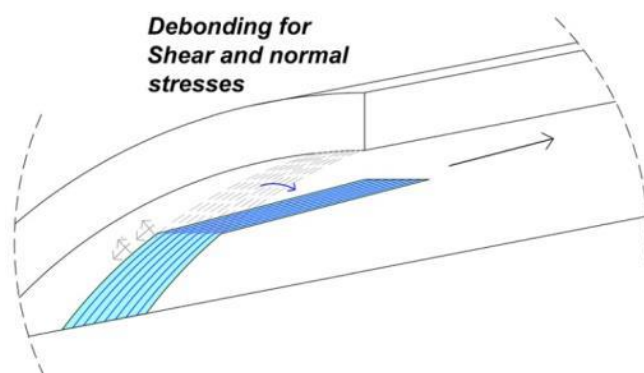


Figure 2.23 Debonding in curved structures [62]

The debonding failure is the main critical issue of the retrofit with FRP. It is mostly due to the curvature of vaults coupled with both the peeling stresses and normal axial forces at the FRP fibre plane. However, the application of longitudinal quadriaxial strips provides anchoring to former transverse strips preventing the debonding failure.

If a proper FRP anchorage is provided, the FRP rupture is possible. Nevertheless, whether the original failure is governed by shear failure or crushing of the masonry, the effectiveness of the FRP retrofit is not granted.

Crushing failure as well as sliding failure is related to the load pattern. The former is achieved when the thrust line is very close to the bounds of the arch. In particular it is due to either load pattern variations or increases in flexural forces. The latter is usually achieved for highly non-symmetric loads. In order to reduce sliding issues, the masonry substrate preparation (usually by means of

thin layer of fibre reinforced mortar) is crucial. The same issues discussed in the case of FRP laminates can be repeated in the case of FRP fabric. In the case of vault retrofit, the fabric is commonly preferred to the laminates due to its ability to fit curved geometries.

Inorganic Matrix composite Grids (IMG)

As discussed in the previous section the use of FRP laminates (fabric) in masonry structural retrofit has shown to be effective. However, this technique has shown a number of problems. In particular, the main problems are: insufficient vapour permeability, low performances at high temperatures (flammability), lack of bond between resins and masonry substrates, no reversibility [5]. By means of inorganic matrix composite grid (IMG) such issues can be overcome. IMG retrofit is an innovative retrofit technique based on inorganic matrixes. In particular the inorganic matrix (e.g. cement based matrix) replaces the *traditional* epoxy resin of the classic FRP system (see Figure 2.24).

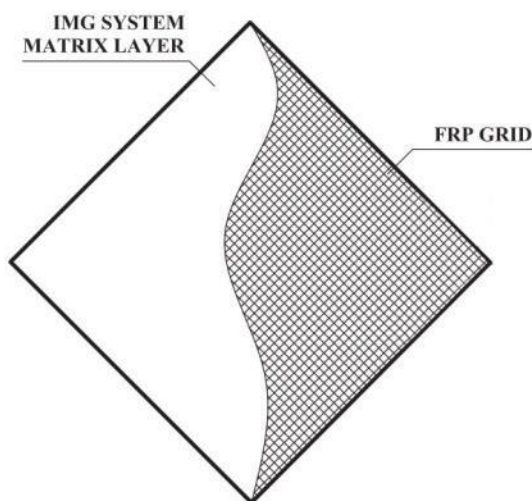


Figure 2.24 IMG retrofit system scheme

The main advantage of inorganic cement based matrixes is the high physical and chemical compatibility with the masonry substrate. Thus usually premature debonding failure does not occur. Furthermore, due to its continuous nature, the IMG is particularly suitable for curved masonry elements such as arches and vaults. Several experimental tests show [4, 5] that the IMG strengthening systems increase the load-bearing capacity of masonry elements.

An issue related to the IMG system can be found in the installation phase. In fact the IMG system should be installed at temperatures ranging between 5°C and 35°C. The installation at higher temperatures results in a sensitive decrease in the mortar workability. Otherwise, the installation at lower temperatures results in setting slow down.

It is worth noting that, being innovative this technique, there is still not a widely adopted name. Therefore in the literature, it is usually identified with several different acronyms generating possible misunderstandings. For instance some of the more frequent acronyms are: fibre reinforced cementitious mortar (FRCM), fibre reinforced cementitious matrix (FRCM) and cementitious matrix grid (CMG).

2.5 Experimental studies

The seismic behaviour of masonry vaults is strongly affected by the global behaviour of the structure in which they are inserted. On the other hand the role of structural components testing is fundamental [65]. Vault's dynamic behaviour is generally treated by means of either simplified mechanism methods or complex computational analysis [40, 66, 67]. Even so, detailed knowledge on the dynamic behaviour of the vault elements is still lacking from

an experimental point of view. In particular, only a few dynamic experimental tests on unreinforced masonry vaults are available in scientific literature. On the other hand, a lot of study can be found about reinforced vaults under static or quasi static loads. In the following, a brief overview on some experimental tests concerning retrofitted masonry vaults is presented.

2.5.1 Tests on reinforced arches and vaults

An interesting study provided in [63] highlights the results of an experimental investigation on brick masonry vaults strengthened with FRP strips. The behaviour of masonry vaults reinforced with FRP laminates has been studied by means six specimens. The specimens were subjected to monotonic vertical load applied at $\frac{1}{4}$ of their span. The geometry of the specimens and load conditions are shown in Figure 2.25.

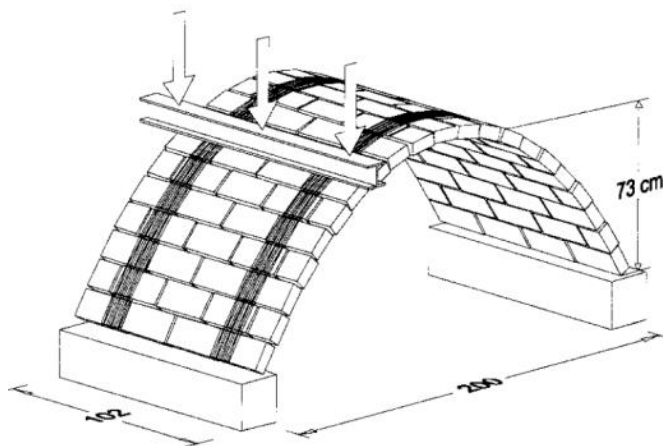


Figure 2.25 Geometry of the specimens and load conditions [63]

The FRP strips applied at the intrados (or extrados) results in an alteration of the collapse mechanism. The results of these tests showed that the width and the stiffness of the reinforcement strips have a strong influence in the behaviour of

the vault. Vaults strengthened at the extrados showed possible brittle failure; while vaults strengthened at the intrados showed a ductile failure mechanism. This is due to the detachment of the fibre perpendicularly to the masonry interface. The failure involves a limited area, thus the strips can still prevent the collapse.

In [68] a study on the dynamic behaviour of masonry barrel vaults is presented. Vault dynamic behaviour has been investigated in the cases of unreinforced vault, damaged unreinforced vault and retrofitted vault. The vault has been retrofitted by means of GFRP strips (at the extrados). In Figure 2.26 is shown the reinforcement configuration.



Figure 2.26 Reinforcement configuration [68]

The results of experimental tests showed a good dynamic behaviour in both the cases of undamaged and damaged vault. After the retrofit the vault showed a dynamic behaviour similar to the undamaged vault.

A contribution to the investigation of the effectiveness of the IMG as seismic retrofit of vaults is found in [46]. In particular in this study the retrofit is based on steel cords embedded in an inorganic cement based matrix (i.e. steel

reinforced grout). The research consists in the retrofit of the vaults for the case study of Jacobilli building which is a clustered complex in the historical centre of Foligno (Italy). The building was seriously damaged by the Umbria-Marche earthquake (1997). Therefore, in order to improve the strength of the cloister vaults included in the building against earthquake, two systems have been adopted. A couple of prestressed steel reinforced grout (SRG) strips and a reticular system made of transversal and longitudinal prestressed SRG laminates. The reinforcements have been applied at the extrados of the vault (see Figure 2.27).



Figure 2.27 Extrados of the vault after the intervention [46]

The study remarks that the retrofit can modify the failure mode of the masonry vault preventing the formation of the fourth hinge. Furthermore the retrofit significantly increases the load carrying capacity of the vault.

Another application of IMG on curved masonry elements is provided in [69]. In particular laboratory tests were carried out on seven semicircular brick arches which underwent repair and retrofit.

The experimental tests on models showed that in all the cases the use of Fibre Reinforced Cementitious Matrix (FRCM) reinforcement significantly enhances the load-bearing capacity of the brick arches (vaults). In particular, the cementitious matrix has ensured a good capacity for distribution of stresses on the masonry support.

A comparison between the experimental performances of FRP strips and IMG is provided in [70]. The tests were carried out on two arch specimens. The first specimen has been retrofitted with carbon FRP (CFRP). The second specimen has been retrofitted with glass fibre reinforced cement matrix (GFRCM). The reinforcements have been applied on the whole surface at the intrados of the arches. The experimental results showed that, under seismic load, the GFRCM performed better. Furthermore the specimen retrofitted with GFRCM showed a failure mechanism similar to an unreinforced arch. Conversely the failure mechanism for the specimen retrofitted with CFRP strips was different. In particular, due to delamination, a highly brittle collapse occurred.

A further contribution on the study of reinforced vaults is found in [71] which studied the IMC for masonry vaults by means of experimental tests. In particular the influence of the retrofit has been studied by comparing the results achieved for different kinds of retrofit. Both the static and the dynamic behaviour of the retrofitted vaults were studied. The specimens were retrofitted with five different systems. In particular: SRG, basalt textile reinforced mortar (BTRM), steel reinforced polymers (SRP), CFRP and reinforced transverse vertical diaphragms (RTVD). The specimens were subjected to both monotonic and cyclic vertical load applied at $\frac{1}{4}$ of their span (Figure 2.28).



Figure 2.28 Experimental test setup [71]

The results showed that all the tested retrofits result in a substantial increase of the load capacity and ductility. The dynamic identification allowed relating the decay of the fundamental frequencies to the increase of the damage.

The dynamic behaviour of both unreinforced and reinforced masonry vaults have been studied in [72]. Shaking table tests have been performed on a masonry vault. In particular the specimen consisted of a 1/3 scale masonry vault with parapets (Figure 2.29) loaded with a uniformly distributed load.

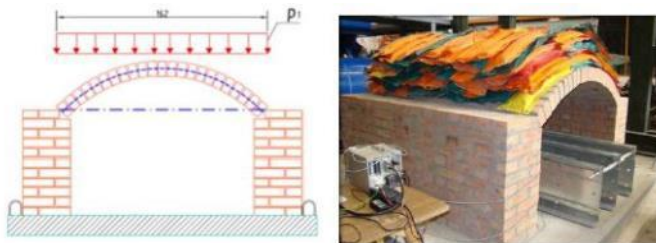


Figure 2.29 Experimental test setup [72]

The specimen was built on a reinforced concrete slab connected to the shaking table. The specimen was monitored by linear variable differential transformer (LVDT) and accelerometers. Two accelerograms (one natural and one artificial) have been imposed to the structure without producing any significant damage to the specimen. In order to achieve the failure, a sine sweep action (having acceleration equal to 0.5 g) have been imposed to the structure. The collapse started due to relative displacements in the mortar beds near the abutments and was due to the formation of five hinges.

The investigation of uncertain features of the masonry vault seismic response has been proposed in [73]. On this purpose experimental tests on mono-directional shaking table have been performed.

The specimens were arches made of tuff bricks resting on two piers which continue over the impost. Furthermore some steel ties were placed between the wing walls. A sketch of the specimen is provided in Figure 2.30.

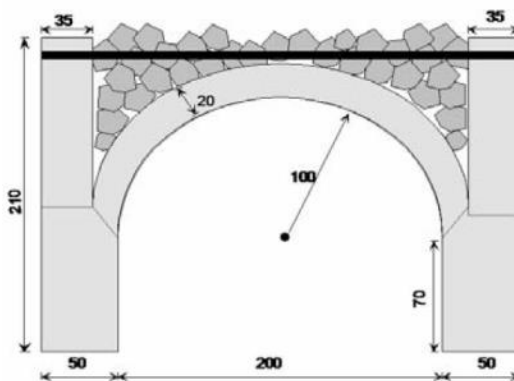


Figure 2.30 Experimental test setup [73]

The test consisted in two phases. The first phase was performed by means of the same dynamic signal (which reproduces a natural earthquake) scaled at progressively increasing intensities. In the second phase an overload was

imposed on the top of the arches. The specimens were monitored by accelerometers (applied on the arch) and transducers (applied at the external sides of the piers). The collapse was not reached in the first phase. Then the collapse was reached in the second phase. By the comparison of the outcomes of the two phases it was evident that the static degradation was faster than the dynamic one. However this result is probably due to the previous damages occurred.

Chapter 3

Experimental tests: unreinforced vault

The experimental programme presented in this chapter aims to investigate the dynamic behaviour of a masonry vault subjected to a dynamic base excitation. In particular dynamic shaking table tests on a full scale masonry barrel vault have been performed at the Laboratory of the Department of Structures for Engineering and Architecture (University of Naples “Federico II”).

A comprehensive overview of the results of the shaking table tests is presented and discussed. The presented experimental activity is part of a wider research project which involves the University of Naples “Federico II”, University of Padova, STRESS S.c.ar.l, Veneto Nanotech s.p.a., Regional Center of Assistance for Economic Cooperation Artisan, CETMA Consortium, Consortium TRE and SIPRE s.r.l. In the presented experimental tests the vault is tested without any vertical load acting at the extrados. This load condition is suitable, for instance, to simulate typical historical vaulted roof. Furthermore, the vault’s imposts are constrained on the shaking table. Therefore the outcome represents the behaviour of the vault itself.

The aim of these tests is to improve the knowledge on the dynamic behaviour of the masonry vaults once the settlement and capacity of the supports of the vaults, (e.g. imposts, masonry piers, load bearing walls) are guaranteed.

3.1 Specimen

A full scale clay brick masonry vault has been designed for testing purpose. The geometry of the specimen (Figure 3.1) is the same of the vault which has been tested under static conditions in [71]. The geometry of the vault has been carefully chosen to simulate a typical masonry vault commonly included in historical heritage buildings.

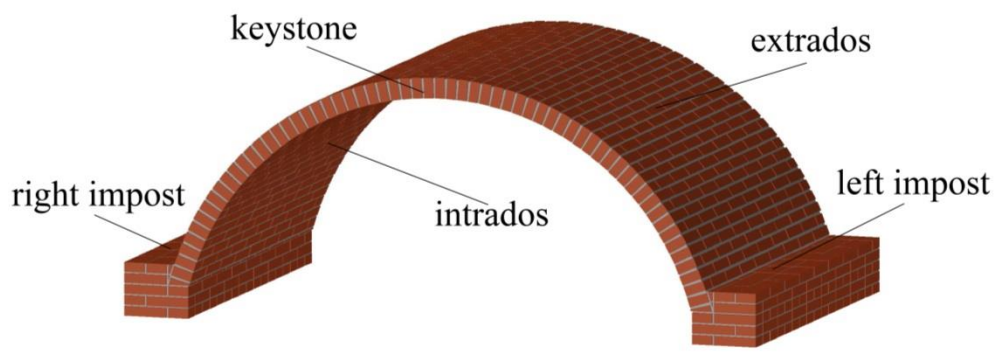


Figure 3.1 Geometry of the specimen: 3D view

The vault has a segmental arch profile (less than a semicircle) having a clear span of 298 cm and a rise of 114 cm. The vault is 220 cm deep and it is made of solid facing clay brick ($25 \times 5.5 \times 12 \text{ cm}^3$) and pozzolanic masonry mortar (i.e. MAPEI MAPE *Antique allettamento*). The mortar mixture was prepared in order to present typical properties of mortars used in historical buildings.

The vault is fixed on two imposts made of the same masonry material. Further geometrical details are provided in (Figure 3.2).

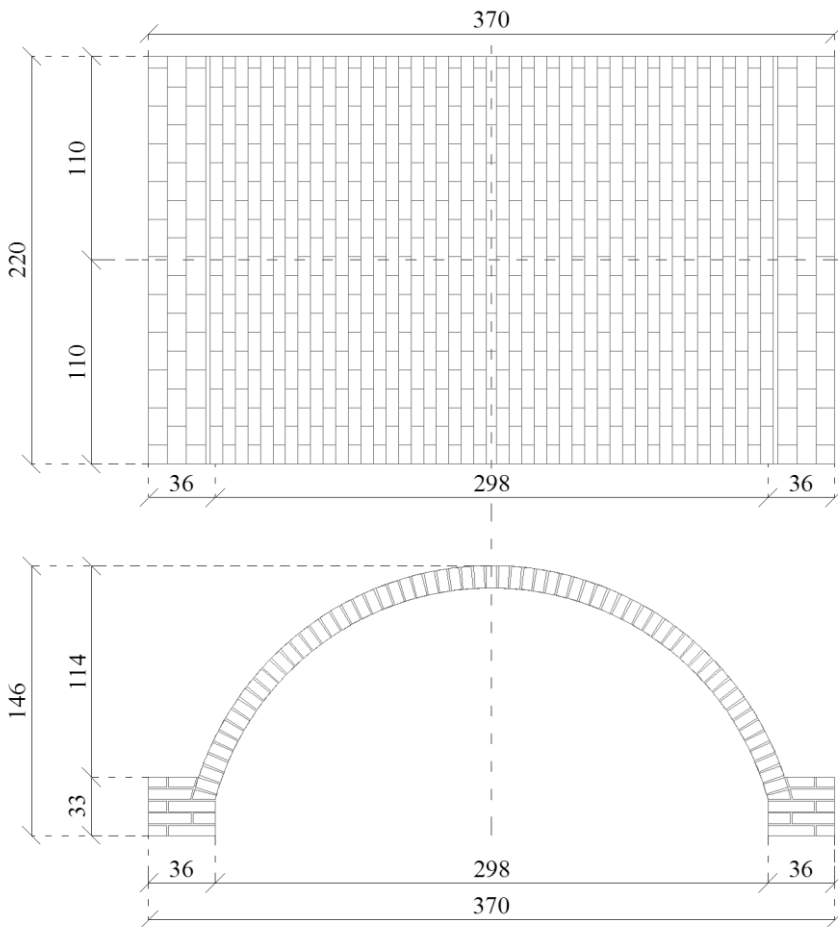


Figure 3.2 Geometry of the specimen: plan and section views (dimension in cm)

The specimen was built up on a steel beam system which is part of the testing structure (further information about the technical characteristics of the testing structure will be discussed in the following section 3.3). Since the vault is not self-supporting, until the keystone bricks were positioned, a polystyrene centring has been used as a temporary support (Figure 3.3a).

The polystyrene centring was placed on wooden supports in order to keep it at the proper quota and facilitate its removal after the vault was completed. Some images concerning the construction phases are shown in Figure 3.3.

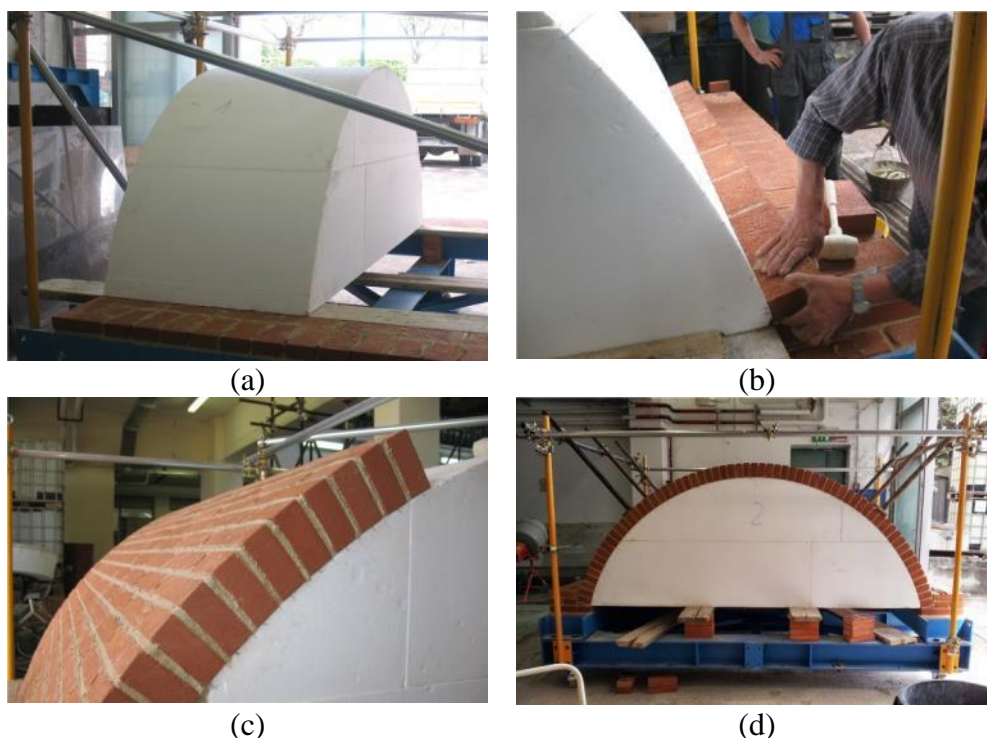


Figure 3.3 Specimen during construction phases: (a) polystyrene centring; (b) construction of the impost; (c) curved element construction; (d) specimen completed

3.1.1 Material characterization

Preliminary mechanical characterization tests have been performed for both mortar and bricks. Table 3.1 lists the main results of the material characterizations. Both brick's compressive and tensile strength, as well as elastic modulus, were characterized in [74].

In particular, according to UNI 8942-3 (1986) [75], three point bending tests have been performed. In these tests the brick is placed on two supports. Then given the distance, l , between the two supports, (typically $l = 200$ mm), the actuator applies a force in the middle of the two supports ($l/2$).

Table 3.1: Material mechanical properties.

Property	Brick [MPa]	Mortar [MPa]
Compressive strength	19.8	10.1
Flexural strength	3.7	-
Splitting tensile strength	2.5	-
Tensile strength	-	2.4
Elastic Modulus	5756	1452

Therefore the flexural strength, $\sigma_{f,b}$, is achieved by applying the well-known Navier's formulation (simple bending case). In particular in this case the following Equation (3.1) has been used:

$$\sigma_{f,b} = \frac{3P_u l}{2bh^2} \quad (3.1)$$

Where b and h are the dimensions of the brick's cross section, and P_u is the ultimate achieved load.

Compression tests on the bricks have been performed as well. In particular, according to EN 772-1 (2002) [76], the compression force on the two faces of the specimen have to be applied by means of suitable actuators.

Assuming a uniform stress distribution along the horizontal sections of the brick, the compressive strength, $\sigma_{c,b}$, can be achieved by means of the following Equation (3.2):

$$\sigma_{c,b} = \frac{P_u}{bd} \quad (3.2)$$

Where b and d , in this case, are the dimensions of the section in which the load P_u is applied. Indirect tensile strength has been achieved according to UNI 8942-3 (1986) [75]. In particular the indirect tensile strength, $\sigma_{s,b}$, has been evaluated by means of the following Equation (3.3):

$$\sigma_{s,b} = \frac{2P_u}{\pi bd} \quad (3.3)$$

Characterization tests on the mortar (Figure 3.4) have been performed according to UNI EN 998-2 (2010) [77] and UNI EN 1015-11 (2007) [78] on twelve $40 \times 40 \times 160 \text{ mm}^3$ 28 days wet cured specimens.



Figure 3.4 Material characterization: mortar specimen preparation

In order to achieve the elastic modulus, several tests were performed according to UNI 6556 (1976) [79]. The elastic modulus reported in Table 3.1 has been achieved as average of the elastic modulus achieved in these tests.

3.2 Experimental facilities

Shaking table tests have been performed in order to investigate the seismic behaviour of the brick masonry vault. The tests have been carried out at the laboratory of the Department of Structures for Engineering and Architecture of the University of Naples Federico II.

The tests have been performed by means of an earthquake simulator system (ESS). In particular the ESS consists of two square shaking tables ($3\times 3\text{ m}^2$). Each table is characterized by two degrees of freedom in the two horizontal directions. In Figure 3.5 a scheme of the EES is provided.

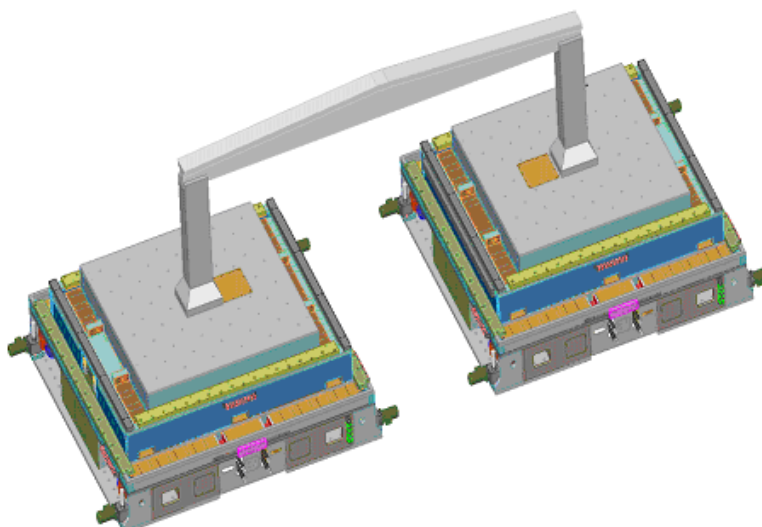


Figure 3.5 Earthquake simulator system (ESS) scheme

Each shaking table has a maximum payload of 200 kN having a frequency range of 0 – 50 Hz, acceleration peak equal to 9.81 m/s^2 , velocity peak equal to 1 m/s (both at maximum payload) and total displacement equal to 500 mm ($\pm 250 \text{ mm}$). In the presented experimental tests only one table is used.

3.3 Testing structure

Since the width of the specimen to be tested (3.7 m) was larger than the shaking table platform (3.0 m) an additional structure was required. Main purpose of such structure was to rigidly transfer the acceleration from the shaking table to the structure to be tested. Therefore a steel testing frame has been expressly designed. Furthermore in order to allow the specimen to be built off of the shaking table platform, a lifting structure for the test setup has been designed, too. Therefore the testing structure consists in two sub-structures namely *testing frame* and *lifting structure* respectively. The total weight of the testing structure, including the lifting structure (Figure 3.6), is 17.22 kN.



Figure 3.6 Testing structure overview

3.3.1 Testing frame design

The design of the testing frame involved two main stages. The first stage consisted in the estimation of the loads acting on the testing frame during the tests. The second stage consisted in the design and verification of the testing frame and its structural elements. At the first stage, the loads acting on the testing frame have been evaluated by means of preliminary numerical finite elements (FE) analyses. In particular, static nonlinear analyses have been performed on a simplified FE model.

The preliminary FE analyses were performed by means of the software DIANA developed by TNO DIANA. The FEM model is constituted of more than 800 CQ16M eight-node quadrilateral isoparametric plane stress elements based on quadratic interpolation and Gauss integration. Further details about the CQ16M element are provided in the following section 5.1.

A macro element approach was adopted. The masonry was modelled as a homogeneous material according to the total strain model coupled with the rotating crack stress-strain relationship approach. In particular, in the total strain approach, the constitutive model describes the stress as a function of the strain. In the rotating crack approach, stress-strain relationships are evaluated in the principal directions of the strain vector, as reported in [80]. Furthermore, the combined Rankine/Von Mises yield criterion was adopted. In Figure 3.7 the preliminary FE model of the vault is shown.

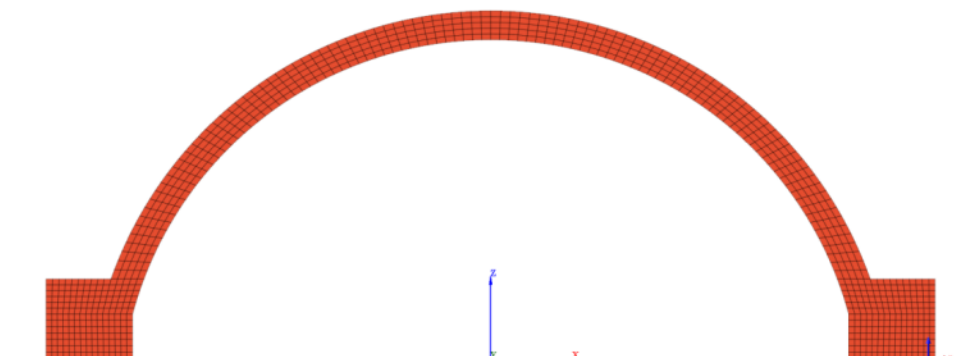


Figure 3.7 FE model of the specimen

All the analyses were performed under load control, measuring the evolution of both the reacting forces and displacements. The load, which is horizontal and proportional to the mass of the model, has been applied at increasing steps. According to the experimental boundary conditions, the two imposts of the vault have been fixed. The outcomes of the analyses allowed studying the trend of the base reacting forces when varying the horizontal load multiplier (Figure 3.8). This trend represents the forces which the testing frame has to bear without significant deformations. Furthermore the numerical analyses allowed estimating a *broad* value of the horizontal load multiplier at the formation of the first hinge. Since at this stage characterization tests on the masonry materials were not yet performed, average values for the mechanical properties were considered. However, in order to take into account of the variability of the tensile strength which is the governing parameter, parametric analyses were performed. The outcomes, in terms of horizontal load multiplier, are shown in Figure 3.9.

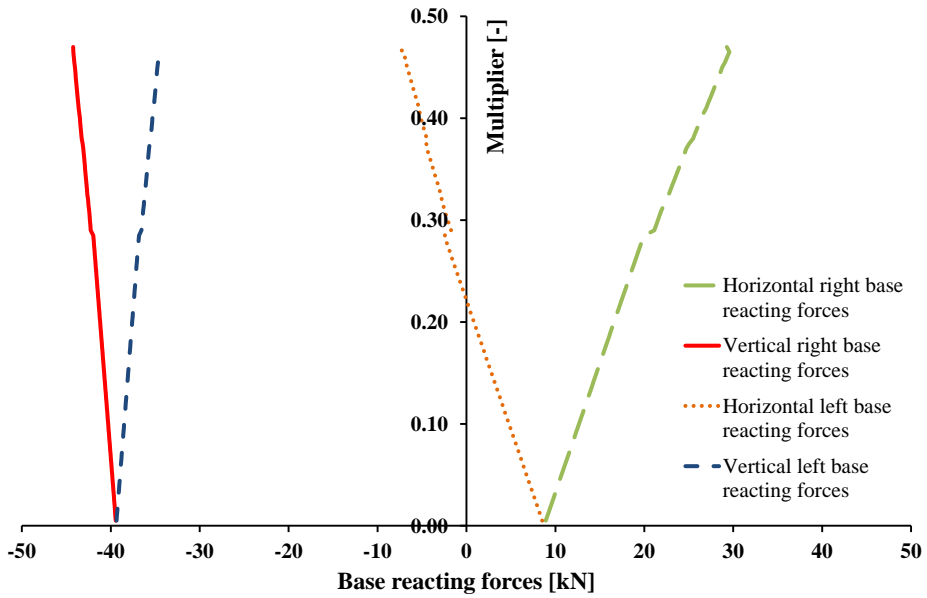


Figure 3.8 Static nonlinear analyses results: horizontal load multiplier-base reacting forces (horizontal and vertical)

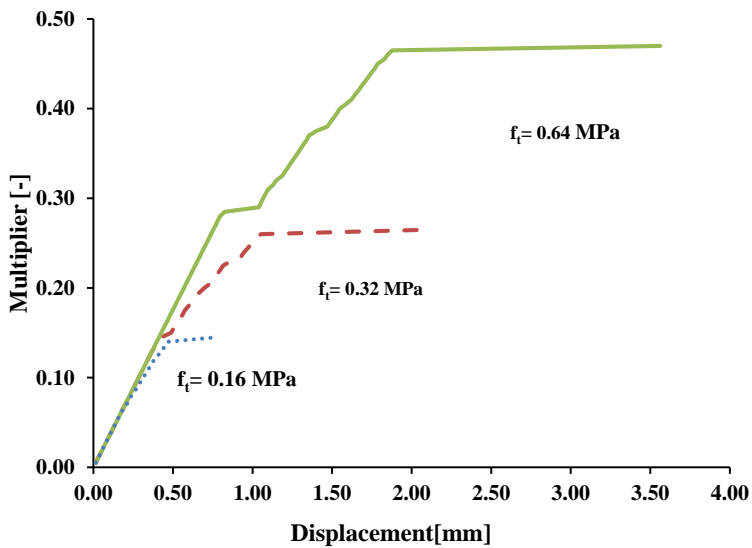


Figure 3.9 Static nonlinear analyses results: horizontal load multiplier-displacement curves

Due to the high variability of the mechanical parameters, all the results achieved at this stage have to be considered as approximate values. Therefore at the design and verification stage partial safety factors were adopted. According to the outcomes of the FE analyses performed at the previous stage, the testing frame has been designed. In particular, the testing frame is a steel plane frame constituted of three H shaped beams (HE240B profile in Figure 3.10) bolted on the shaking table platform. Two U shaped beams (welded U profiles in Figure 3.10) are bolted on the main H shaped beams, forming a two span beam scheme. The structure has a symmetric K-bracing system in order to prevent the buckling and to increase the in-plane stiffness of the plane frame. The bracing system is constituted of six steel U shaped beams (UPN100 profile in Figure 3.10). A sketch of the complete steel plane frame is provided in Figure 3.10.

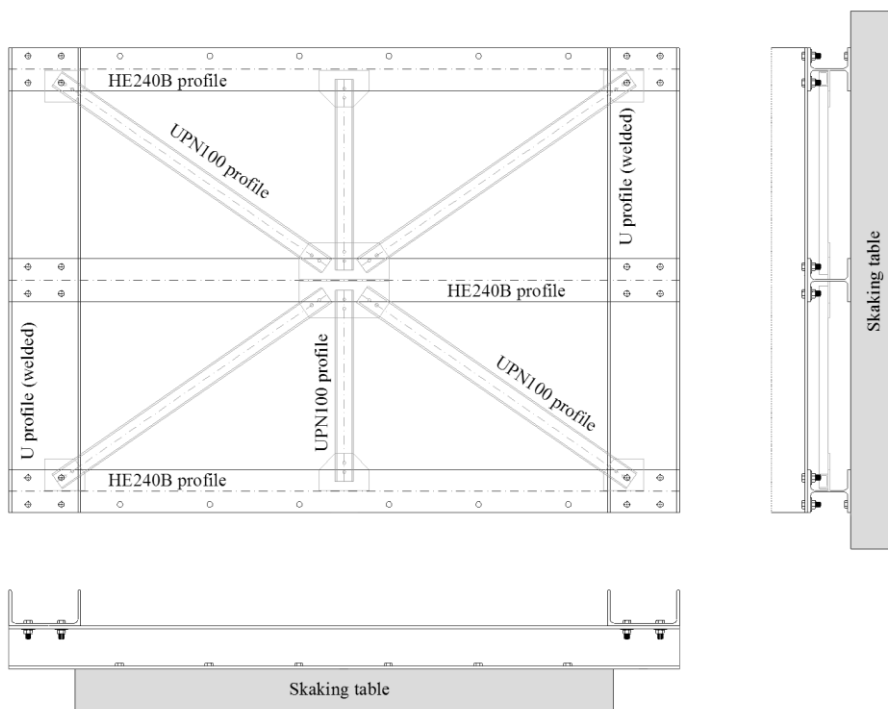


Figure 3.10 Geometry of the steel plane frame (plan and lateral view)

The bracing system trusses are linked to the plane frame by means of bolted connections. The overall dimensions of the plane frame are $3.7 \times 2.6 \text{ m}^2$. The total weight of the testing frame is 12.5 kN. During the testing frame design the main purpose was to prevent any possible influence, of the frame deformability, on the test results. Therefore the testing frame has been designed to be rigid in order to prevent any significant deformation, and it has been verified in the elastic field. Furthermore all the testing frame structural elements have been verified under the following assumptions:

- Material isotropic and perfectly homogeneous.
- Material in elastic field (the Hook's law is valid).
- The cross section remains flat (before and after bending).
- The elastic modulus is the same in tension and compression.

Several verifications have been performed for the testing frame. In the following a brief description of the most relevant verifications has been reported.

U profile (welded): deflection verification

Aim of this section is to verify the deflection of the U shaped two span (three supports) continuous beam (Figure 3.11). The length of each span is 1176 mm. According to the preliminary FE analyses the maximum vertical reacting force is $F_y = 44.8 \text{ kN} \approx 45 \text{ kN}$. This force can be smeared on the total span length, s , (2352 mm) achieving a uniformly distributed load $q_f = 19.13 \text{ N/mm}$.

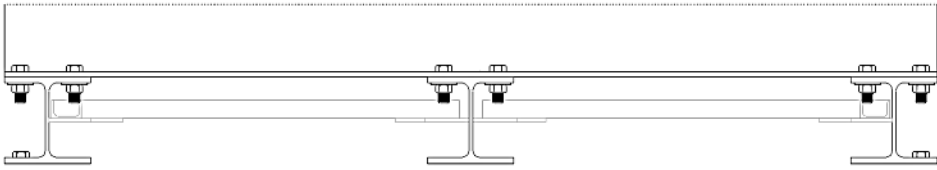


Figure 3.11 Detail of the U shaped beam

The cross section of the beam is a U profile made up of two L profiles welded. Thus, being 0.46 N/mm the weight of the single L profile, the weight of the U profile is $W_U = 0.92$ N/mm. Therefore the total uniformly distributed load which has to be considered is: $q_{tot} = q_f + W_U = 20.05$ N/mm.

On safe side, in the calculation of the maximum deflection, a simply supported beam scheme has been assumed (Figure 3.12).

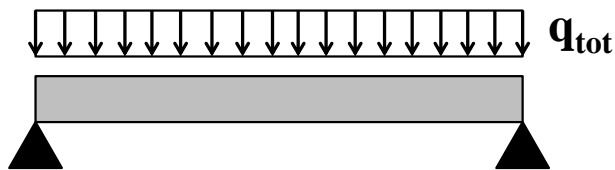


Figure 3.12 Calculation scheme: simple supported beam with uniformly distributed load

The maximum deflection, δ_{max} , has been achieved according to the well-known formulations of the solid mechanics as:

$$\delta_{max} = \frac{5}{384} \frac{s^4 q_{tot}}{EI} = 4.60 \text{ mm} \quad (3.4)$$

Where E is the elastic modulus and I is the second order moment of inertia. In the present case, the achieved maximum deflection (4.6 mm) is widely acceptable. Indeed the δ_{max} is about 1/500 of the span length and the δ_{max}/s ratio is about 0.002.

HE240B profile: shear verification

Since the H shaped beam is longer than the shaking table platform it will work as a cantilever stud beam (Figure 3.13). The length of the cantilever is 370 mm. Aim of this section is to verify that at any cross section the shear strength of the HE240B profile is higher than the shear stress.

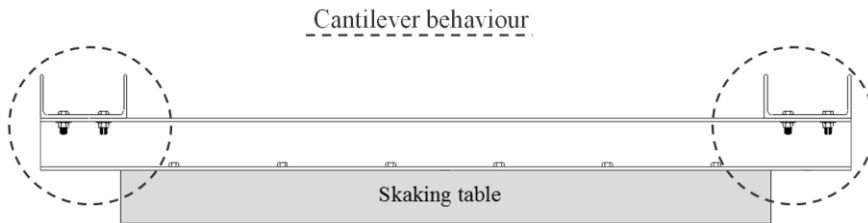


Figure 3.13 Detail of the H shaped beam

A cantilever beam scheme has been adopted (Figure 3.14) at both the sides of the beam. On safe side the half of the maximum achievable vertical reacting force, F_y , has been considered as vertical shear force acting at the end of the cantilever beam. In particular, being the maximum vertical reacting force about 45 kN, the considered force, $T = F_y/2 = 22.5$ kN.

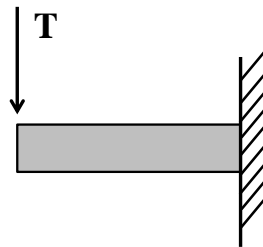


Figure 3.14 Calculation scheme: cantilever beam with point load

The most highly stressed cross section has been considered for the verification. On safe side, the shear contribution of the flanges has been neglected. The maximum shear stress, τ_{\max} , has been achieved, according to the well-known formulations of the solid mechanics, as:

$$\tau_{\max} = \frac{3 T}{2 A} = 14.06 \text{ MPa} \quad (3.5)$$

Where A is cross section area (in this case the contribution of the flanges of the HE240B profile on the shear strength has been neglected).

The shear strength of the HE240B profile has been assessed, according the well-known formulations of the solid mechanics, as:

$$\tau_{res} = \frac{f_y}{\gamma_{M0} \sqrt{3}} = 123.71 \text{ MPa} \quad (3.6)$$

Where f_y is the steel strength and $\gamma_{M0} = 1.05$ is a material partial safety factor. In order to keep the testing frame in elastic field, in the Equation (3.6) the steel strength, f_y , has been assumed as the half of the actual steel strength. This assumption is strong. However, due to both the high variability (uncertainty) of the dynamic load and the lack of examples of comparable structures in literature, at this stage a wide error margin is required. Since $\tau_{res} > \tau_{\max}$ and the τ_{res}/τ_{\max} ratio is about 8.8 the verification is widely satisfied.

U profile-HE240B profile bolted connection: strength verification

Each U shaped beam is connected to a H shaped beam by means of three bolted connections. Each connection is realized by means of four, grade 8.8, bolts having a nominal diameter, d_n , of 30 mm (Figure 3.13).

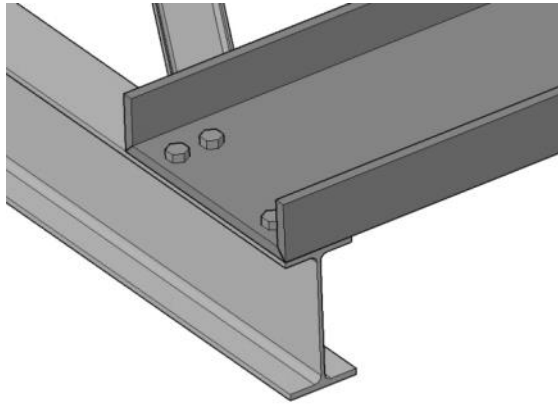


Figure 3.15 detail of the bolted connection: 3D view

Aim of this section is to verify the strength of the bolted connections between the U profile and the HE240B profile. The bolted connection strength has been considered as a function of both the slip coefficient, μ , of the faying surfaces and the clamping force, N_s , provided by the bolts.

According to the preliminary FE analyses the maximum achievable horizontal reacting force is $F_x = 29.87 \text{ kN} \approx 30 \text{ kN}$. The bolt strength can be assessed according to the Italian building code (IBC) [81]. Assuming a bolt tightening torque of 1508 Nm (which corresponds to a clamping force, $N_s = 251 \text{ kN}$) and a slip coefficient $\gamma_f = 0.3$, the strength, F_{lim} , of the single bolt is:

$$F_{\text{lim}} = \frac{n_f \mu N_s}{\gamma_f} = 60 \text{ kN} \quad (3.7)$$

Where n_f is the number of faying surfaces, and $\gamma_f = 1.25$ is a partial safety factor. The horizontal force, F_x , acts on three bolted connections (i.e. on 12 bolts).

Thus the total resistant force of the single connection is 240 kN while the force loading the single connection is $F_x/3 = 10$ kN. Therefore the verification is satisfied. A simplified scheme of the force acting on a single bolted connection is provided in Figure 3.16.

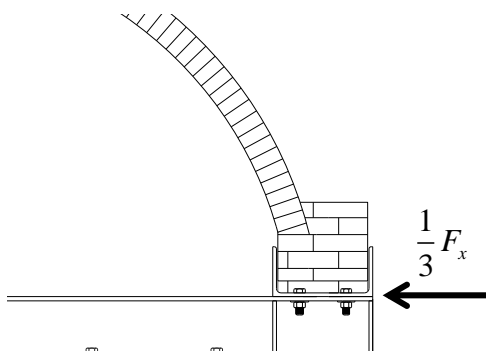


Figure 3.16 Force acting on the single bolted connection

U profile-HE240B profile bolted connection: bearing strength verification

Aim of this section is to verify the bolted connections between the U profile and the HE240B profile against the bearing failure at bolt holes. The nominal diameter of the bolts is 30 mm. The thickness of the thinnest plate involved in the connection (i.e. the U profile) is $t = 15$ mm. The spacing between the bolt holes are: $p_1 = 150$ mm and $e_1 = 45$ mm. Where the dimensions p_1 and e_1 , are defined as shown in figure.

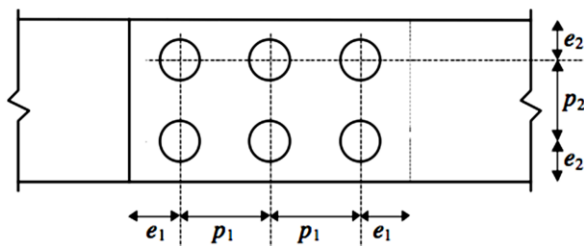


Figure 3.17 Bolt holes spacing reference scheme

According to the Eurocode 3 (EC3) [82] the bearing strength, F_b , can be assessed as:

$$F_b = 2.5 \frac{\alpha_b f_y d_n t}{\gamma_{M2}} = 183.33 \text{ kN} \quad (3.8)$$

Where α_b is defined as the $\min(p_1/3d_n-1/4; f_{ub}/f_y; 1)$ which in this case is 1, f_{ub} is the bolt ultimate strength and $\gamma_{M2} = 1.35$ is a partial safety factor. Being the expected maximum horizontal force $F_x = 30 \text{ kN}$ the verification is satisfied.

3.3.2 Lifting structure design

The lifting structure has been realised by means of steel pipes. Two different thicknesses for the pipes have been used. In particular, the vertical pipes used to link the lifting structure to the steel testing frame are 10 mm thick, while all the other pipes have a thickness of 3 mm. All the joints between the pipes are realised using a commercial pipe connection system commonly used for scaffolding structures. The lifting structure is connected to the testing frame by means of steel plates. In particular each vertical steel pipe is welded onto a steel plate (namely plate class A). The plate class A is bolted onto another plate (namely plate class B). The plate class B is welded to the testing frame (onto the web of the HE240B) by means of another plate (namely plate class C). Two further plates are welded between the plates class B, C and the HE240B profile in order to stiffen the plate class C. A sketch of the connection between the lifting structure and the testing frame is provided in Figure 3.18.

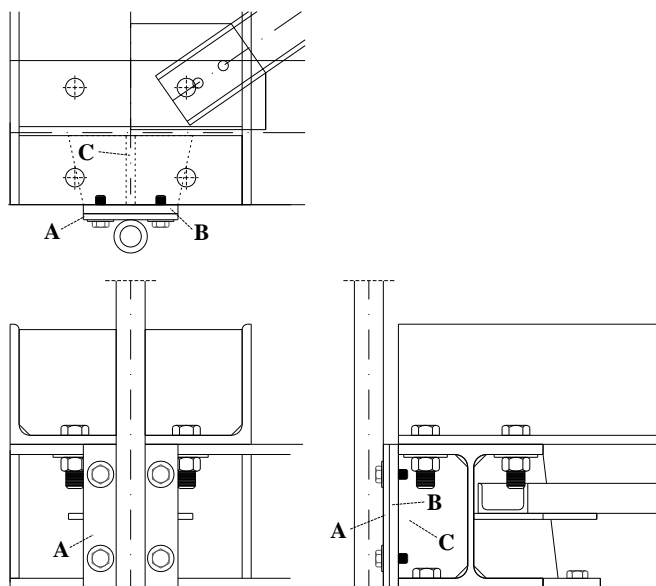


Figure 3.18 Connections between the lifting structure and the testing frame

Numerical FEM analyses have been performed by means of the software SAP2000 developed by CSI [83] in order to simulate the lifting procedure and achieve the axial forces. Each pipe of the lifting structure has been modelled as an elastic truss element (see Figure 3.19). The lifting force (i.e. 41.50 kN) has been achieved as the sum of the total weight of the testing structure including the lifting structure (i.e. 17.22 kN) and the total weight of the specimen (i.e. 24.28 kN).

The maximum axial loads achieved in tension and in compression are: 24.50 kN and 22.10 kN respectively. The maximum vertical reacting force achieved, F_{ly} , is 11.90 kN.

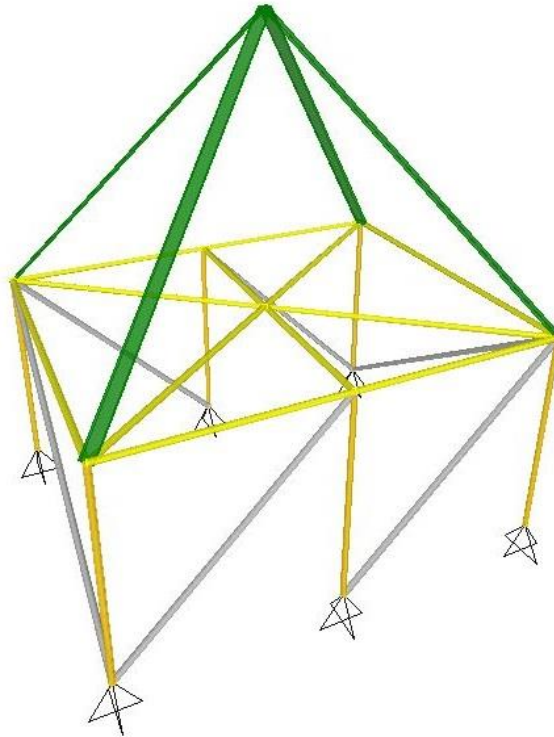


Figure 3.19 FEM model of the lifting/moving system

The main design purpose was to prevent any possible damage to the specimen while lifting (or moving). Therefore the lifting structure has been designed to be rigid in order to prevent any significant deformation, and it has been verified in the elastic field. Furthermore all the lifting structure elements have been verified under the following assumptions:

- Material isotropic and perfectly homogeneous.
- Material in elastic field (the Hook's law is valid).
- The cross section remains flat (before and after bending).
- The elastic modulus is same in tension and compression.

Several verifications have been performed for the lifting structure. In the following a brief description of the most relevant verifications has been reported.

HE240B profile: deflection while lifting verification

The H shaped beams are the elements to which the lifting structure is connected. In particular each beam is connected to the lifting structure in three points (see Figure 3.6). Therefore, aim of this section is to verify the expected deflection of the H shaped beam during the lifting process. Since the connection is realised in three points the beam will behave as a two span (three supports) continuous beam. However, on safe side, a simply supported beam scheme has been assumed. The total span length, s , has been assumed as the distance between the two external connection points (i.e. 3340 mm).

According to the preliminary FE analyses the maximum achievable vertical reacting force is $F_{1s} = 11.90 \text{ kN} \approx 12 \text{ kN}$. Such force, on safe side, has been considered as a point load applied at the midspan of the beam (see Figure 3.20).

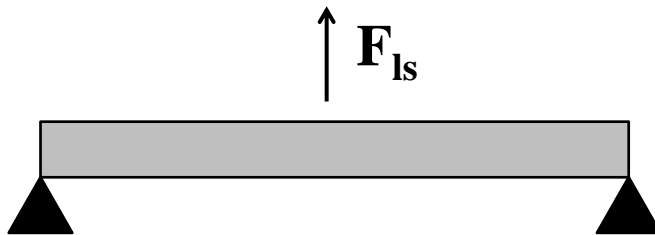


Figure 3.20 Calculation scheme: simply supported beam with point load

The maximum deflection, δ_{\max} , has been achieved, according to the well-known formulations of the solid mechanics, as:

$$\delta_{\max} = \frac{1}{48} \frac{s^3 F_{ls}}{EI} = 0.40 \text{ mm} \quad (3.9)$$

Where E and I are defined as in the previous section 3.3.1. In the present case, the achieved maximum deflection (0.40 mm) is widely acceptable. Indeed the δ_{\max} is about 1/5800 of the span length and the δ_{\max}/s ratio is about 0.0001.

Lifting pipe-plate class A welded connection: strength verification

Each vertical pipe is connected to a plate class A by means of a fillet weld as shown in Figure 3.21.

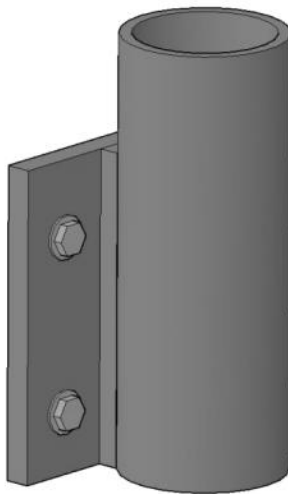


Figure 3.21 Detail of the Lifting pipe-plate class A connection: 3D view

Aim of this section is to verify the strength of the welded connection between the lifting pipe and the plate class A. The stress on the weld critical throat is assumed to be uniform. The following normal and shear stresses have been taken in to account:

$$\left\{ \begin{array}{l} a) \quad \sigma_{\parallel} = \frac{F_{ls}}{2ah} \\ b) \quad \tau_{\perp} = \frac{F_{ls}L_b}{I_x} y \end{array} \right. \quad (3.10)$$

Where $a = b/3$ is the throat, b is the welded plate thickness, h is the height of the weld, L_b is the distance between the weld and the force F_{ls} , I_x is the second order moment of inertia (about the neutral axis x) and y is the perpendicular distance to the neutral axis.

According to the EC3 [82] the verification of the weld strength is satisfied if the following conditions are verified:

$$\left\{ \begin{array}{l} a) \quad \sqrt{\sigma_{\parallel}^2 + (\tau_{\perp}^2 + \tau_{\parallel}^2)} = 13.08 \text{ MPa} \leq \frac{f_y}{\beta_w \gamma_{Mw}} = 196.07 \text{ MPa} \\ b) \quad \sigma_{\perp} = 17.84 \text{ MPa} \leq \frac{F_y}{\gamma_{Mw}} = 166.66 \text{ MPa} \end{array} \right. \quad (3.11)$$

Where $\beta_w = 0.85$ is a coefficient related to steel typology and $\gamma_{Mw} = 1.35$ is a partial safety factor. It is worth noting that, due to the geometrical configuration of the weld, in this case τ_{\parallel} is equal to zero.

3.4 Instrumentation

The monitoring of the vault has been achieved by means of seven accelerometers and two laser-optical displacement sensors. In Figure 3.22 and Figure 3.23 the positions of the sensors are indicated.

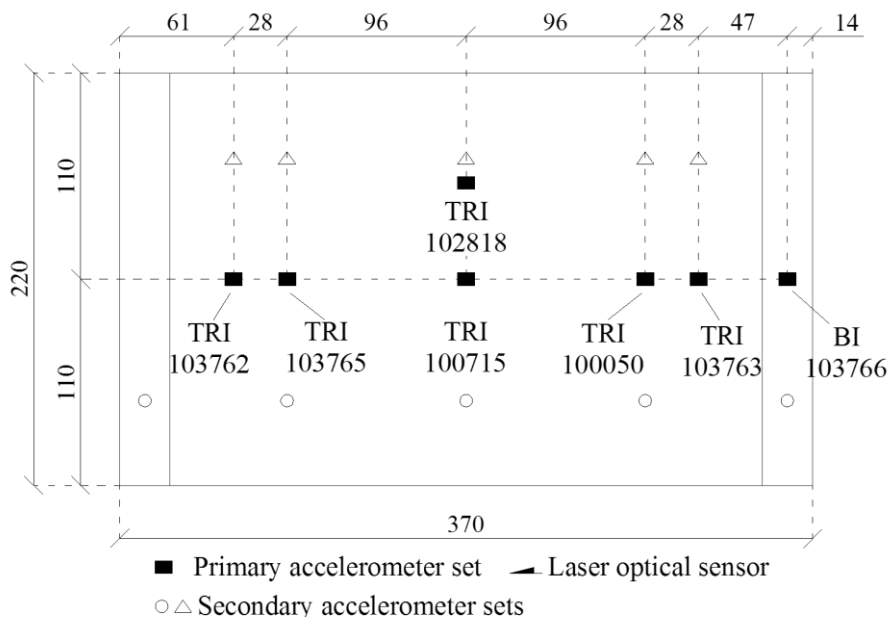


Figure 3.22 Instrumentation layout: plan view (dimensions in cm)

Six tri-axial accelerometers and one bi-axial accelerometer are placed along the extrados of the vault at the longitudinal midplane. In particular one accelerometer, namely TRI-100715, was placed at the keystone location. Two accelerometers, namely TRI-103765 and TRI-100050, were placed on the left and right side respectively at 45° from the keystone. Two accelerometers, namely TRI-103763, and TRI-103762, were placed on the left and right side respectively at 60° from the keystone. In order to measure contingent torsional effects, an accelerometer, namely TRI-102818, was placed at the keystone location but on a different vertical plane. Finally, one bi-axial accelerometer, namely BI-103766 was placed on the left imposts of the vault to check the actual acceleration input transmitted to the vault. With the purpose of checking the output recorded by the main instrumentation, two more secondary accelerometer sets were placed in parallel, at the same locations as the set

mentioned above but on different vertical planes. In order to measure the horizontal displacements, two laser-optical sensors, namely L1 and L2, were placed along the extrados of the vault at the longitudinal midplane. In particular, the sensor L1 was placed at the keystone location, and the sensor L2 was placed on the left side at 45° from the keystone.

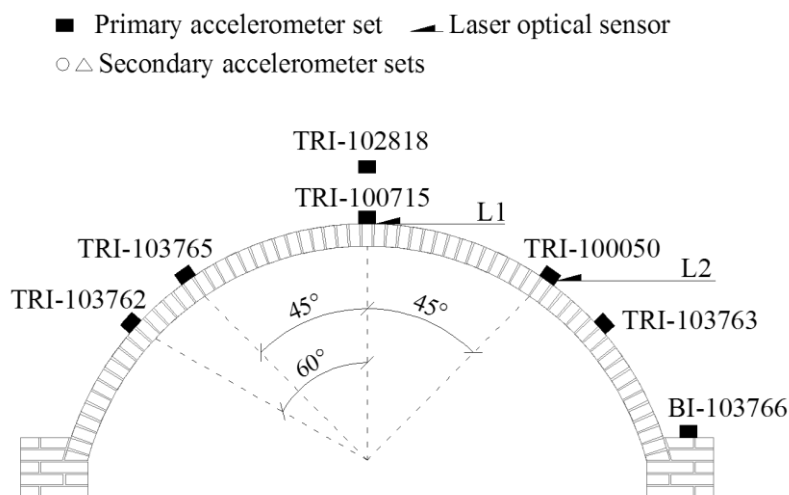


Figure 3.23 Instrumentation layout: front view (dimensions in cm)

3.5 Input and test programme

The seismic behaviour of the masonry vault has been investigated by means of two sets of time-history accelerograms namely “STR” and “ART” respectively. The STR set consists of five tests. The time-history used is a natural accelerogram recorded in Southern Italy by the station of Sturno during the Irpinia earthquake occurred on November 23rd 1980. The total duration of the accelerogram is 72 s. The PGA is 1.78 m/s^2 (see Figure 3.24a). The accelerogram has been scaled by different factors in order to get a progressive

PGA increase (0.25, 0.50, 0.75, 1.00 and 1.50). Consequently, the test sequence in terms of PGA was the following: 0.44, 0.89, 1.33, 1.78 and 2.67 m/s².

The ART set consists of seven tests. The time-history used as base is an artificial accelerogram obtained from a non-stationary broadband random excitation having an energy content ranging from 1 to 30 Hz. The drive signal composition is obtained as multiple-frequency random excitations. The total duration of the accelerogram is 30 s. The accelerogram has a PGA of 4.50 m/s² (see Figure 3.24b).

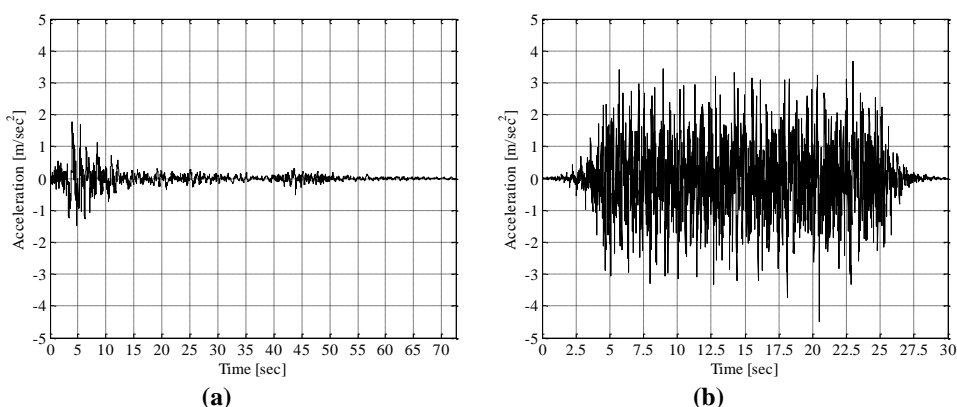


Figure 3.24 Time-history accelerograms at 100% intensity: (a) STR; (b) ART;

The time-history is scaled by different factors in order to get a progressive PGA increase (0.10, 0.20, 0.30, 0.40, 0.50, 0.75, 1.00). Consequently, the test sequence in terms of PGA was the following: 0.45, 0.90, 1.35, 1.80, 2.25, 3.38, and 4.50 m/s². The two sets of time-history accelerograms cover two different frequency ranges being the STR mainly limited to 15 Hz, while the second ART is up to 30 Hz (Fast Fourier Transforms, FFT, in Figure 3.25a and b).

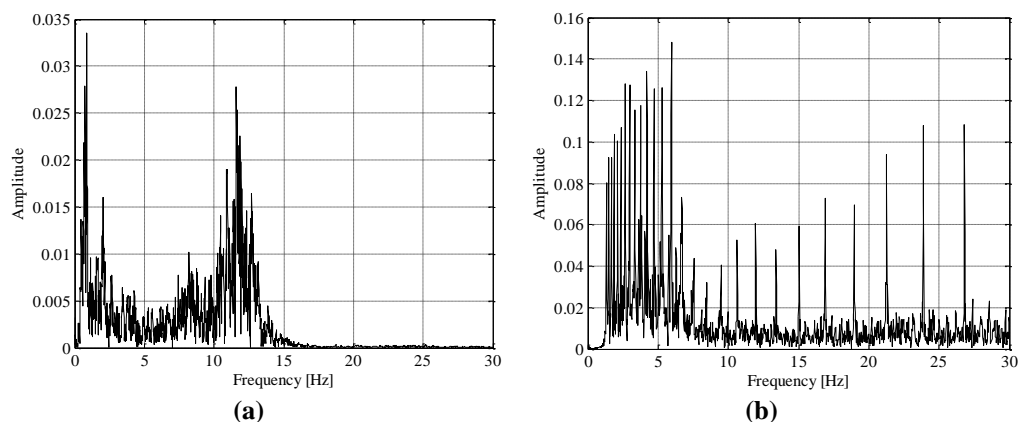


Figure 3.25 Time-history accelerograms at 100%: (a) FFT STR; (b) FFT ART.

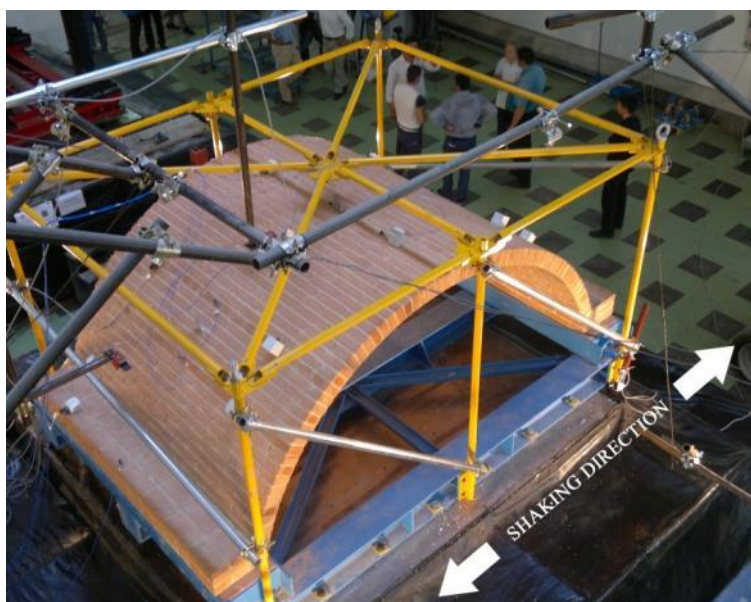
Preliminarily, a set of random accelerograms were performed on dynamic identification purpose (natural frequency and damping). The random set, namely “RND” was performed by means of four tests. In particular, an input random accelerogram scaled at different PGA levels (0.25, 0.50, 0.75 and 1.00 m/s^2) was used as the input. The total duration of the random vibration is 60 s. Table 3.2 lists the complete experimental test programme.

It is worth noting that the desired PGA does not exactly match with the achieved PGA (actual value of the maximum acceleration transmitted at the specimen by the shaking table motion). This aspect may be crucial for experimental tests on shaking table especially on specimens made of brittle material like masonry. For this reason, the procedure described in [84], concerning the optimisation of the drive motion to predict the signal recorded at desired locations, i.e. on the keystone, using a compensation procedure, has been taken into account in the experimental programme.

All the tests of the experimental program are unidirectional with the shaking movement applied in the transversal direction of the vault (Figure 3.26).

Table 3.2: Experimental test programme (unreinforced vault).

Test ID	Scale factor	Desired PGA [m/s^2]	Achieved PGA [m/s^2]
RND1	0.25	0.25	0.26
RND2	0.50	0.50	0.52
RND3	0.75	0.75	0.89
RND4	1.00	1.00	1.29
STR1	0.25	0.44	0.53
STR2	0.50	0.89	1.04
STR3	0.75	1.33	1.54
STR4	1.00	1.78	2.13
STR5	1.50	2.67	3.52
ART1	0.10	0.45	0.39
ART2	0.20	0.90	0.85
ART3	0.30	1.35	1.27
ART4	0.40	1.80	1.81
ART5	0.50	2.25	2.30
ART6	0.75	3.38	3.24
ART7	1.00	4.50	4.67

**Figure 3.26** Test setup and specimen: shaking direction (unreinforced vault).

3.6 Outcomes of the shaking table tests

The main results of the experimental tests are described in the following sections. The outcomes are grouped by test set, according to the set naming defined in the previous section 3.5.

3.6.1 RND test results (Dynamic identification)

The natural frequency and the damping ratio have been evaluated by means of a dynamic identification procedure. Using a random time-history in acceleration as input signal, a sequence of four shakings has been performed scaling the signal from a PGA of 0.25 m/s^2 to 1.0 m/s^2 . It's worth noting that a low intensity signal has been used in the dynamic identification phase to prevent premature damage on the specimen. The natural frequency has been assessed according to the transfer curve method. The decay of the natural frequency evidenced by the transfer function amplitude is shown in Figure 3.27.

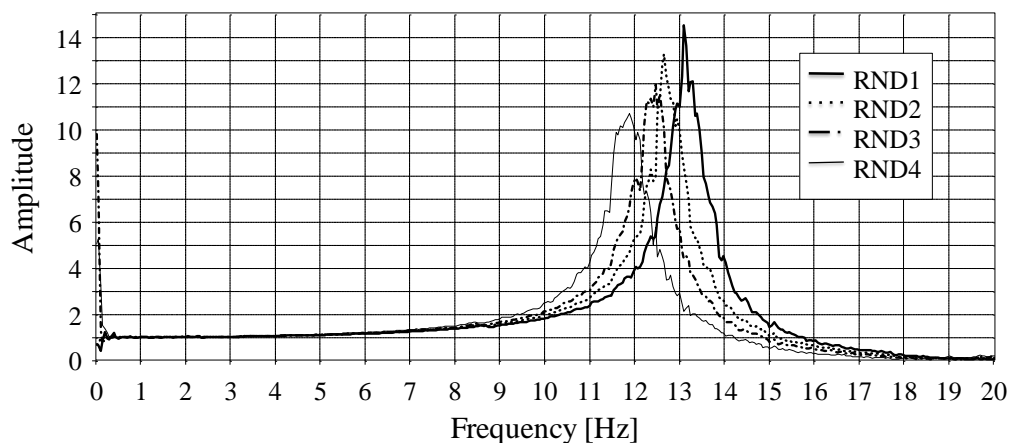


Figure 3.27 Natural frequency decay of the specimen (unreinforced vault).

The first shaking at a PGA of 0.25 m/s^2 (RND1) provided a natural frequency of about 13.1 Hz. That result remarks the high stiffness of the vault.

The further three tests (i.e. RND2, RND3 and RND4) have shown a decay of the natural frequency due to premature minor damage (microcracking) of the specimen. The damping ratio, ζ , has been achieved according to the well-known half-power bandwidth method as:

$$\zeta = \frac{\omega_2 - \omega_1}{2\omega_k} \quad (3.12)$$

Where ω_k is the natural frequency, ω_2 and ω_1 are the frequencies for which the power input is half the input at resonance [85]. The tested structure has shown a damping ratio, ζ , ranging between 2.2% and 3.2%. Table 3.3 lists both the fundamental frequency and damping ratio achieved for each test.

Table 3.3: Natural frequencies and damping ratios (unreinforced vault).

Test ID	Natural frequency [Hz]	Damping ratio [%]
RND1	13.1	2.2%
RND2	12.6	2.2%
RND3	12.4	2.2%
RND4	11.7	3.2%

3.6.2 STR test results (Sturno earthquake)

As described in the previous section 3.5, the input accelerogram used for these tests is a natural accelerogram recorded in southern Italy during the 1980 Irpinia earthquake. The record has a PGA of 1.78 m/s².

A sequence of five tests has been performed, applying to the natural accelerogram scaling factors equal to: 0.25, 0.50, 0.75, 1.00 and 1.50 (see Table 3.2). For the test performed at 100% level intensity (STR4), the horizontal component of the achieved time histories recorded at the imposts (BI-103766) and at the keystone (TRI-100715) of the vault are shown in Figure 3.28a. The relative displacement time-history (keystone-imposts) is shown in Figure 3.28b. The outcomes are presented in terms of maximum accelerations, maximum displacements, and detected damage to the specimen.

Both the horizontal and vertical accelerations have been recorded in five locations according to the instrumentation scheme shown in Figure 3.22 and Figure 3.23. All the accelerometers recorded the maximum horizontal accelerations during the last test of the set (i.e. test STR5). In particular the maximum horizontal acceleration has been recorded by the accelerometer TRI-100765, placed at 45° from the keystone location.

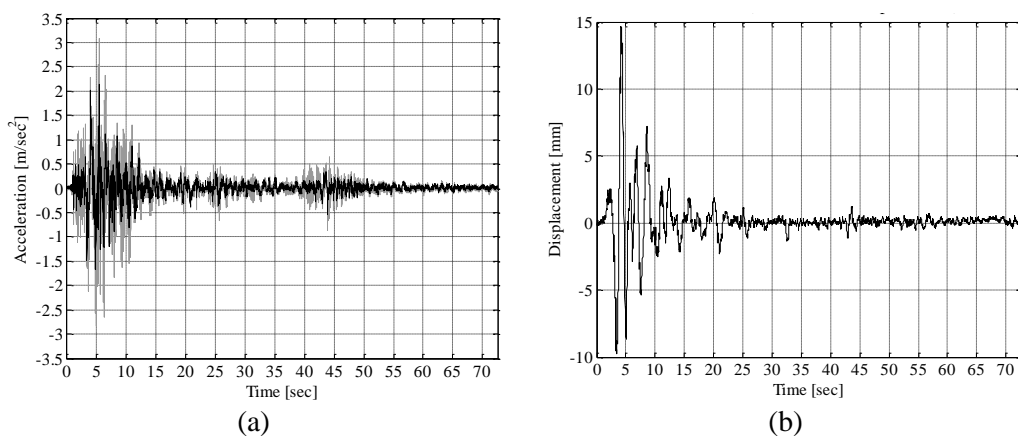


Figure 3.28 Sturno earthquake, test STR4: recorded time-history in acceleration at the impost (in black) and keystone (in grey) of the vault (a) and relative keystone-impost displacement (b).

This acceleration of 5.21 m/s^2 has a dynamic magnification of about 48% compared to the PGA of the achieved shaking table motion (i.e. 3.52 m/s^2).

At the keystone location (i.e. accelerometer TRI-100715) the maximum recorded acceleration is 4.28 m/s^2 with a dynamic magnification of about 22% compared to the recorded shaking table PGA (i.e. 3.52 m/s^2).

Furthermore, since the difference between the values of the accelerations recorded by the two accelerometers, at the keystone location (i.e. TRI-100715 and TRI-102818), is small (it ranges between 1% and 2%), the torsional effects can be considered negligible. The maximum vertical acceleration, equal to 5.06 m/s^2 , has been recorded during the test STR5 by the accelerometer TRI-103762 (see Figure 3.22 and Figure 3.23). In Figure 3.29 the results, in terms of maximum accelerations, are plotted as profiles.

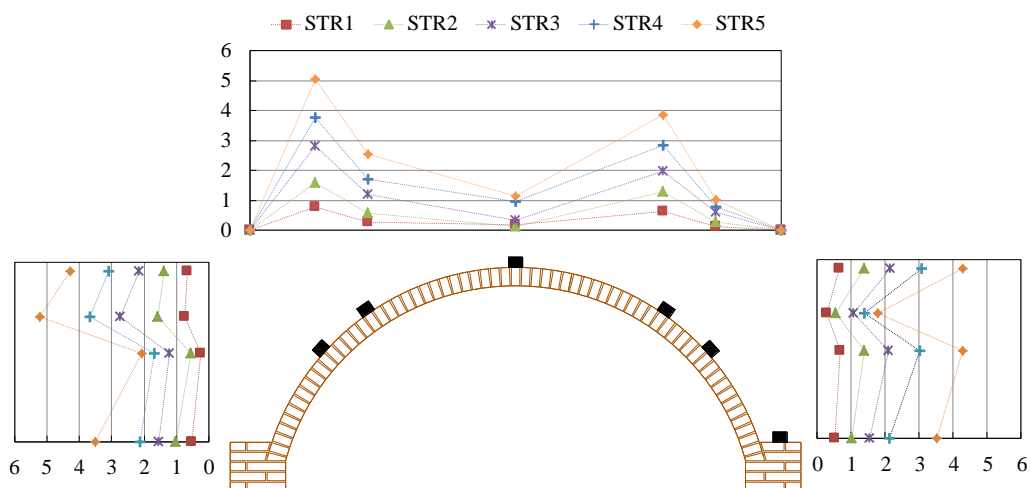


Figure 3.29 STR: Maximum acceleration profiles (values expressed in m/s^2).

The profiles show that the trends of the maximum accelerations (horizontal and vertical) do not change when varying the magnitude of the base acceleration. Furthermore the maximum acceleration profiles highlight a not symmetric

dynamic behaviour. In particular the maximum horizontal accelerations on the right side of the vault were recorded at both the keystone and 60° from the keystone locations (i.e. accelerometers TRI-103763 and TRI-100715). Otherwise, on the left side of the vault the maximum horizontal accelerations were recorded at 45° from the keystone location (i.e. accelerometer TRI-103765). The horizontal and vertical maximum recorded accelerations are reported in Table 3.4 and Table 3.5 respectively.

Table 3.4: STR test results: horizontal maximum accelerations.

TEST ID	TRI-100715 [m/s ²]	TRI-102818 [m/s ²]	TRI-103765 [m/s ²]	TRI-103762 [m/s ²]	TRI-100050 [m/s ²]	TRI-103763 [m/s ²]
STR1	0.66	0.67	0.75	0.26	0.29	0.68
STR2	1.39	1.41	1.57	0.57	0.56	1.39
STR3	2.17	2.19	2.74	1.21	1.09	2.11
STR4	3.08	3.13	3.66	1.69	1.40	3.02
STR5	4.28	4.33	5.21	2.06	1.79	4.27

Table 3.5: STR test results: vertical maximum accelerations.

TEST ID	TRI-100715 [m/s ²]	TRI-102818 [m/s ²]	TRI-103765 [m/s ²]	TRI-103762 [m/s ²]	TRI-100050 [m/s ²]	TRI-103763 [m/s ²]
STR1	0.18	0.24	0.28	0.78	0.66	0.14
STR2	0.14	0.25	0.57	1.60	1.28	0.28
STR3	0.32	0.45	1.21	2.82	1.97	0.60
STR4	0.98	1.21	1.70	3.77	2.85	0.78
STR5	1.14	1.19	2.56	5.06	3.87	1.04

The horizontal dynamic amplifications in terms of percentage have been evaluated as:

$$Amplification = \frac{Acc_{out} - Acc_{in}}{Acc_{in}} \quad (3.13)$$

Where Acc_{out} is the maximum acceleration recorded at the considered location, while Acc_{in} is the PGA of the achieved motion of the table. The horizontal dynamic amplifications in terms of percentage are plotted as profiles in Figure 3.30

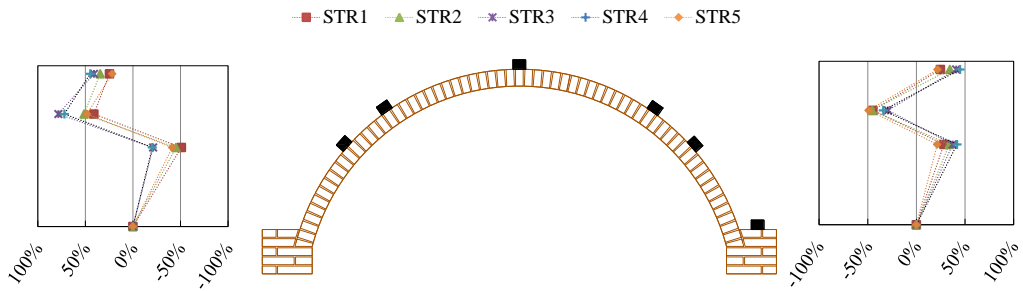


Figure 3.30 STR: Horizontal dynamic amplifications (values expressed in %).

The profiles show that the magnitude of the base acceleration does not have a strong impact on the trends of the horizontal dynamic amplifications. The horizontal dynamic amplifications profiles exhibit a not symmetric trend. As expected the maximum horizontal amplifications on the right side of the vault were achieved at both the keystone and 60° from the keystone locations. On the left side of the vault the maximum horizontal accelerations were achieved at 45° from the keystone location. The horizontal dynamic amplifications achieved are reported in Table 3.6. Vertical dynamic amplification cannot be evaluated since no vertical acceleration was imposed to the vault.

Table 3.6: STR test results: dynamic amplifications.

TEST ID	TRI- 100715 [%]	TRI- 102818 [%]	TRI- 103765 [%]	TRI- 103762 [%]	TRI- 100050 [%]	TRI- 103763 [%]
STR1	25%	27%	41%	-51%	-45%	28%
STR2	34%	36%	51%	-45%	-46%	34%
STR3	41%	42%	78%	-21%	-29%	37%
STR4	45%	47%	72%	-20%	-34%	42%
STR5	22%	23%	48%	-41%	-49%	21%

The maximum relative displacement measured at the keystone location (i.e. laser-optical sensor L1, see Figure 3.23) ranges between 2.92 mm and 17.41 mm from test STR1 to STR5. The same increasing trend has been shown by the laser-optical sensor, L2, placed on the left side of the vault (see Figure 3.23). In particular, the maximum relative displacements measured by the L2 sensor range between 3.28 mm and 7.41 mm from test STR1 to STR5. Except for the STR1 test, in which the relative displacement measured by the two sensors is comparable, the displacements measured by the sensor L2 are always widely lower than those measured by the sensor L1. The maximum relative displacements are shown in detail in Table 3.7.

Table 3.7: STR test results: maximum relative displacements.

Test ID	L1 [mm]	L2 [mm]
STR1	2.92	3.28
STR2	7.86	3.81
STR3	11.63	4.86
STR4	14.44	5.62
STR5	17.41	7.41

In order to detect damages to the vault, after each test, the specimen has been inspected. However even after the last test (i.e. test STR5) the specimen damages were not relevant. In particular very slight cracking, at the interface between mortar and brick, has been observed.

3.6.3 ART test results (artificial earthquake)

As described in the previous section 3.5, the input used is an artificial accelerogram specifically designed for the tests. A sequence of seven tests was performed increasing the PGA of the table drive motion up to 4.50 m/s^2 (4.67 m/s^2 recorded). For the test performed at 100% level intensity (ART7), the horizontal component of the achieved time histories recorded at the impost (BI-103766) and at the keystone (TRI-100715) of the vault are shown in Figure 3.31a. The relative displacement time-history (keystone-impost) is shown in Figure 3.31b.

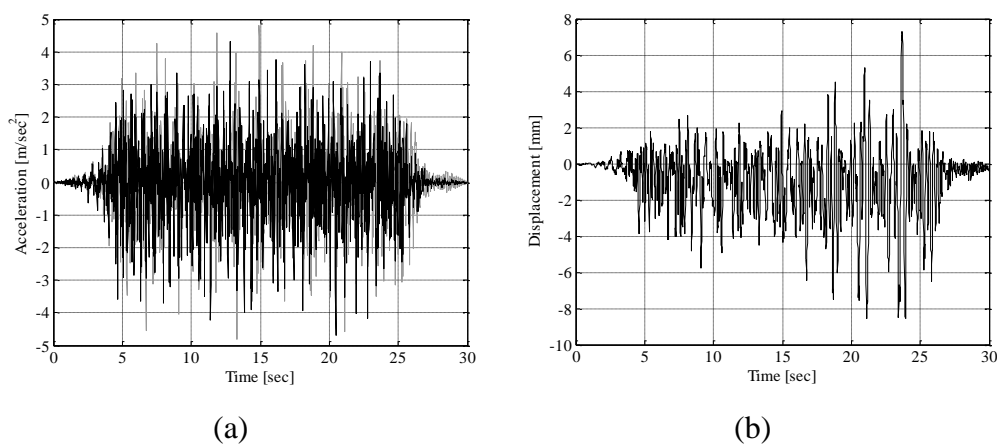


Figure 3.31 Artificial earthquake, test ART7: (a) recorded time-history in acceleration at the impost (in black) and keystone (in grey) of the vault; (b) relative keystone-impost displacement.

The complete testing sequence is reported in Table 3.2. The outcomes are presented in terms of maximum accelerations, maximum displacements, and detected damage to the specimen.

Both the horizontal and vertical accelerations have been recorded in five locations according to the instrumentation scheme represented in Figure 3.22 and Figure 3.23.

The maximum horizontal acceleration was recorded by the accelerometer TRI-103763 during the last test (i.e. test ART7). The recorded acceleration was 7.64 m/s^2 . The magnification was of about 64% compared to the recorded PGA of the table (i.e. 4.67 m/s^2). At the keystone location (i.e. accelerometer TRI-100715) the maximum acceleration was recorded during the test ART7. The recorded acceleration was 4.80 m/s^2 having a dynamic magnification of about 3% compared to the recorded PGA (i.e. 4.67 m/s^2). The maximum vertical accelerations were recorded by all the accelerometers during the last test of the set (i.e. test ART7). In particular the maximum vertical acceleration was 7.51 m/s^2 and it is recorded by the accelerometer TRI-103762. In Figure 3.32 the results, in terms of maximum accelerations, are plotted as profiles.

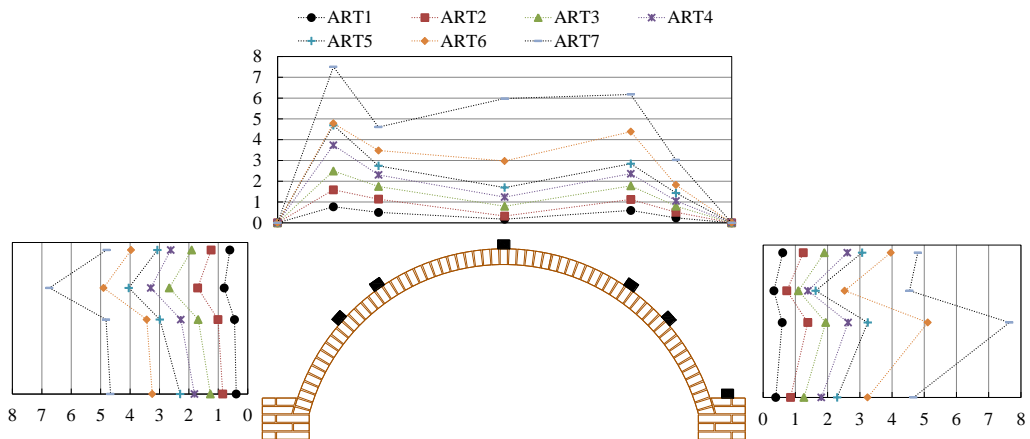


Figure 3.32 ART: Maximum acceleration profiles (values expressed in m/s^2).

The profiles show that the trends of the maximum accelerations (horizontal and vertical) do not change when varying the magnitude of the base acceleration (except for the last ART7 test). In the ART7 test the maximum vertical acceleration profile show a sharp change in the trend (compared with the previous tests). A possible reason for this sharp change is a damage localised at that location.

As in the previous tests (i.e. STR), the acceleration profiles highlight a not symmetric dynamic behaviour. In particular the maximum horizontal accelerations on the right side of the vault were recorded at both the keystone and 60° from the keystone locations (i.e. accelerometers TRI-103763 and TRI-100715). Otherwise, on the left side of the vault the maximum horizontal accelerations were recorded at 45° from the keystone location (i.e. accelerometer TRI-103765). The horizontal and vertical maximum recorded accelerations are reported in Table 3.8 and Table 3.9 respectively.

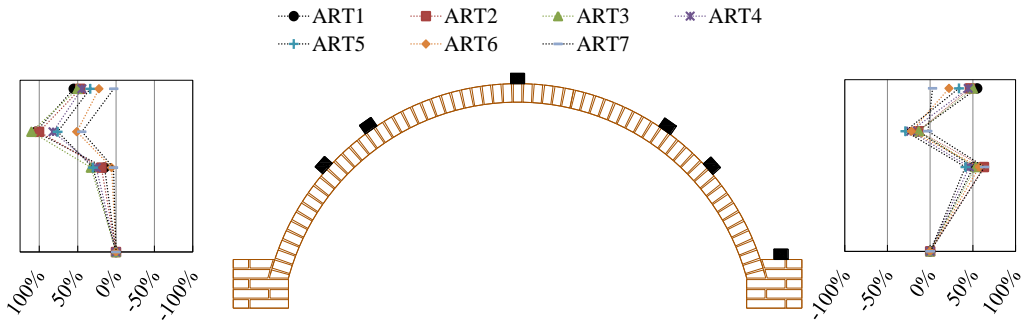
Table 3.8: ART test results: horizontal maximum accelerations.

TEST ID	TRI-100715 [m/s²]	TRI-102818 [m/s²]	TRI-103765 [m/s²]	TRI-103762 [m/s²]	TRI-100050 [m/s²]	TRI-103763 [m/s²]
ART1	0.61	0.62	0.80	0.45	0.33	0.59
ART2	1.24	1.25	1.70	1.01	0.73	1.38
ART3	1.90	1.94	2.67	1.68	1.10	1.94
ART4	2.62	2.66	3.29	2.27	1.39	2.64
ART5	3.07	3.06	4.04	2.99	1.63	3.25
ART6	3.96	4.08	4.90	3.43	2.53	5.11
ART7	4.80	4.83	6.74	4.82	4.54	7.64

Table 3.9: ART test results: vertical maximum accelerations.

TEST ID	TRI- 100715 [m/s ²]	TRI- 102818 [m/s ²]	TRI- 103765 [m/s ²]	TRI- 103762 [m/s ²]	TRI- 100050 [m/s ²]	TRI- 103763 [m/s ²]
ART1	0.17	0.23	0.50	0.77	0.60	0.24
ART2	0.32	0.49	1.14	1.59	1.12	0.51
ART3	0.80	0.99	1.75	2.49	1.78	0.80
ART4	1.24	1.48	2.31	3.74	2.36	1.05
ART5	1.70	1.68	2.74	4.69	2.84	1.44
ART6	2.97	3.27	3.48	4.79	4.39	1.82
ART7	5.98	5.86	4.61	7.51	6.18	3.03

The horizontal dynamic amplifications, evaluated as shown in the Equation (3.13), are plotted as profiles in terms of percentage in Figure 3.33.

**Figure 3.33** ART: Horizontal dynamic amplifications (values expressed in %).

According to the dynamic amplification profiles, the magnitude of the input acceleration does not have a strong impact on the trends of the horizontal dynamic amplifications. The horizontal dynamic amplifications profiles exhibit a not symmetric trend.

As expected the maximum horizontal amplifications on the right side of the vault were achieved at both the keystone and 60° from the keystone locations. On the left side of the vault the maximum horizontal accelerations were

achieved at 45° from the keystone location. The horizontal dynamic amplifications achieved are reported in Table 3.10.

Table 3.10: ART test results: dynamic amplifications.

TEST ID	TRI- 100715 [%]	TRI- 102818 [%]	TRI- 103765 [%]	TRI- 103762 [%]	TRI- 100050 [%]	TRI- 103763 [%]
ART1	55%	59%	105%	15%	-15%	51%
ART2	47%	47%	100%	19%	-14%	63%
ART3	50%	53%	110%	33%	-13%	53%
ART4	45%	47%	82%	26%	-23%	46%
ART5	34%	33%	76%	30%	-29%	41%
ART6	22%	26%	51%	6%	-22%	58%
ART7	3%	3%	44%	3%	-3%	64%

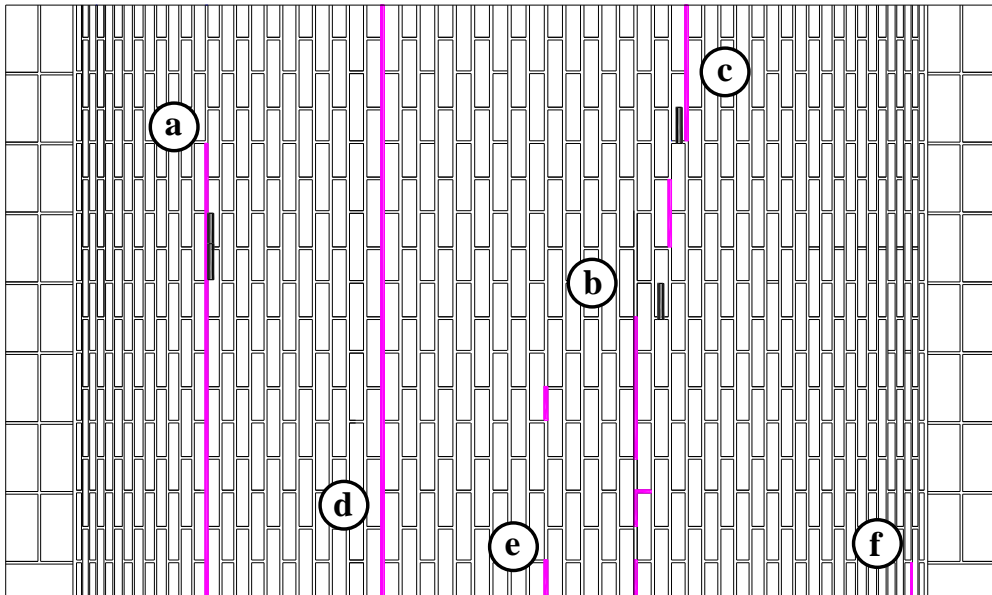
The maximum relative displacement measured at the keystone location (i.e. laser-optical sensor L1, see Figure 3.23) ranges between 1.35 mm and 8.57 mm from test ART1 to ART7. The same increasing trend has been shown by the laser-optical sensor, L2, placed on the left side of the vault (see Figure 3.23). In particular the maximum relative displacement measured by the L2 sensor ranges between 0.70 mm and 11.12 mm from tests ART1 to ART7. Except for the last test (i.e. ART7) in which the displacement measured by the sensor L1 is lower than the one measured by the sensor L2, the key section always shows a relative displacement larger than the side of the vault. The maximum relative displacements are shown in detail in Table 3.11

Table 3.11: ART test results: maximum relative displacements.

Test ID	L1 [mm]	L2 [mm]
ART1	1.35	0.70
ART2	2.03	1.06
ART3	2.86	1.74
ART4	3.77	2.25
ART5	3.98	2.36
ART6	5.50	3.00
ART7	8.57	11.12

In order to detect damages to the vault, after each test, the specimen has been inspected. Only after the last test (i.e. test ART7) slight damages were observed. However, evident cracking at the interface between mortar and brick has been observed at both intrados and the extrados of the vault. In particular, as shown in Figure 3.34, at the intrados, interface cracking occurred, in a few joints, along its entire depth. Interface cracking occurred at the extrados as well. However, at the extrados, the cracking has involved a larger number of joints. Due to excessive local compressive stress concentrations, few minor detachments of the brick edges have been observed.

In the following figures a comprehensive overview on the damages observed is provided. In particular, Figure 3.34 and Figure 3.35, show the damages at the intrados and at the extrados of the vault respectively.



a

b

c



d

e

f



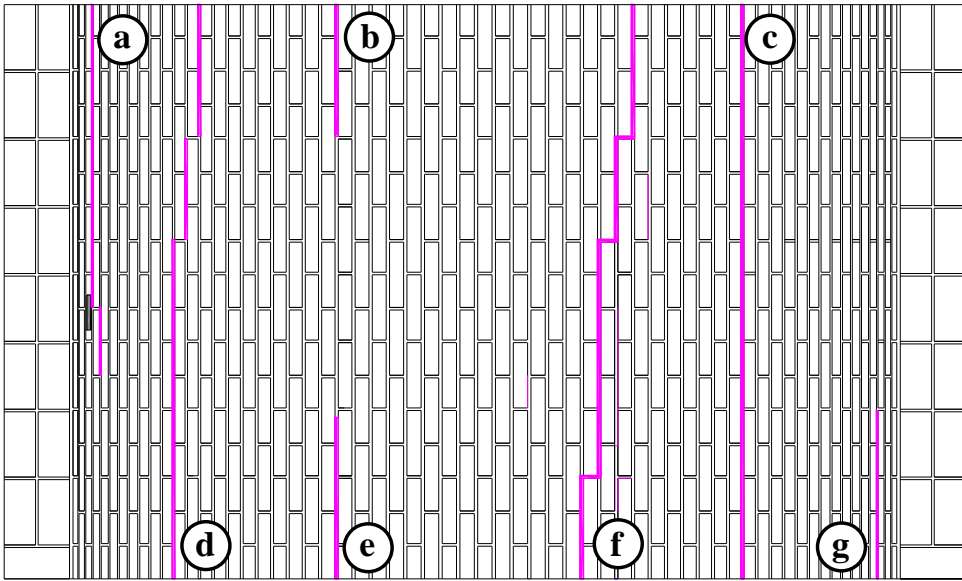
 Interface cracking
 Brick edge detachment

Figure 3.34 Unreinforced vault: damages detected (intrados)



(a)

(b)

(c)



(d)

(e)

(f)

(g)



 Interface cracking
 Brick edge detachment

Figure 3.35 Unreinforced vault: damages detected (extrados)

3.7 Conclusions

The dynamic behaviour of the masonry vault has been investigated by means of shaking table tests. In particular, two sets of time-history accelerograms (natural and artificial) have been used as input signal. Preliminarily, a set of random accelerograms were performed on dynamic identification purpose. The results of the shaking tests have been presented in terms of dynamic characteristics (natural frequency and damping ratio), maximum accelerations, maximum displacements, time histories and observed damage to the specimen.

In the case of unreinforced vault, a natural frequency of 13.1 Hz and a damping ratio ranging between 2.2% and 3.2% have been evaluated. The outcomes, in terms of accelerations measured on the structure, highlighted a dynamic amplification of the base horizontal excitation. Furthermore, although the shaking is applied only in the horizontal direction, significant vertical accelerations have been detected. The tested structure exhibits good seismic behaviour, showing very slight damage only after the last test performed with an achieved PGA of 4.67 m/s^2 . In particular, cracking at the interface between mortar and brick has been observed at both the intrados and the extrados of the vault.

Chapter 4

Experimental tests: retrofitted vault

Since the previous shaking table tests (see Chapter 3) resulted in a slight damage of the vault, it was possible to retrofit the vault. Then shaking table tests have been performed on the retrofitted vault.

The experimental programme presented in this chapter aims to investigate the behaviour of a retrofitted masonry vault subjected to a dynamic base excitation. Furthermore, in the cases of comparable dynamic input, a comparison with the previous unreinforced vault tests allowed to investigate the effect of the retrofit. A comprehensive overview of the results of the shaking table tests is presented and discussed. As well as in the previous tests (see Chapter 3), the vault has been tested without any vertical load acting at the extrados. Furthermore the vault is constrained on the shaking table. Therefore the outcome represents the behaviour of the retrofitted vault once the settlement and capacity of the supports of the vaults, (e.g. imposts, masonry piers, load bearing walls) is guaranteed.

4.1 Specimen retrofit

As discussed in the previous section 2.4.1, the first step of a proper retrofit is “*an accurate survey of the structure in order to assess the main vulnerabilities and potential instability sources*”. Therefore, according to the slight damages detected on the unreinforced vault after the last test (section 3.6.3), the retrofit has been performed by coupling three different techniques. In particular: repointing of the cracked joints (Figure 4.1 and Figure 4.2), grout injections (Figure 4.3) and IMG (Figure 4.4).

The repointing has been performed both at the front section (Figure 4.1) and at the intrados of the vault (Figure 4.2) by means of a commercial repair mortar (i.e. MAPEI *MAPE Antique fc ultrafine*).

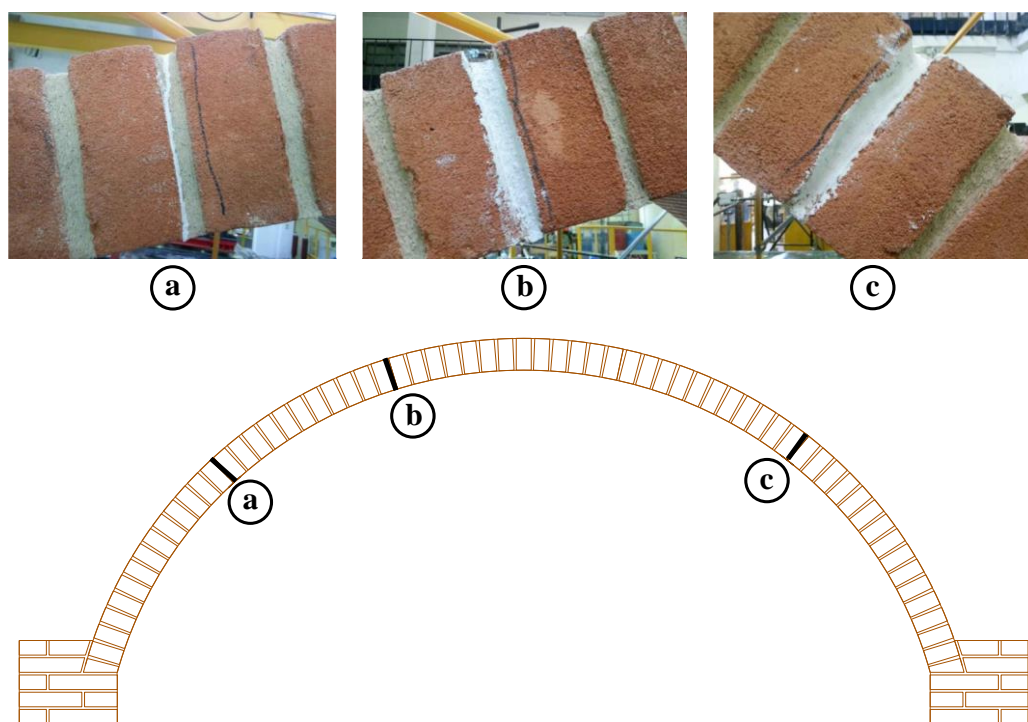
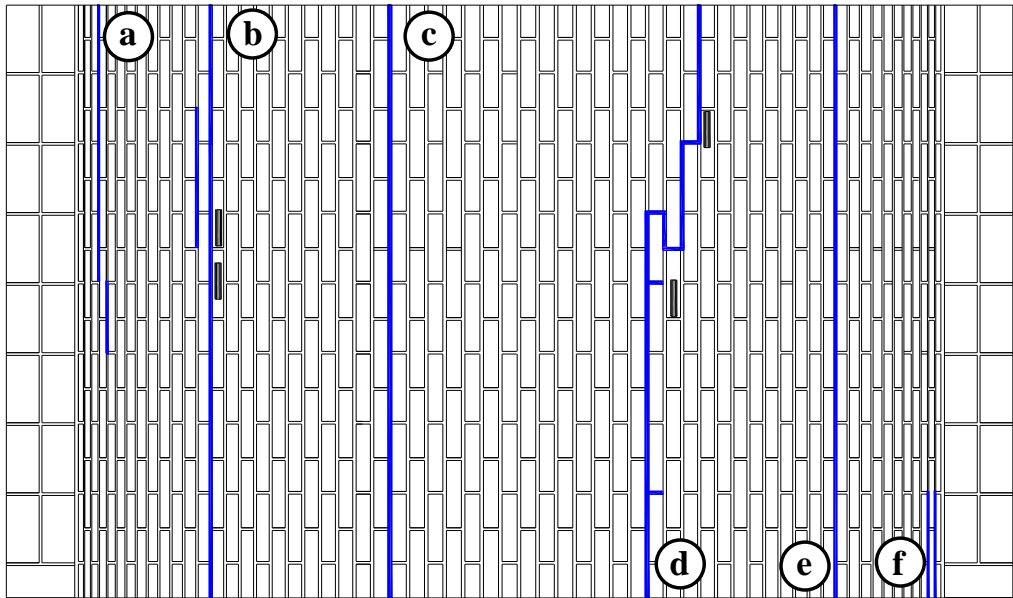


Figure 4.1 Repointing of the cracked joints at the front of the vault.



(a)



(b)



(c)



(d)



(e)



(f)

Figure 4.2 Repointing of the cracked joints at the intrados of the vault

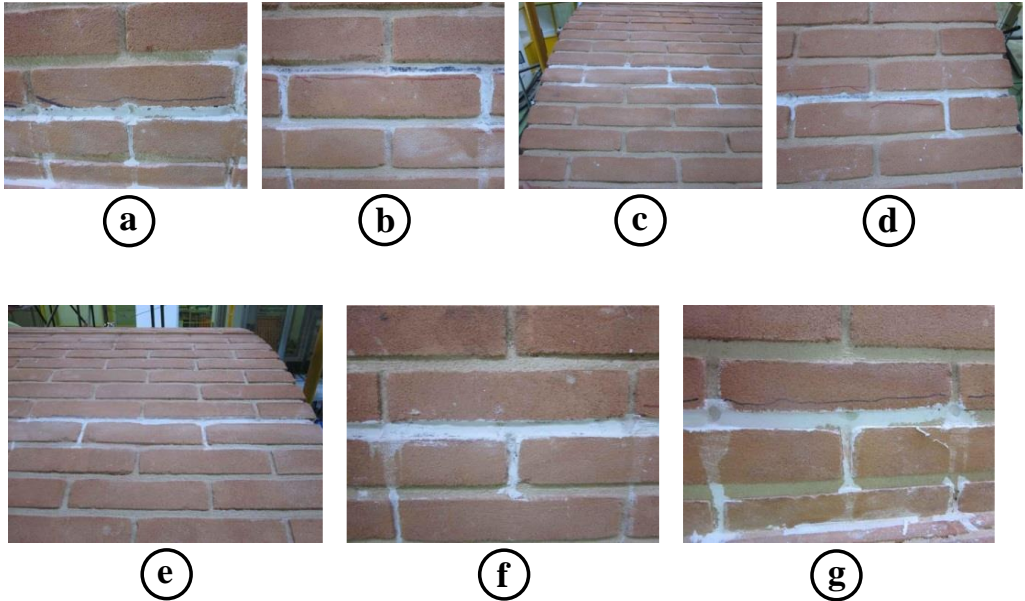
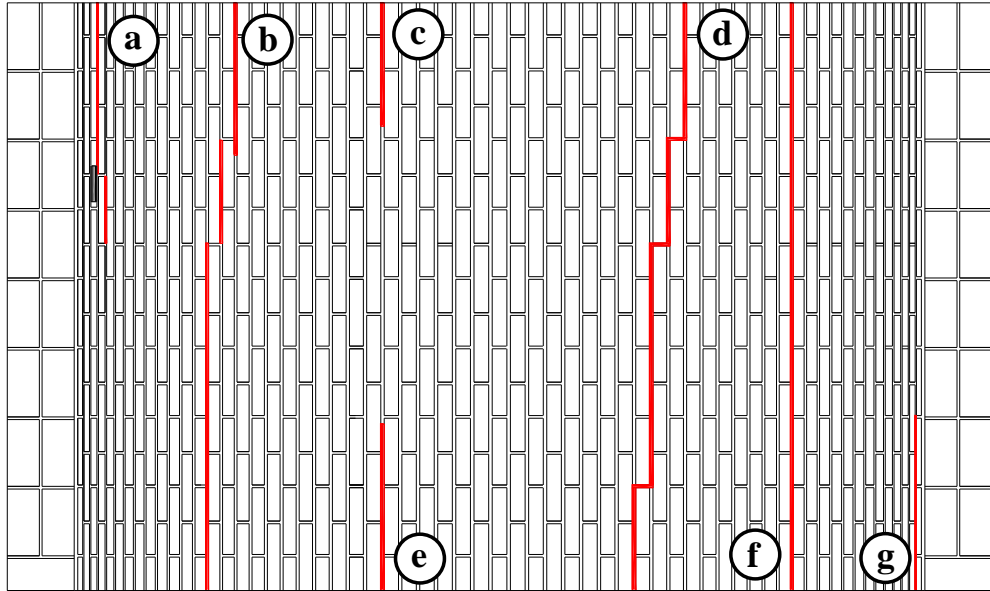


Figure 4.3 Grout injections at the extrados of the vault

The deteriorated or distressed mortar has been carefully removed from the joints, taking care to prevent damages to the nearest bricks. Once the old mortar had been removed, the whole involved surfaces have been accurately cleaned from mortar dust and debris. Then the repointing phase has been performed by pressing the repair mortar into the joints (in three successive layers).

The grout injections have been performed at the extrados of the vault (Figure 4.3). In particular, at the cracked locations, holes have been drilled at the extrados of the vault with a spacing of 12 cm. Since the cracks were not wide, a cement-free fluid hydraulic binder has been used as mixture for the injections.



Figure 4.4 IMG system at the extrados of the vault

The IMG system has been installed at the extrados of the vault (Figure 4.4). In particular, a first layer 5 mm thick of mortar has been applied to the extrados of the vault. While the mortar was still fresh, an alkali-resistant primed basalt fibre grid has been applied onto the mortar layer. Since the vault is 220 cm deep, two sheets of grid have been jointed in order to cover the entire extrados. Therefore, the installation of the grids has been performed taking care to overlap at the least by 5 cm all the joints.

Once the grid was perfectly bonded to the first mortar layer, a second layer, entirely covering the grid, has been applied. The mortar used for both the layers was a two-component premixed mortar made of: natural hydraulic lime (NHL), Eco-Pozzolan, natural sand, special additives and synthetic polymers in aqueous dispersion (i.e. MAPEI *Planitop HDM restauro*). The grid used was a basal grid (250 g/m^3) having a tensile strength $f_{tg} = 3000 \text{ MPa}$ and elastic modulus $E_g = 89 \text{ GPa}$. A photographic resume of the whole retrofit process has been provided in Figure 4.5.



Figure 4.5 Resume of the retrofit process: (a) Repointing of the cracked joints at the intrados; (b) Grout injections at the extrados; (c) Grid installing layer at the extrados.

4.2 Instrumentation

The monitoring of the retrofitted vault has been achieved with the use of seven accelerometers (six tri-axial accelerometers and one bi-axial accelerometer) and two laser-optical displacement sensors. The outputs recorded by the main instrumentation have been validated by means of two more secondary accelerometer sets. On comparison purpose all the sensors, namely: TRI-100715, TRI-103765, TRI-100050, TRI-103763, TRI-103762, TRI-102818, BI-103766, L1 and L2, have been installed in the same geometrical configuration

adopted in the previous tests (see section 3.4). A comprehensive scheme of the sensor position is provided in Figure 3.22 and Figure 3.23.

4.3 Input and test programme

The seismic behaviour of the retrofitted masonry vault has been investigated by means of one set of time-history accelerograms namely “ART_R”. The ART_R set consists of eighteen tests, each one having a total duration of 30 s. The time-history used is the same artificial accelerogram used in the previous tests (see section 3.5) having a PGA of 4.50 m/s^2 (Figure 3.24b). All the tests of the experimental programme are unidirectional with the shaking movement applied in the transversal direction of the vault (Figure 4.6).

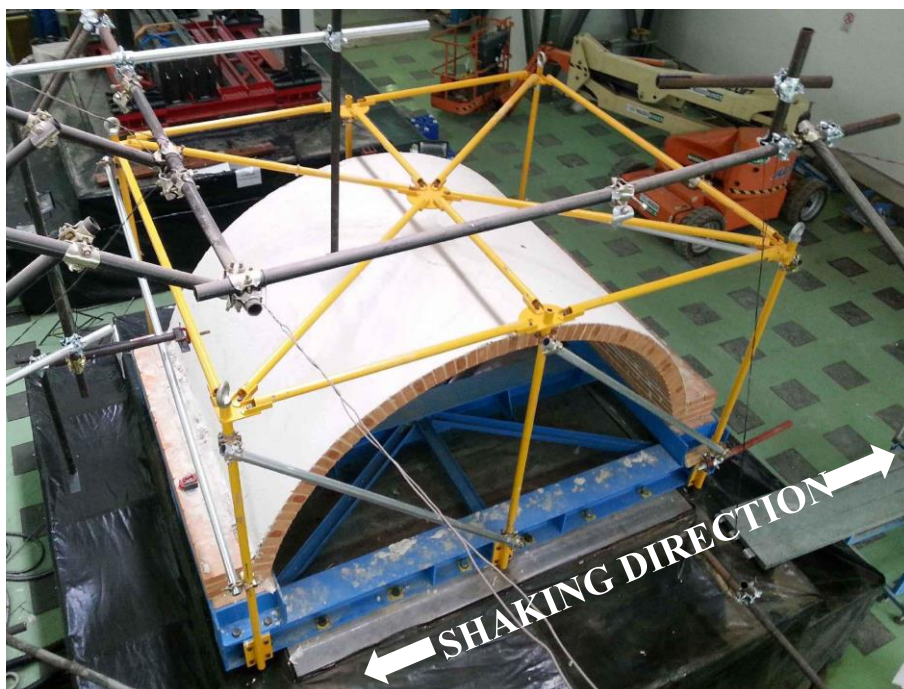


Figure 4.6 Test setup and specimen: shaking direction (retrofitted vault).

As well as in the previous tests on the unreinforced vault, the time-history has been scaled by different factors in order to get a progressive PGA increase.

In particular the scale factors adopted are: 0.10, 0.20, 0.30, 0.40, 0.50, 0.75, 1.00, 1.10, 1.20, 1.30, 1.40, 1.50, 1.60, 1.80, 2.00, 2.20, 2.50, and 2.75. Consequently, the test sequence in terms of PGA was the following: 0.45, 0.90, 1.35, 1.80, 2.25, 3.38, 4.50, 4.95, 5.40, 5.85, 6.30, 6.75, 7.20, 8.10, 9.00, 9.90, 11.25 and 12.38 m/s^2 . The ART_R set of time-history accelerograms cover frequency ranging up to 30 Hz (see the FFT in Figure 3.11d).

Preliminarily, a set of random accelerograms were performed on dynamic identification purpose (natural frequency and damping). The random set, namely “RND_R” was performed by means of five tests. In particular, an input random accelerogram scaled at different PGA levels (0.25, 0.50, 0.75, 1.00 and 1.25 m/s^2) was used as the input. The total duration of the random vibration is 60 s. It is worth remarking that, for the reasons discussed in the previous section 3.5, the procedure described in [84], concerning the optimisation of the drive motion has been taken into account in the present experimental programme as well. Although the ART_R set include more tests than the previous ART set (see section 3.5), on comparison purpose, each test of the ART set has a corresponding (same input signal) test in the ART_R set. Table 4.1 and Table 4.2 list the complete experimental test programme.

Table 4.1: Experimental test programme pt. 1 (retrofitted vault).

Test ID	Scale factor	Desired PGA [m/s^2]	Achieved PGA [m/s^2]
RND1_R	0.25	0.25	0.28
RND2_R	0.50	0.50	0.56
RND3_R	0.75	0.75	0.88
RND4_R	1.00	1.00	1.19
RND5_R	1.25	1.25	1.51

Table 4.2: Experimental test programme pt. 2 (retrofitted vault).

Test ID	Scale factor	Desired PGA [m/s²]	Achieved PGA [m/s²]
ART1_R	0.10	0.45	0.42
ART2_R	0.20	0.90	0.97
ART3_R	0.30	1.35	1.38
ART4_R	0.40	1.80	1.69
ART5_R	0.50	2.25	2.23
ART6_R	0.75	3.38	3.55
ART7_R	1.00	4.50	5.12
ART8_R	1.10	4.95	6.14
ART9_R	1.20	5.40	6.35
ART10_R	1.30	5.85	6.15
ART11_R	1.40	6.30	7.88
ART12_R	1.50	6.75	8.30
ART13_R	1.60	7.20	6.93
ART14_R	1.80	8.10	8.32
ART15_R	2.00	9.00	9.17
ART16_R	2.20	9.90	9.59
ART17_R	2.50	11.25	10.70
ART18_R	2.75	12.38	11.70

4.4 Outcomes of the shaking table tests

The main results of the experimental tests are described in the following sections. The outcomes are grouped by test set, according to the set naming defined in the previous section 4.3.

4.4.1 RND_R test results (Dynamic identification)

The natural frequency and the damping ratio have been evaluated by means of a dynamic identification procedure. Using a random time-history in acceleration as input signal, a sequence of five shakings has been performed scaling the signal from a PGA of 0.25 m/s^2 to 1.25 m/s^2 .

It's worth noting that a low intensity signal has been used in the dynamic identification phase to prevent premature damage on the specimen.

The natural frequency has been assessed according to the transfer curve method. The first shaking (RND1_R) at PGA of 0.25 m/s^2 provided a natural frequency of about 19.3 Hz. The achieved result highlights the improvement of stiffness given by the retrofit (coupled to a negligible mass increase). The further four tests (i.e. RND2_R, RND3_R, RND4_R and RND5_R) have shown a decay of the natural frequency due to premature minor damage (microcracking) of the specimen.

The decay of the natural frequency evidenced by the Transfer Function amplitude is shown in Figure 4.7.

The damping ratio, ζ , has been achieved according to the well-known half-power bandwidth method (section 3.6.1). The retrofitted vault has shown a damping ratio, ζ , ranging between 1.7% and 2.8%. The damping ratio increases with the intensity of the signal. This result is expected and it is due to the microcracking of the specimen.

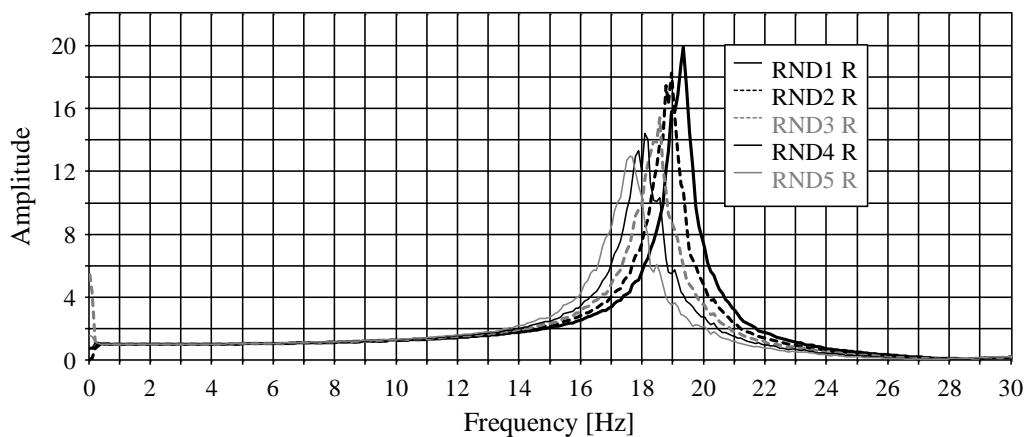


Figure 4.7 Natural frequency decay of the specimen (retrofitted vault).

Indeed, being the damping ratio closely related to the energy dissipation, the higher the microcracking is the higher the damping ratio becomes.

A resume of both the fundamental frequency and damping ratio achieved for each test is provided in Table 4.3.

Table 4.3: Natural frequencies and damping ratios (retrofitted vault).

Test ID	Natural frequency [Hz]	Damping ratio [%]
RND1_R	19.3	1.7%
RND2_R	18.9	1.7%
RND3_R	18.6	1.9%
RND4_R	18.1	2.2%
RND5_R	17.6	2.8%

4.4.2 ART_R test results (artificial earthquake)

The input used is an artificial accelerogram specifically designed for the tests. A sequence of eighteen tests was performed increasing the PGA of the table drive motion up to 12.38 m/s^2 (11.70 m/s^2 recorded). For the test performed at 100% level intensity (ART7_R), the horizontal component of the achieved time histories recorded at the impost (BI-103766) and at the keystone (TRI-100715) of the vault are shown in Figure 4.8a. The relative displacement time-history (keystone-impost) is shown in Figure 4.8b.

The complete testing sequence is reported in Table 4.1 and Table 4.2. The outcomes achieved are presented in terms of maximum accelerations and observed damage to the specimen.

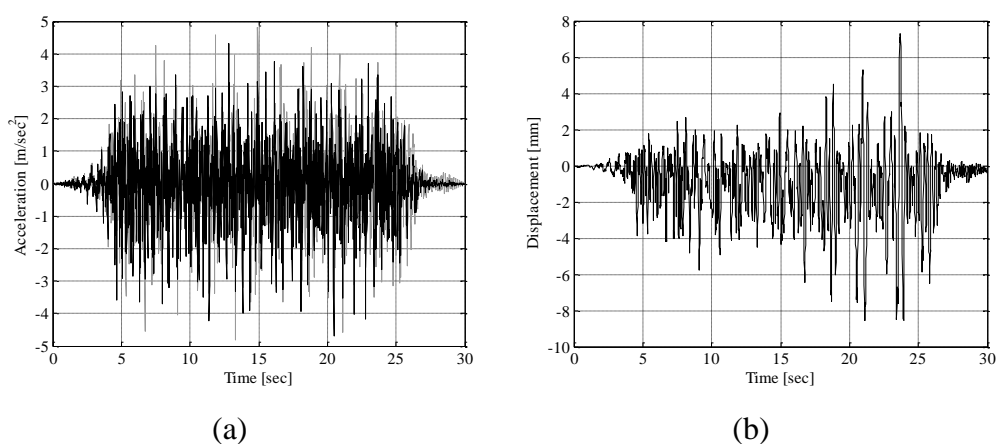


Figure 4.8 Artificial earthquake, test ART7_R: (a) recorded time-history in acceleration at the impost (in black) and keystone (in grey) of the vault; (b) relative keystone-impost displacement.

Both the horizontal and vertical accelerations have been recorded in five locations according to the instrumentation scheme represented in Figure 3.22 and Figure 3.23. As well as in the case of unreinforced vault, the maximum horizontal acceleration was recorded by the accelerometer TRI-103763 during the last test (i.e. test ART18_R).

In particular, the recorded acceleration was 21.21 m/s^2 . The magnification was of about 82% compared to the recorded PGA of the table (i.e. 11.65 m/s^2). At the keystone location (i.e. accelerometer TRI-100715) the maximum horizontal acceleration (9.12 m/s^2) was recorded during the test ART18_R. The maximum vertical acceleration (i.e. 29.90 m/s^2) was recorded by accelerometer TRI-100715 during the test ART16_R. The horizontal and vertical maximum recorded accelerations are reported in Table 4.4 and Table 4.5 respectively. Furthermore, in Figure 4.9 the results, in terms of maximum accelerations, are plotted as profiles.

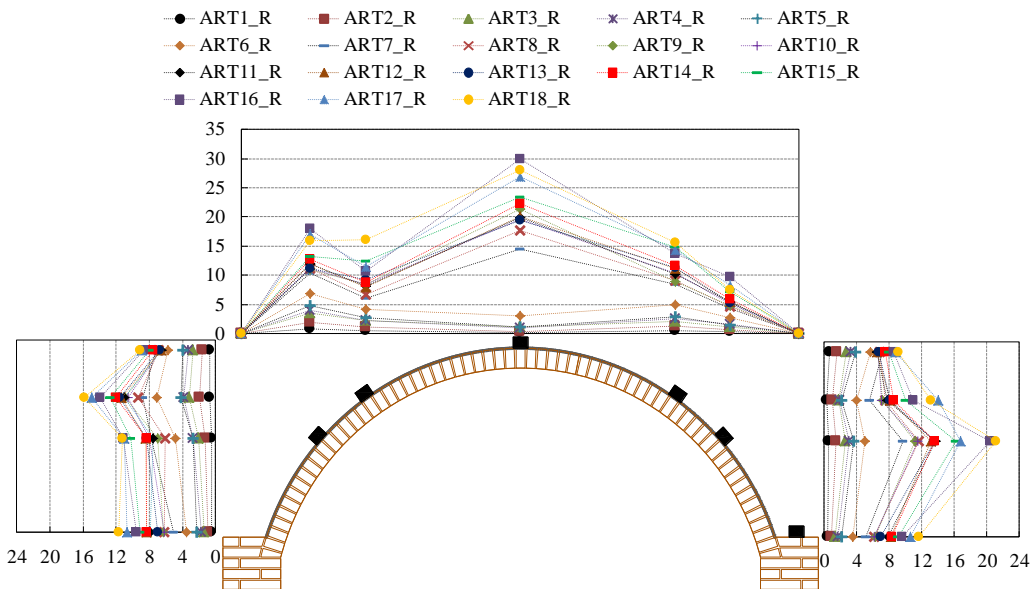


Figure 4.9 ART_R: Maximum acceleration profiles (values expressed in m/s^2).

The maximum horizontal acceleration trends remain almost the same when varying the magnitude of the base acceleration. However a large increase of the maximum horizontal accelerations is noticed after the test ART6_R which corresponds to a PGA of 5.12 m/s^2 . The vertical acceleration trends remain

almost the same until the test ART6_R (5.12 m/s^2) then a different trend is noticed. Therefore the maximum acceleration trends can be divided into two groups. The first group includes the tests until the ART6_R (5.12 m/s^2), while the second group includes all the other tests (i.e. until the test ART18_R which corresponds to a PGA of 11.70 m/s^2).

Table 4.4: ART_R test results: horizontal maximum accelerations.

TEST ID	TRI- 100715 [m/s²]	TRI- 102818 [m/s²]	TRI- 103765 [m/s²]	TRI- 103762 [m/s²]	TRI- 100050 [m/s²]	TRI- 103763 [m/s²]
ART1_R	0.65	0.65	0.75	0.50	0.36	0.63
ART2_R	1.56	1.57	1.90	1.24	1.01	1.50
ART3_R	2.72	2.74	3.21	2.04	1.84	2.63
ART4_R	3.28	3.24	3.78	2.69	1.94	3.05
ART5_R	3.92	3.90	4.23	2.71	2.18	3.67
ART6_R	5.77	5.81	7.10	4.82	4.04	5.05
ART7_R	7.20	7.11	8.79	7.81	5.56	9.73
ART8_R	6.83	6.97	9.36	6.08	7.58	11.67
ART9_R	6.62	6.88	10.95	6.99	7.22	11.20
ART10_R	6.60	6.47	10.58	8.02	7.05	11.55
ART11_R	6.55	6.42	11.07	7.52	7.82	13.73
ART12_R	6.54	6.95	11.33	8.43	8.15	13.22
ART13_R	6.75	7.10	11.60	8.33	8.17	13.58
ART14_R	7.57	7.96	12.03	8.36	8.60	13.66
ART15_R	7.96	8.08	12.69	10.23	10.08	16.30
ART16_R	8.62	8.70	13.93	11.12	11.05	20.48
ART17_R	8.86	8.85	14.94	10.99	14.03	16.83
ART18_R	9.12	9.15	15.85	11.30	13.18	21.21

Table 4.5: ART_R test results: vertical maximum accelerations.

TEST ID	TRI- 100715 [m/s²]	TRI- 102818 [m/s²]	TRI- 103765 [m/s²]	TRI- 103762 [m/s²]	TRI- 100050 [m/s²]	TRI- 103763 [m/s²]
ART1_R	0.15	0.12	0.48	0.80	0.55	0.28
ART2_R	0.39	0.38	1.15	1.97	1.29	0.70
ART3_R	1.15	1.19	2.20	3.45	2.09	1.16
ART4_R	1.00	1.07	2.27	4.04	2.56	1.52
ART5_R	1.06	1.05	2.64	4.73	2.92	1.50
ART6_R	2.97	2.93	4.14	6.84	4.87	2.72
ART7_R	14.55	14.77	6.08	10.42	8.41	4.36
ART8_R	17.72	17.84	6.74	11.13	9.01	4.58
ART9_R	21.27	20.93	8.49	10.99	9.00	4.72
ART10_R	19.59	19.78	8.44	11.12	10.38	5.11
ART11_R	19.98	19.38	8.05	11.97	10.16	5.42
ART12_R	20.04	19.54	7.95	11.92	11.08	5.41
ART13_R	19.41	19.12	9.22	11.09	11.24	5.19
ART14_R	22.32	21.13	8.82	12.79	11.62	5.89
ART15_R	23.38	23.97	12.37	13.28	14.77	7.15
ART16_R	29.90	27.22	10.75	18.06	13.74	9.74
ART17_R	26.90	26.63	11.53	17.11	14.27	8.34
ART18_R	28.02	27.55	16.04	15.94	15.64	7.54

As in the case of unreinforced vault, the acceleration profiles highlight a not symmetric behaviour. The maximum horizontal accelerations on the right side of the vault were recorded at 60° from the keystone locations (i.e. accelerometers TRI-103763).

Otherwise, on the left side of the vault the maximum horizontal accelerations were recorded at 45° from the keystone location (i.e. accelerometer TRI-103765). The horizontal dynamic amplifications, evaluated as shown in the Equation (3.13), are plotted as profiles in terms of percentage in Figure 4.10.

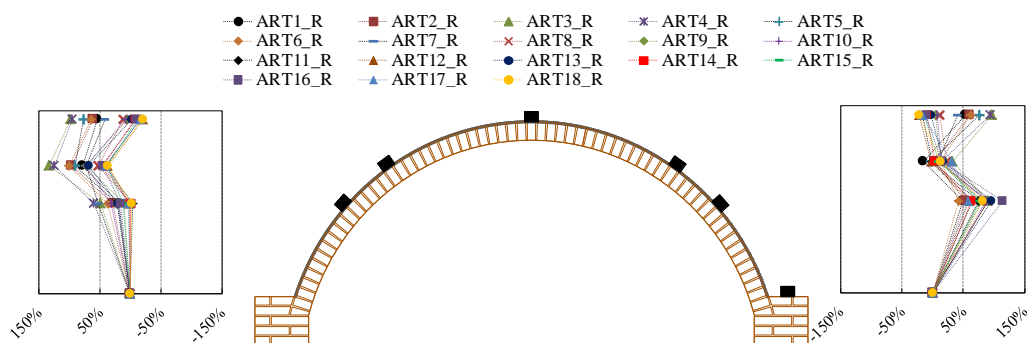


Figure 4.10 ART_R: Horizontal dynamic amplifications (values expressed in %).

In terms of dynamic amplifications it is not possible to divide the profiles into two groups. In fact, the dynamic amplification profiles highlight that the magnitude of the base acceleration does not have a strong impact on the trends of the horizontal dynamic amplifications. The horizontal dynamic amplification profiles exhibit a not symmetric trend. As expected the maximum horizontal amplifications on the right side of the vault were achieved at both the keystone and 60° from the keystone locations. On the left side of the vault the maximum horizontal accelerations were achieved at 45° from the keystone location. The horizontal dynamic amplifications achieved are reported in Table 4.6.

Table 4.6: ART_R test results: dynamic amplifications.

TEST ID	TRI- 100715 [%]	TRI- 102818 [%]	TRI- 103765 [%]	TRI- 103762 [%]	TRI- 100050 [%]	TRI- 103763 [%]
ART1_R	53.5%	53.9%	77.2%	18.2%	-14.4%	49.5%
ART2_R	60.2%	61.1%	95.6%	27.8%	3.5%	54.4%
ART3_R	97.1%	98.3%	132.8%	48.0%	32.9%	90.5%
ART4_R	94.2%	92.3%	124.3%	59.2%	14.8%	81.0%
ART5_R	75.8%	74.8%	89.8%	21.7%	-2.2%	64.7%
ART6_R	62.9%	63.9%	100.2%	36.0%	13.8%	42.5%
ART7_R	40.6%	38.8%	71.6%	52.4%	8.6%	89.9%
ART8_R	11.2%	13.5%	52.4%	-1.0%	23.3%	90.0%
ART9_R	4.2%	8.3%	72.5%	10.1%	13.7%	76.3%
ART10_R	7.3%	5.3%	72.0%	30.4%	14.6%	87.8%
ART11_R	-16.9%	-18.4%	40.5%	-4.5%	-0.7%	74.3%
ART12_R	-21.2%	-16.2%	36.5%	1.5%	-1.8%	59.3%
ART13_R	-2.7%	2.3%	67.3%	20.1%	17.8%	95.8%
ART14_R	-9.0%	-4.3%	44.6%	0.5%	3.3%	64.1%
ART15_R	-13.2%	-11.9%	38.4%	11.5%	9.9%	77.7%
ART16_R	-10.1%	-9.3%	45.3%	15.9%	15.2%	113.6%
ART17_R	-16.9%	-17.0%	40.0%	3.0%	31.6%	57.8%
ART18_R	-21.7%	-21.5%	36.1%	-3.0%	13.1%	82.1%

The maximum relative displacement measured at the keystone location (i.e. laser-optical sensor L1, see Figure 3.23) ranges between 0.44 mm and 10.70 mm from the test ART1_R to the test ART18_R.

The same increasing trend has been shown by the laser-optical sensor, L2, placed on the left side of the vault (see Figure 3.23).

In particular the maximum relative displacement measured by the L2 sensor ranges between 0.52 mm and 8.81 mm from the tests ART1_R to the test ART18_R. The maximum relative displacements are shown in detail in Table 4.7.

Table 4.7: ART_R test results: maximum relative displacements.

Test ID	L1 [mm]	L2 [mm]
ART1_R	0.44	0.52
ART2_R	0.44	0.52
ART3_R	1.53	0.87
ART4_R	2.37	1.46
ART5_R	2.73	1.39
ART6_R	3.27	2.56
ART7_R	4.16	3.75
ART8_R	4.75	4.04
ART9_R	4.98	4.66
ART10_R	4.71	4.18
ART11_R	5.96	4.09
ART12_R	4.74	4.00
ART13_R	5.30	4.14
ART14_R	6.98	5.00
ART15_R	7.15	6.25
ART16_R	9.41	6.41
ART17_R	9.30	6.53
ART18_R	10.70	8.81

In the first two tests (i.e. ART1_R and ART2_R) the displacement measured by the sensor L1 is lower than the one measured by the sensor L2. Otherwise, in all the other tests, the key section always shows a relative displacement larger than the side of the vault. In order to detect vault damages, after each test, the specimen has been inspected. After the last test (i.e. test ART18_R) slight damages were observed. In the following Figure 4.11, Figure 4.12 and Figure 4.13 a comprehensive overview on the damages observed is provided.

It is worth noting that, during the tests was evident a mechanism of *opening and closing* of the cracks. The presence of the IMG prevented the cracking at the extrados of the vault. However, evident cracking at the interface between mortar and brick at the intrados of the vault has been observed.

In particular, as shown in Figure 4.13, at the intrados, interface cracking occurred, in a few joints, along its entire depth. This outcome remarks that for such curved masonry structures the weak element is the interface. Due to excessive local compressive stress concentrations, few minor detachments of the brick edges have been observed at the intrados.

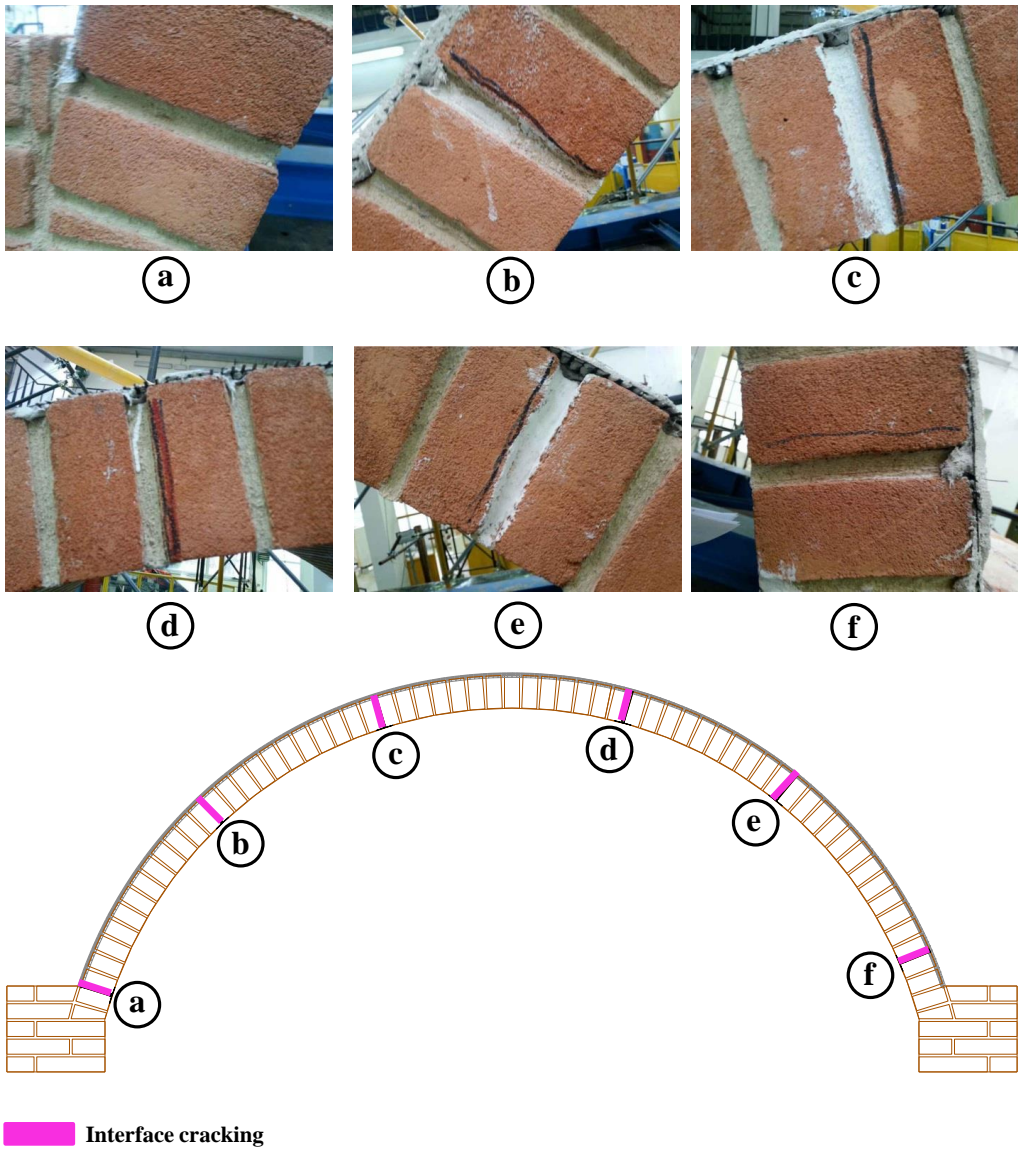


Figure 4.11 Retrofitted vault: damages detected (front view).

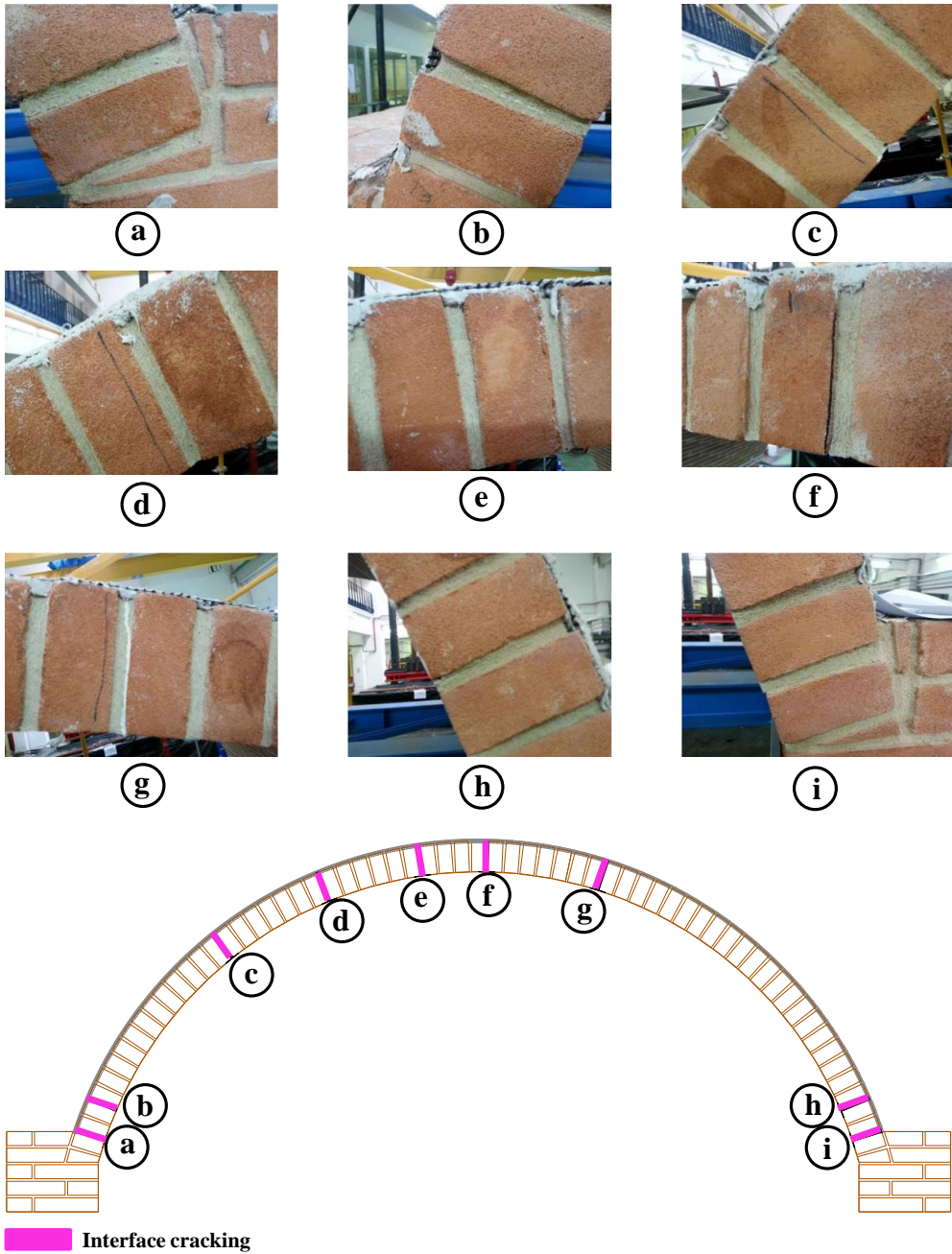


Figure 4.12 Retrofitted vault: damages detected (rear view)

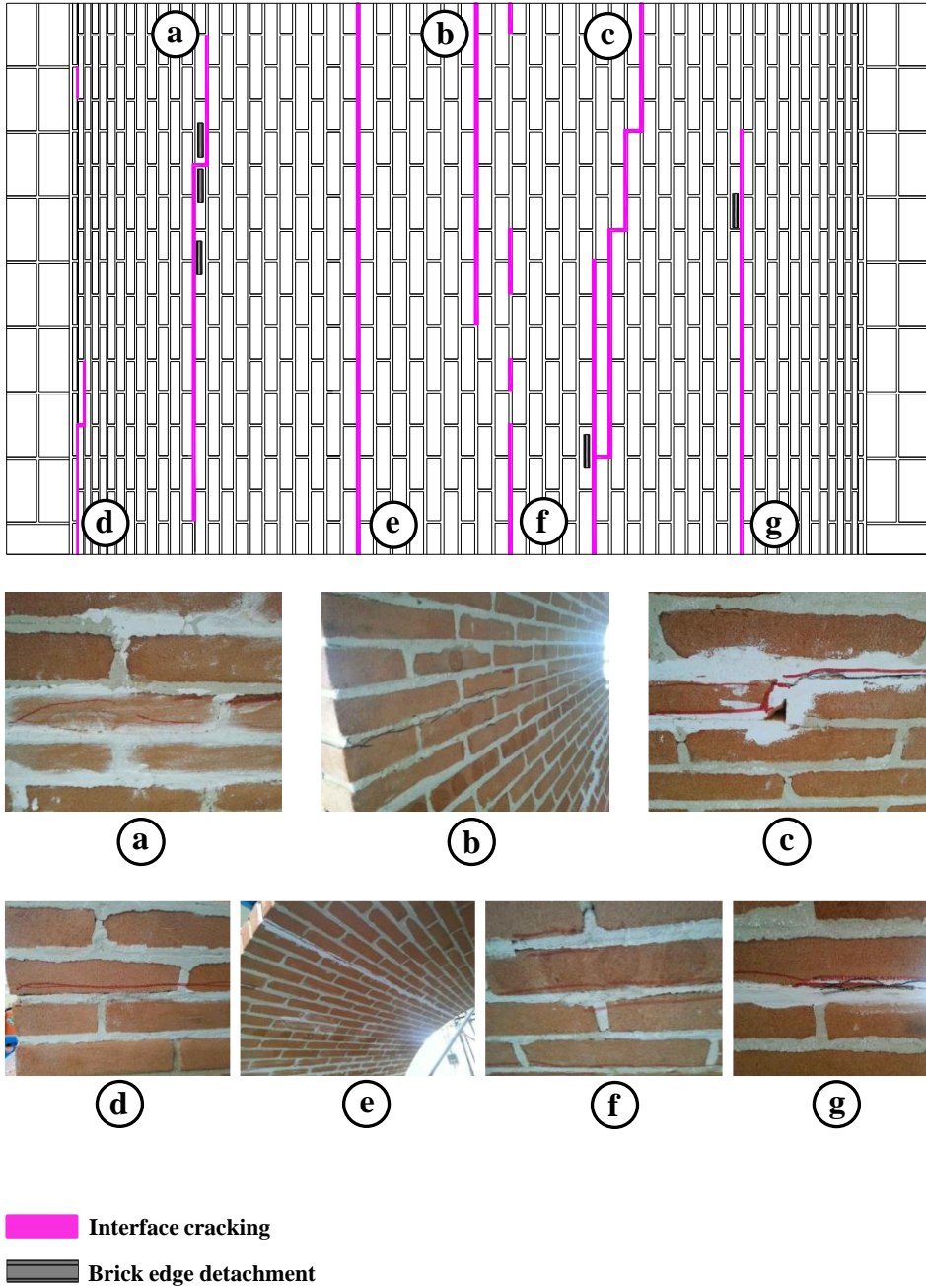


Figure 4.13 Retrofitted vault: damages detected (intrados)

4.5 Outcomes comparison: retrofitted/unreinforced vault

In the following sections the effects of the retrofit on the dynamic behaviour of the vault have been analysed. The effects of the vault retrofit have been studied by comparing the outcomes achieved in the cases of unreinforced and retrofitted vault. The outcomes have been compared in terms of: dynamic characteristics, maximum acceleration profiles and dynamic amplification profiles.

It is worth remarking that the outcomes of the tests have been compared only in the case of comparable seismic input signals. In fact, on comparison purpose, for each test of the ART set, a corresponding test (same desired input signal) was provided in the ART_R set (see sections 3.5 and 4.3).

The results show that the retrofit resulted in an evident stiffness increase and in a large improvement of the seismic capacity, while the global dynamic behaviour was not fundamentally changed. Furthermore, it is interesting noting that slight damages were detected on both unreinforced and retrofitted vault only after the respective last tests. However the respective last test input signals were not comparable. Therefore a comparison in terms of vault damage has not been reported. However comprehensive overviews about the damage detected in both the cases of unreinforced and retrofitted vault are reported in the sections 3.6 and 4.4 respectively.

4.5.1 Dynamic characteristics

The effects of the vault retrofit, in terms of dynamic characteristics, have been assessed by comparing the outcomes achieved in the dynamic identification tests (sections 3.6.1 and 4.4.1). The dynamic identification tests have been performed (in both the cases of unreinforced and retrofitted vault) using a random time-history in acceleration as input signal of the shaking table. The

main outcomes achieved by means of the dynamic identification procedure were: the natural frequencies and the damping ratios. The natural frequencies have been achieved according to the transfer curve method, while the damping ratios, ζ , have been achieved according to the well-known half-power bandwidth method. Further details about the dynamic identification tests are provided in the previous sections 3.6.1 and 4.4.1. In Figure 4.14 the comparison between the transfer functions achieved in the cases of unreinforced and retrofitted vault is shown.

The transfer function comparison shows that, due to the retrofit interventions, the natural frequency of the vault increase of about 50%. Therefore the retrofit results in a significant stiffness increase, while the mass was only slightly increased.

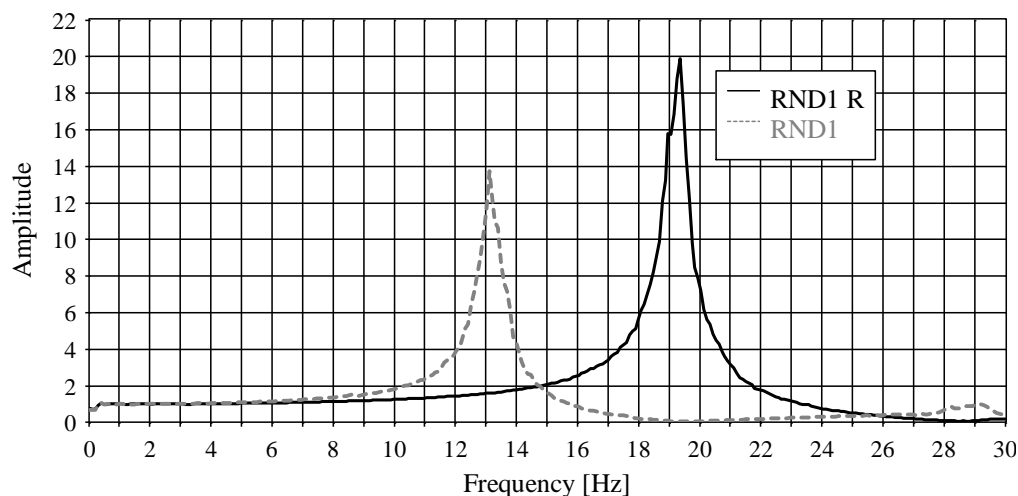


Figure 4.14 Natural frequency comparison: retrofitted vault/unreinforced vault

Moreover, as expected, in the case of unreinforced vault, the natural frequency decay is steeper than the one achieved in the case of retrofitted vault. In particular a natural frequency decay of about 10% is noticed in the case of

unreinforced vault. Conversely, in the case of retrofitted vault the natural frequency decay is of about 6%. In Figure 4.15 the natural frequency decay trends, during the dynamic identification tests, are shown in both the case of unreinforced and retrofitted vault. During the first tests (i.e. RND1 and RND1_R), due to the retrofit interventions, an increase of about 20% is noticed in the damping ratio of the vault (Figure 4.16). Being the damping ratio related to the natural frequency, this result was expected. However, since the damping ratios range between 2.2% and 3.2% (unreinforced), and between 1.7% and 2.8% (retrofitted), the rise becomes 31% after the last identification tests (i.e. RND4 and RND4_R).

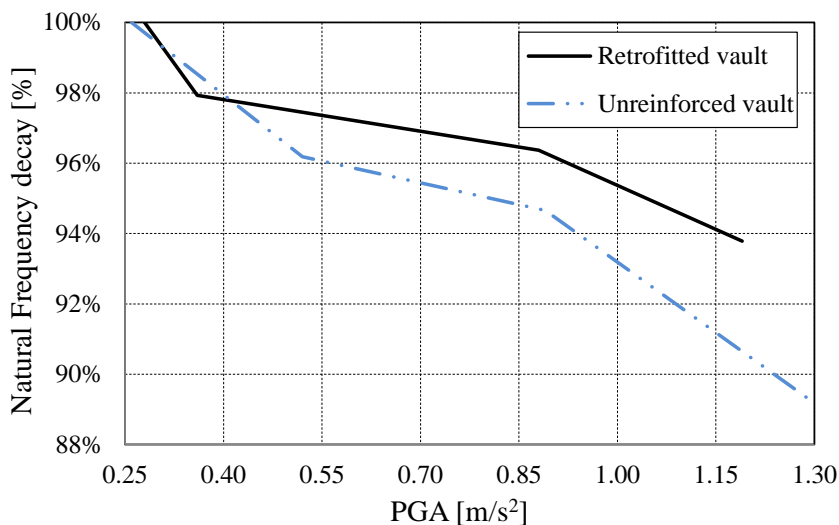


Figure 4.15 Comparison: frequency decay-achieved PGA trends

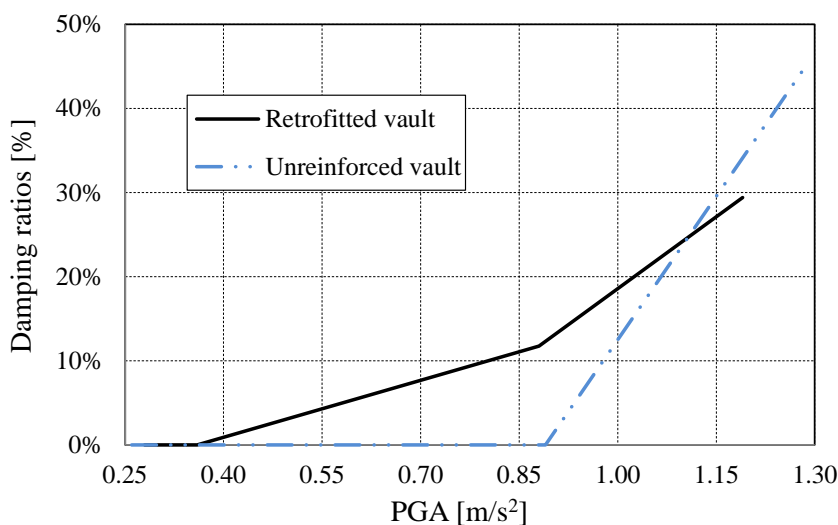


Figure 4.16 Comparison: damping ratios-achieved PGA trends

The effect of the retrofit on the dynamic characteristic can be resumed in both a significant increase of stiffness and a decrease of damping ratio. Further considerations can concern both the stiffness reduction trends and the damping ratio increase trends, when varying the PGA of the dynamic identification tests. In particular, the comparisons show that both the reduction in stiffness and the increase in damping ratios are steeper in case of unreinforced vault. These results can be explained by an improvement in terms of capacity due to the retrofit interventions.

4.5.2 Maximum acceleration profiles

The effects of the vault retrofit, in terms of maximum accelerations, have been assessed by comparing the outcomes achieved in the test on the unreinforced and the retrofitted vault (ART and ART_R test sets respectively).

The comparison has been presented by means of the most representative tests. In particular, the tests ART2, ART5, ART6 and ART7 were compared to the tests ART2_R, ART5_R, ART6_R and ART7_R.

The tests ART2 and ART2_R were selected as representative of the low intensity signals. Although the desired input signal was the same for both the tests, it does not exactly match with the achieved signal. Therefore, in order to check the full comparability of the tests, the achieved input signals have been studied by means of the Fast Fourier Transforms (FFT). The analysis of the FFT proved the achieved input signals to be fully comparable. The FFT of both the ART2 and ART2_R achieved input signals are shown in Figure 4.17.

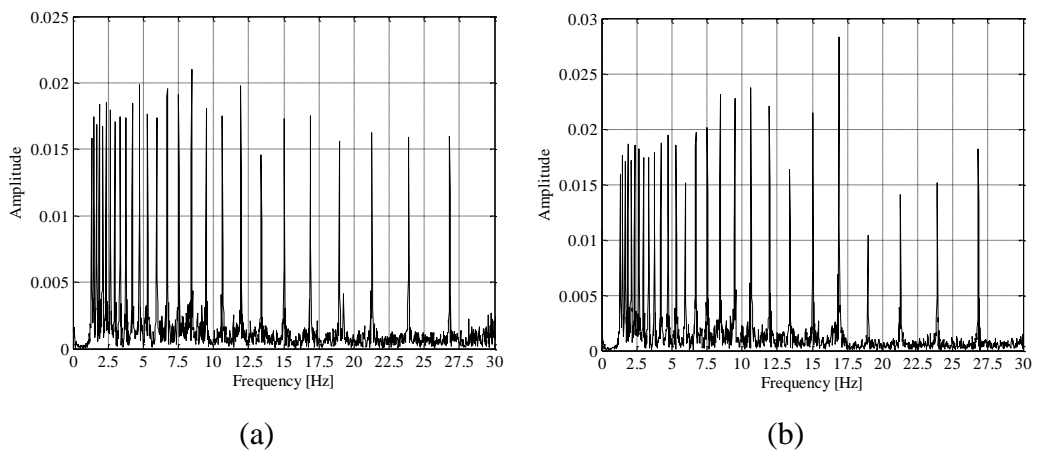


Figure 4.17 Achieved input signals FFT: (a) ART2; (b) ART2_R

The comparison between the outcomes of the tests ART2 (unreinforced vault) and ART2_R (retrofitted vault) is shown in Figure 4.18 in terms of horizontal and vertical maximum acceleration profiles.

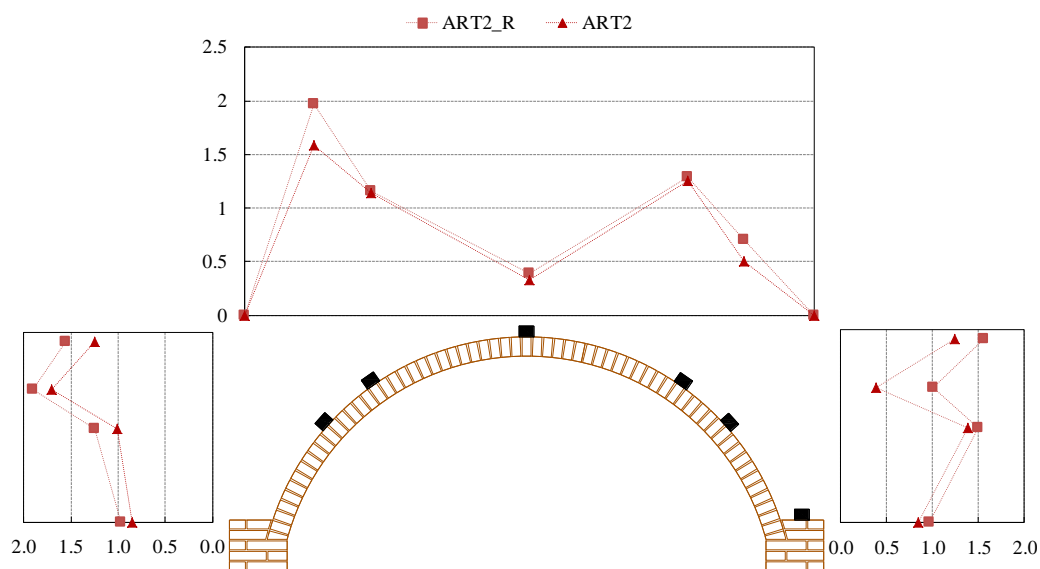


Figure 4.18 Maximum acceleration profiles comparison: ART2-ART2_R
(values expressed in m/s^2)

Both the tests ART2 (unreinforced vault) and ART2_R (retrofitted vault) exhibit almost the same maximum acceleration trends (both horizontal and vertical). The maximum horizontal acceleration values are higher in the test ART2_R than in the test ART2. The maximum vertical accelerations are almost the same in both the tests (slightly higher in the test ART2_R though). However, the accelerometers TRI-103765 and TRI-103763 recorded maximum vertical accelerations clearly higher in the test ART2_R.

The same conclusions were drawn by analysing the comparisons performed on the tests ART5, ART5_R, ART6, ART6_R, ART7 and ART7_R. Plots of the comparisons are available in Appendix A.

4.5.3 Dynamic amplification profiles

The effects of the vault retrofit, in terms of dynamic amplifications, have been assessed by comparing the outcomes achieved in the test on the unreinforced

and the retrofitted vault (ART and ART_R test sets respectively). As well as in the case of maximum accelerations, the comparison has been presented by means of the most representative tests (i.e. ART2, ART5, ART6, ART7, ART2_R, ART5_R, ART6_R and ART7_R.). Each couple of test analysed (unreinforced/retrofitted) has the same input signal. However the achieved input signals have been studied by means of the FFT (see section 4.5.2). Therefore the full comparability of the tests is granted. The comparison between the outcomes of the tests ART2 (unreinforced vault) and ART2_R (retrofitted vault) is shown in Figure 4.19 in terms of dynamic amplification profiles.

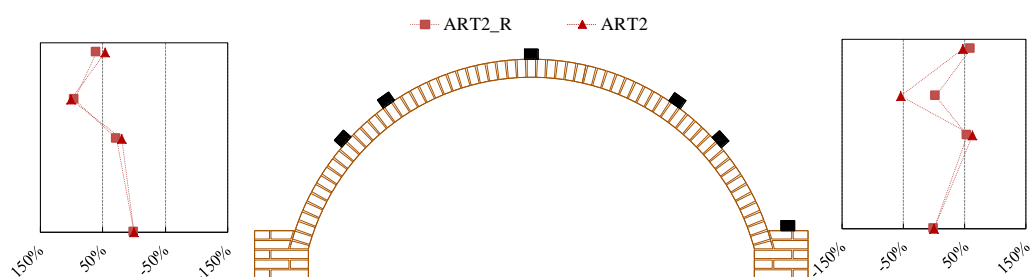


Figure 4.19 Dynamic amplification profiles comparison: ART2-ART2_R
(values expressed in %).

Both the tests ART2 (unreinforced vault) and ART2_R (retrofitted vault) exhibit almost the same dynamic amplification trends. The dynamic amplification values are almost the same in both the tests (slightly higher in the test ART2_R though). However at the TRI-100050 location (see Figure 3.23) the dynamic amplifications in the test ART2_R are about 50% higher than in the test ART2.

The same conclusions were drawn by analysing the comparisons performed on the tests ART5, ART5_R, ART6, ART6_R, ART7 and ART7_R. Plots of the comparisons are available in Appendix B.

4.6 Conclusions

The dynamic behaviour of the masonry vault has been investigated by means of shaking table tests. In particular, a set of artificial time-history accelerograms have been used as input signal. Preliminarily, a set of random accelerograms were performed on dynamic identification purpose. The results of the shaking tests have been presented in terms of dynamic characteristics (natural frequency and damping ratio), maximum accelerations, maximum displacements and observed damage to the specimen. Furthermore, a comparison with the results achieved in the case of unreinforced vault has been provided.

In the case of retrofitted vault, a natural frequency of 19.3 Hz and a damping ratio ranging between 1.7% and 2.8% have been evaluated. Therefore the effect of the retrofit resulted in both a significant increase of stiffness and a decrease of damping ratio. Furthermore, both the stiffness reduction and the damping ratio increase trends, when varying the PGA, are steeper in case of unreinforced vault. This result remarks an improvement in terms of capacity due to the retrofit interventions.

As well as in the case of unreinforced vault, the outcomes, in terms of accelerations measured on the structure, highlighted a dynamic amplification of the base horizontal excitation. Moreover, although the shaking is applied only in the horizontal direction, vertical accelerations have been detected too. Due to the higher stiffness, the maximum accelerations recorded on the retrofitted vault were higher than those recorded on the unreinforced vault. However, both the maximum acceleration trends and the dynamic amplification trends remained almost the same after the retrofit interventions.

The retrofitted vault exhibits a good seismic behaviour, showing very slight damage only after the last test performed with an achieved PGA of 11.70 m/s².

In particular, cracking at the interface between mortar and brick has been observed only at the intrados of the vault.

These findings suggest that the retrofit improves the stiffness and the seismic capacity of the vault. However the global dynamic behaviour of the vault does not change when the vault is retrofitted.

Chapter 5

Numerical modelling

The numerical analyses presented in this chapter aims to provide a reliable FE model able to simulate both the static and dynamic behaviour of the tested masonry vault (before and after the retrofit). Several modelling approaches can be used to perform a FE analysis on a masonry curved element. The most commonly used approaches are: one dimensional approach, equivalent material approach, and micro-modelling approach. In the first approach, the curved element is modelled by means of one-dimensional elements (i.e. beam elements). In the second approach also known as *macro element approach* the curved element is modelled as a homogeneous material (the equivalent mechanical properties are achieved by means of homogenization techniques). In the third approach, bricks and mortar are modelled separately allowing the use of different mechanical parameters and different constitutive laws for both the bricks and the mortar. This approach, which is the more refined, can be improved by adding further details in the modelling phase.

In particular, in order to simulate the interaction between mortar and bricks (allowing for local failures), interface elements between mortar and bricks can be used. This improvement is mostly suitable in the case of *low bond masonry* structures such as the tested masonry vault. Indeed in these structures the bond at the brick/mortar interface is low and has a dominant effect on the mechanical behaviour (i.e. crack formation and collapse mechanisms).

5.1 FE Models

In order to simulate the dynamic behaviour of the tested unreinforced masonry vault, FE analyses were performed. In, particular, the analyses were performed in 2D by means of the software DIANA developed by TNO DIANA bv [80]. Two different FE models have been used for modelling the unreinforced and the retrofitted vaults. However the two models share the modelling of the vault which is the same in both the models (Figure 5.1).

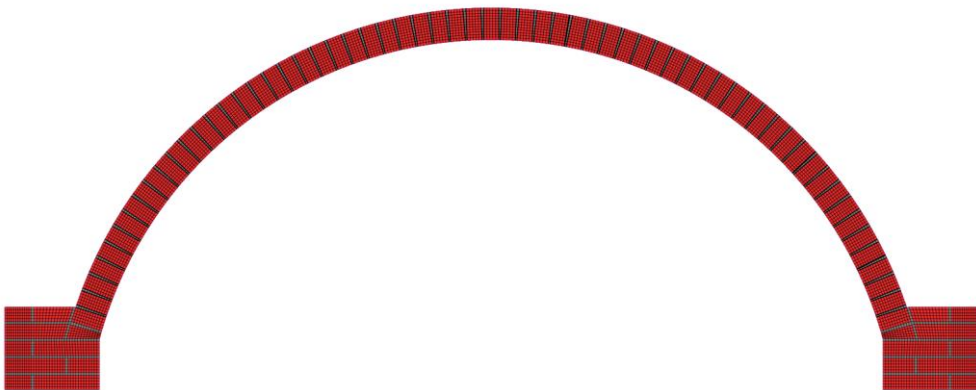


Figure 5.1 Masonry vault FE model.

According to the accurate micro-modelling approach [86], the geometry of the vault was reproduced modelling mortar and bricks individually with interface

elements in between them. As shown in Figure 5.2, a regular discretization [87], based on the CQ16M eight-node quadrilateral isoparametric plane stress elements, was used for both the mortar and the bricks.

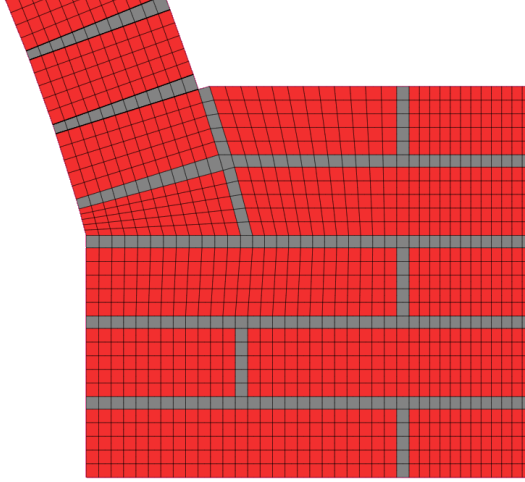


Figure 5.2 Masonry vault FE model: detail of the adopted mesh.

In particular, these elements are based on interpolation and Gauss integration. The polynomial for the displacements u_x and u_y can be expressed as:

$$u_i(\xi, \eta) = a_0 + a_1\xi + a_2\eta + a_3\xi\eta + a_4\xi^2 + a_5\eta^2 + a_6\xi^2\eta + a_7\xi\eta^2 \quad (5.1)$$

where, ξ - η is the local reference system (Figure 5.3). This polynomial typically yields to a strain ε_{xx} which varies quadratically in y direction and linearly in x direction. Similarly, the strain ε_{yy} varies quadratically in x direction and linearly in y direction. Otherwise, the shear strain, γ_{xy} , varies quadratically in both directions [80].

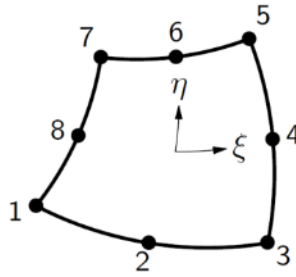


Figure 5.3 CQ16M element [80]

As discussed in the previous sections 3.6.2, 3.6.3 and 4.4.2 structural damages were not detected in both bricks and mortar (except for few minor detachments of the brick edges due to excessive local compressive stress concentrations). In particular, only cracks at the interface were detected. Therefore both brick and mortar were modelled as linear isotropic elastic materials. The mechanical properties assigned to mortar and bricks are those assessed by means of the material characterization tests described in the section 3.1.1.

The interaction between bricks and mortar joints has been modelled by means of 3+3 nodes CL12I interface elements. These elements are based on quadratic interpolation and a 4-point Newton-Cotes integration scheme. In particular, interfaces relate the forces acting on them to the relative displacement of the two sides as shown in Figure 5.4.

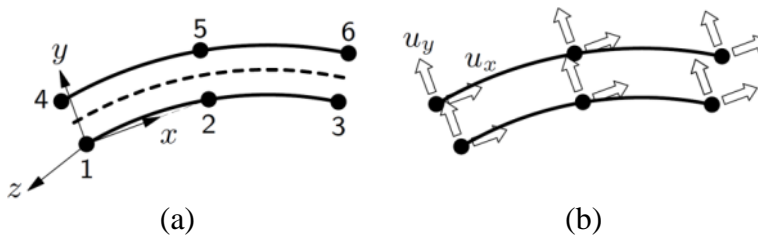


Figure 5.4 CL12I element: (a) topology; (b) displacement [80]

Since the linear isotropic elastic model has been assumed, for both mortar and bricks, the unreinforced vault nonlinearities are governed by the interface between mortar and bricks. In particular a frictional behaviour has been assumed for the interfaces. This behaviour is modelled with the nonlinear elastic friction model, which is a simplification of the Mohr-Coulomb plasticity model for continuum elements (see Figure 5.5).

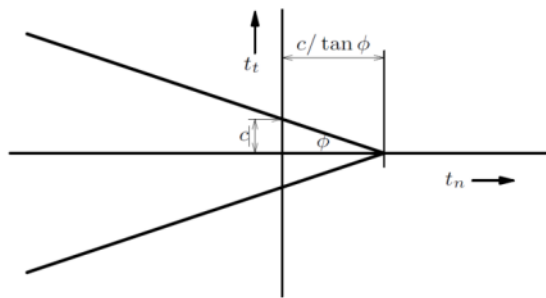


Figure 5.5 Nonlinear elastic friction model [80]

In particular, the interface model is derived in terms of the generalized strain and stress vector:

$$\begin{aligned} t &= \{t_n, t_s, t_t\}^T \\ u &= \{u_n, u_s, u_t\}^T \end{aligned} \quad (5.2)$$

Where u_s and u_t are the relative shearing displacements in the interface plane, the shear tractions t_s and t_t act in the local plane of the interface, and u_n and t_n the relative and traction displacement respectively normal to the plane. The behaviour in loading and unloading is similar. In the elastic field the constitutive behaviour is described by $t = D^e u$; where, $D^e = \text{diag} [k_n k_s k_t]$.

The basic concept of this friction model is that the effective shear stress $\tau = \sqrt{(t_s^2 + t_t^2)}$ is governed by a yield function according to:

$$f = |\tau| + t_n \tan \varphi - c = 0 \quad (5.3)$$

where $\tan \varphi$ is the friction coefficient and c is the cohesion. Thus, shear-slipping occurs when the yield function, f , becomes positive.

The linear properties assigned to the interface elements are the normal stiffness, k_n , and the shear stiffness, k_s , while nonlinear properties assigned to the interface elements are the friction coefficient, φ , and the cohesion c . The friction coefficient φ , has been achieved as: $\sin \varphi = (f_c - f_t) / (f_c + f_t)$, where, f_c is the compressive strength of the weaker material in compression; while f_t is the tensile strength of the weaker material in tension. Otherwise the cohesion and both the normal and the shear stiffness have been calibrated by means of experimental outcomes (see sections 5.2.1 and 5.2.2). The mechanical properties assigned to the interface elements are reported in Table 5.1.

Table 5.1: Interface elements properties

k_n [MPa]	k_s [MPa]	φ [rad]	c [MPa]
46	46	0.66	0.15

The FE model boundary conditions reproduced the real conditions of the laboratory test setup. In particular, both the impost sections of the vault have been fixed.

5.1.1 Modelling of the retrofit interventions

The retrofit interventions discussed in the previous section 4.1 allowed improving the overall seismic performance of the vault without changing its global dynamic behaviour. The estimation of each single retrofit contribution, to the seismic enhancement, is not possible. However, it is acceptable to assume that: both, the joint repointing and the grout injections, contributed restoring the undamaged state of the vault.

Therefore, the effect of these two retrofit interventions has been simulated by using the undamaged vault FE model. Thus only the contribution of IMG has been actually modelled in the FE model of the retrofitted vault.

Consistently with the vault modelling, micro modelling approach has been adopted for the IMG modelling as well. In particular, since the IMG is a composite material (i.e. inorganic matrix and basalt grid), matrix and grid have been modelled individually. Perfect bond has been assumed between matrix and grid, therefore interface elements were not adopted. A regular and dense discretization, based on the truss elements, was used for both inorganic matrix and basalt grid. Equivalent thickness t_{eq} has been adopted for the grid modelling. In particular for the bidirectional grid (mesh size equal to 6 mm×6 mm, weight equal to 250 g/m² and unit weight equal to 2.75 g/cm³) an equivalent thickness, $t_{eq} = 0.045$ mm has been assumed. Conversely the inorganic matrix has been modelled by using its own actual thickness. Therefore for the inorganic matrix $t_{eq} = t = 15$ mm.

In the truss elements the dimension, d , perpendicular to the bar axis, has to be small compared to the bar's length l , and the deformation can only be the axial elongation Δl (see Figure 5.6). Furthermore in the truss elements there is neither bending nor shear deformation.

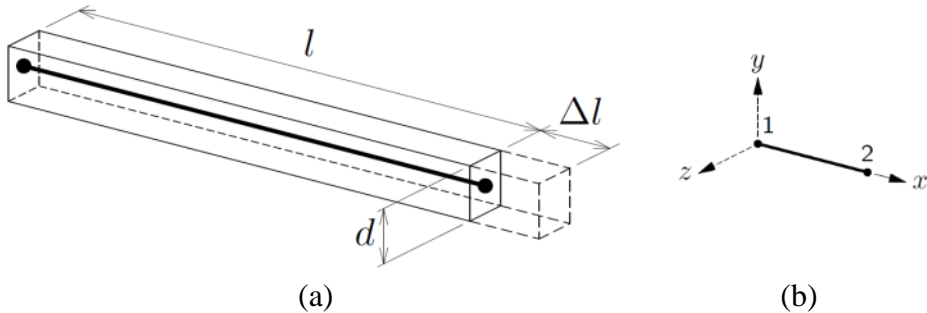


Figure 5.6 Truss element: (a) characteristics; (b) axes [80]

The elastic behaviour of both inorganic matrix and basalt grid was defined by means a linear isotropic elastic model.

The post elastic behaviour was modelled according to the total strain model coupled with the fixed crack stress-strain relationship approach. In particular, in the fixed crack approach, the stress-strain relationships are evaluated in a fixed coordinate system which is fixed upon cracking, as reported in [80].

Furthermore, the combined Rankine/Von Mises yield criterion was adopted (i.e. Rankine yield criterion in tension and Von Mises yield criterion in compression). For both, inorganic matrix and basalt grid, the same constitutive models were assumed in tension. In particular, a brittle failure was adopted. Ideal plasticity was assumed in compression for the inorganic matrix, while no compressive strength was assigned to the basalt grid (see Figure 5.7).

The equivalent thicknesses, t , the elastic modulus, E , the Poisson ratio, ν , the compressive strength, f_c and the tensile strength, f_t , assigned in the FE model to the IMG components are reported in Table 5.4.

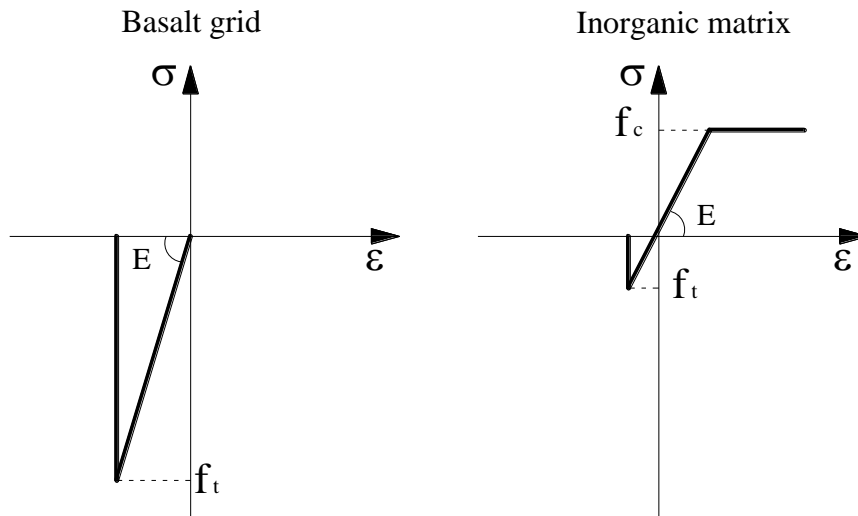


Figure 5.7 IMG constitutive models adopted: (a) grid; (b) matrix

Table 5.2: IMG mechanical properties

Component ts	E [GPa]	ν [-]	f_c [MPa]	f_t [MPa]	t_{eq} [mm]
Matrix	8	0.15	15	2.4	15
Grid	89	0.15	-	3000	0.045

5.2 Calibration of the model

The calibration of the interface modelling parameters has been carried out by means of the experimental test outcomes. In particular, the interface linear parameters (i.e. normal and shear stiffness) have been calibrated by best fitting the numerical and the experimental outcomes of the RND tests (section 3.6.1). Although the RND tests were performed on the undamaged specimen, the same calibrated parameters have been adopted in both the FE models (i.e. unreinforced and retrofitted vault models). In fact, since after the last test on unreinforced vault (i.e. test ART7) only a slight damage was detected (and repaired), it is acceptable to assume that such parameters remained unchanged. Otherwise, the nonlinear parameter (i.e. cohesion) has been calibrated by means of a vertical load test (section 5.2.2). Such test has been performed on the damaged vault after the last shaking table test (i.e. test ART18_R). It is worth noting that, during the vertical load test, the plastic hinges formation involved locations different compared to those involved during the shaking table tests. Therefore, it is acceptable to assume the same calibrated parameter (i.e. the cohesion) in both the FE models (i.e. unreinforced and retrofitted vault models). In the following sections a brief description of the adopted calibration methods is reported.

5.2.1 Calibration of the interface stiffness

The interface normal and shear stiffness have been calibrated by comparing the numerical and the experimental outcomes of the RND tests (section 3.6.1). The comparison has been performed in terms of natural frequency. Preliminary modal analyses, on the unreinforced vault FE model, have been performed varying both the normal and the shear stiffness. The analyses highlighted that,

for the studied structure, the shear stiffness does not have a strong influence on the natural frequency. Therefore, according to [88], the interface normal stiffness, k_n , has been assumed equal to the interface shear stiffness, k_s . Then, assumed $k_n = k_s = k$, parametric modal analyses have been performed when varying the interface stiffness k . In particular, stiffness values ranging between 35 MPa/mm and 50 MPa/mm have been assumed.

The parametric analyses show an almost linear relationship between the interface stiffness, k , and the natural frequency (Figure 5.8). In particular, the match between the experimental natural frequency (13.1 Hz) and the numerical natural frequency has been achieved for $k = 46$ MPa/mm.

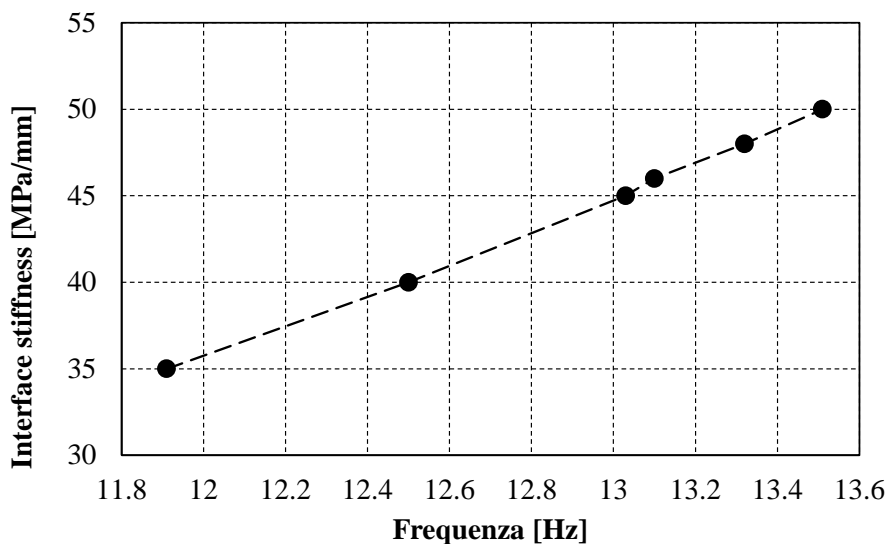


Figure 5.8 Calibration of the interface stiffness: interface stiffness-natural frequency curve

Further analyses confirmed the validity of the interface stiffness achieved. In particular, keeping the assumption of $k = 46$ MPa/mm, modal analyses were performed on the retrofitted vault FE model.

As well as in the case of unreinforced vault FE model, the natural frequency achieved numerically (18.55 Hz) showed a good match with the experimental natural frequency (19.3 Hz).

5.2.2 Calibration of the interface cohesion

The interface cohesion has been calibrated by means of a vertical load test performed at the Laboratory of the Department of Structures for Engineering and Architecture (University of Naples “Federico II”).

The test has been performed after the last shaking table test (i.e. test ART18_R). The damaged vault has been tested on the same testing structure used for the previous shaking table tests (see section 3.3). The monitoring of the vault has been achieved by means of a linear variable displacement transducer (LVDT). In particular the LVDT namely LVDT A has been placed at the keystone location.

The vault was subjected to a vertical distributed load applied at the keystone location. In particular the load was applied on a length of 40 cm along the whole depth of the vault. A comprehensive scheme of both the LVDT and the load position is provided in Figure 5.9.

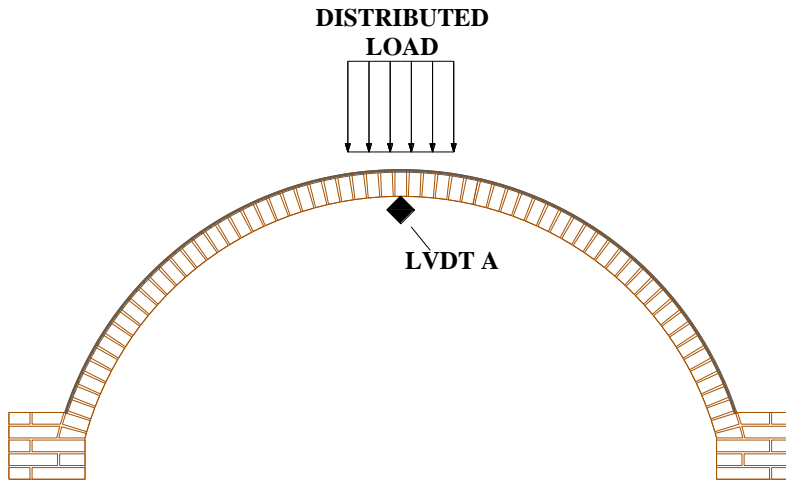


Figure 5.9 Vertical load test: instrumentation and load layout

The load was quasi-statically applied to the vault at increasing steps by means of 0.25 kN sacks. In particular, at each step, the vault was loaded by one more sack. Some pictures of the vertical load test are provided in Figure 5.10.



Figure 5.10 Vertical load test: (a) loading phase; (b) maximum load

The experimental load-displacement curves are provided in Figure 5.11. In order to take into account of the deformability of the testing system, which has

been experimentally evaluated, the curve has been re-aligned. As shown in Figure 5.11, for a load of 9.8 kN (i.e. 40 steps) the load-displacement curve level off, highlighting a hinge formation.

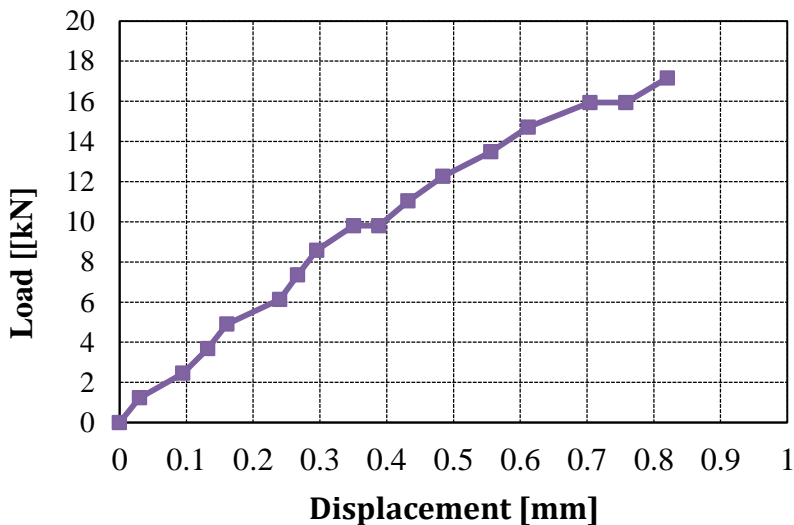


Figure 5.11 Vertical load test: experimental load-displacement curves

Then, the curve grows again until a load of about 16 kN (i.e. 65 steps) where the curve level off again. The test has been stopped after 70 steps resulting in a maximum vertical load of about 16.7 kN. After the test evident cracks at the interface between mortar and brick were detected.

Parametric numerical analyses when varying the interface cohesion, c have been performed on the retrofitted vault FE model. In particular, the experimental vertical load test has been simulated in order to compare the load-displacement curve and therefore calibrate the interface cohesion. Load-displacement curves have been provided when varying the interface cohesion (see Figure 5.12). In particular two interface cohesion values (i.e. 0.05, and 0.15 MPa) have been considered.

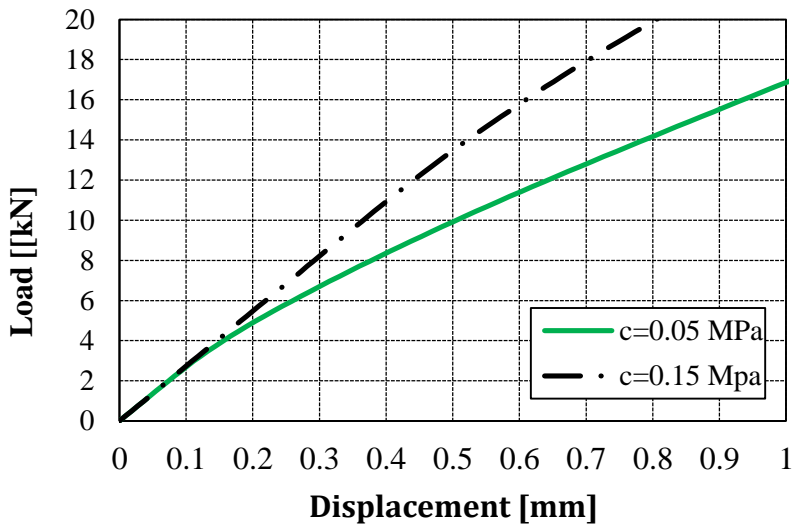


Figure 5.12 Calibration of the interface cohesion: numerical load-displacement curves

In Figure 5.13 a comparison between numerical and experimental outcomes is provided. The comparison shows that in the first elastic branch (i.e. until 2.45 kN) both the curves catch the experimental behaviour. However in the post-elastic the curve $c = 0.15$ catches better the experimental behaviour.

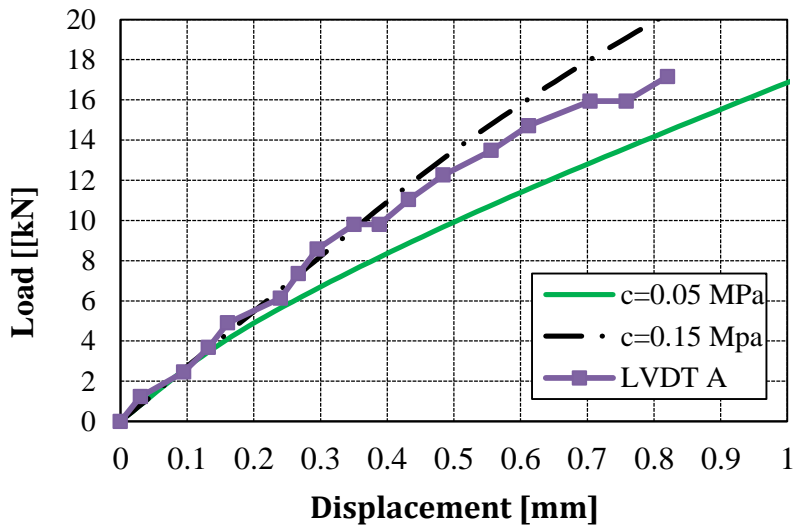


Figure 5.13 Calibration of the interface cohesion: numerical-experimental comparison

5.3 Dynamic linear analyses

The dynamic properties of both the unreinforced and the retrofitted vault, under vibrational excitation, have been investigated by means of dynamic linear analyses. The dynamic linear analyses have been performed on the FE models presented in the section 5.1 and calibrated in the section 5.2. In the following sections a brief review of the main outcomes of the dynamic linear analyses is provided. The outcomes are shown in terms of modal shapes and dynamic properties.

5.3.1 Unreinforced vault

The calibrated unreinforced vault FE model has been used to investigate properties of the unreinforced vault under vibrational excitation.

In particular: frequencies, angular frequencies, ω , periods, T , and both participant mass in horizontal direction, M_h and in vertical direction, M_v , have been achieved for the first ten vibration modes of the unreinforced vault. The modal shapes and their correspondent periods, T , are reported in Figure 5.14 and Figure 5.15.

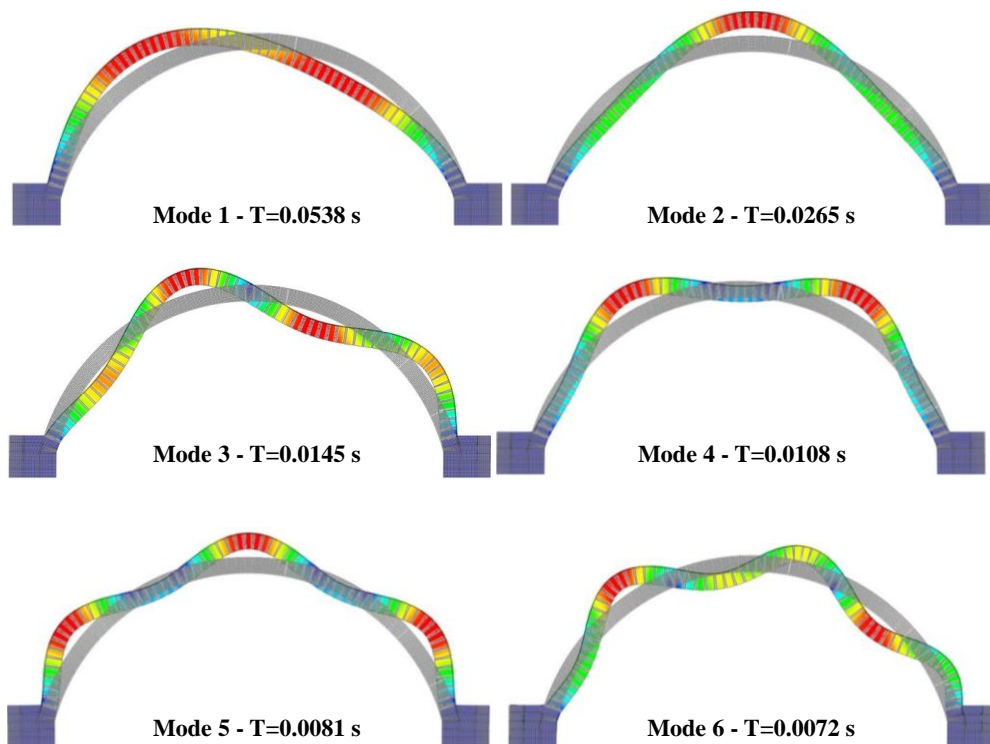


Figure 5.14 Unreinforced vault: modal shapes (mode 1-6)

The first mode is predominant and it involves the highest participating mass in horizontal direction (i.e. about 40 %). However, modes higher than the first involve the most of the participating mass in horizontal direction.

Therefore, the contribution of such modes to the motion of the vault is not negligible. The largest portion of mass, in vertical direction, is participating at the fourth and the fifth modes.

Both, the fourth and fifth mode, involve almost the same participating mass in vertical direction (i.e about 24% and 20% respectively).

Table 5.3 lists the main outcomes of the modal analysis on the unreinforced vault.

Table 5.3: Unreinforced vault: modal properties

Mode	Frequency	ω	Period	M_h	SumM_h	M_v	SumM_v
[-]	[Hz]	[rad/s]	[s]	[-]	[%]	[-]	[%]
1	13.1	82.31	0.0763	0.402	40.21	0.000	0.00%
2	26.7	167.76	0.0375	0.000	40.21	0.063	6.28%
3	49.0	307.88	0.0204	0.114	51.58	0.000	6.28%
4	66.7	419.09	0.0150	0.000	51.58	0.241	30.38%
5	86.0	540.35	0.0116	0.000	51.58	0.208	51.15%
6	101.7	639.00	0.0098	0.085	60.05	0.000	51.15%
7	127.7	802.36	0.0078	0.030	63.05	0.000	51.15%
8	141.4	888.44	0.0071	0.000	63.05	0.003	51.45%
9	180.5	1134.11	0.0055	0.014	64.49	0.000	51.45%
10	211.0	1325.75	0.0047	0.000	64.49	0.072	58.63%

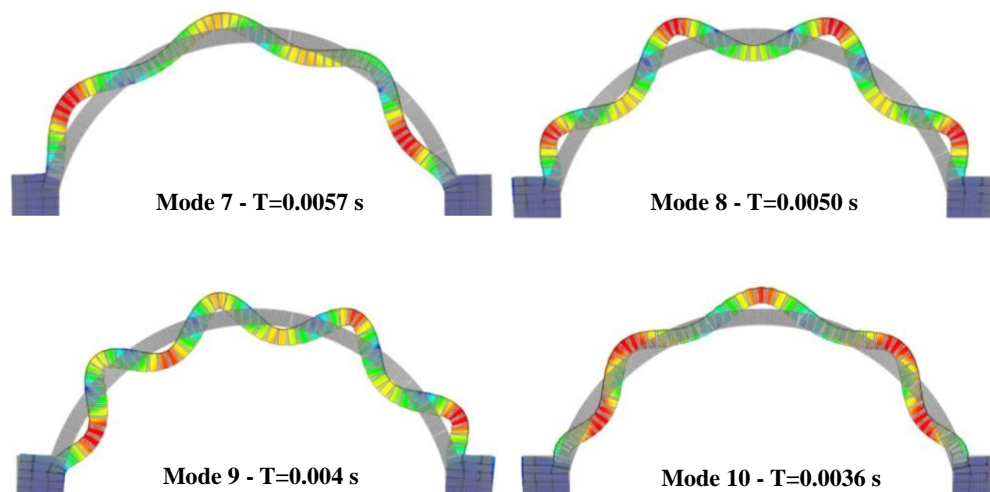


Figure 5.15 Unreinforced vault: modal shapes (mode 7-10)

5.3.2 Retrofitted vault

Similarly, the calibrated unreinforced vault FE model has been used to investigate properties of the retrofitted vault under vibrational excitation. In particular: frequencies, angular frequencies, ω , periods, T , and both participant mass in horizontal direction, M_h and in vertical direction, M_v , have been achieved for the first ten vibration modes of the unreinforced vault.

In Figure 5.16 and Figure 5.17 the modal shapes and their correspondent periods, T , are reported. As well as in the case of unreinforced vault, the results show that, higher modes involve almost negligible participating mass. According to Figure 5.16, until the fourth vibration mode there are not big differences between the unreinforced and the retrofitted vault.

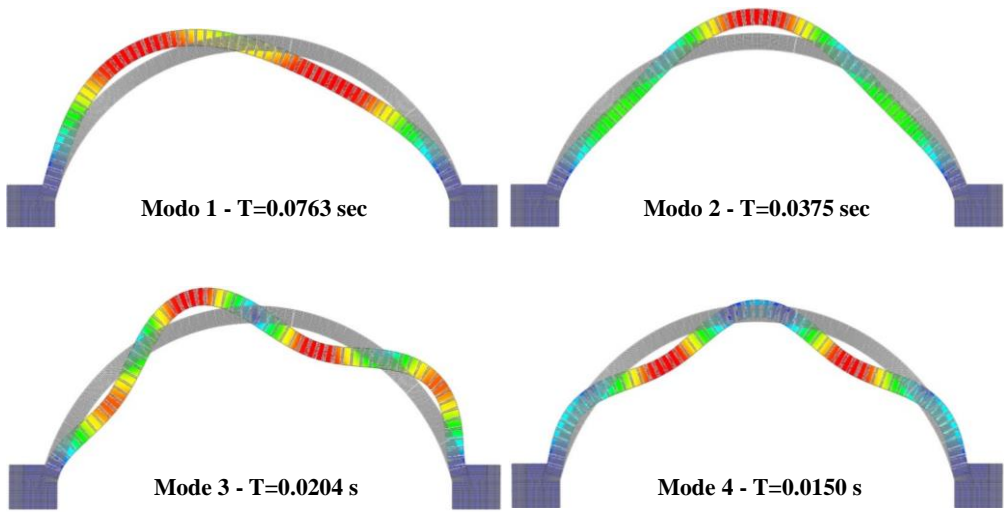


Figure 5.16 Retrofitted vault: modal shapes (mode 1-4)

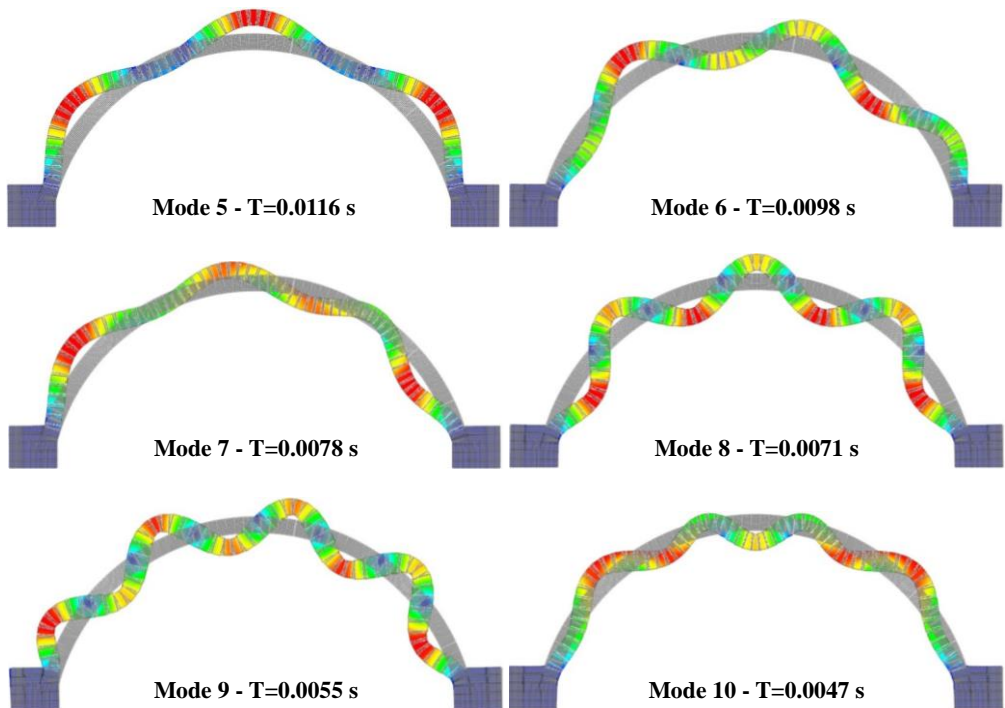


Figure 5.17 Retrofitted vault: modal shapes (mode 5-10)

In the case of unreinforced vault, the first mode involves about 42% of the participating mass in horizontal direction. Then, although it is the predominant mode, the effects of the modes higher than the first are not negligible. The largest portion of mass in vertical direction is participating at the fourth and the fifth modes. However the fourth mode involves the highest participating mass in vertical direction (about 25%). Table 5.4 lists the main outcomes of the modal analysis on the retrofitted vault. These outcomes confirm that the retrofit does not change the global dynamic behaviour of the vault.

Table 5.4: Retrofitted vault: modal properties

Mode	Frequency	ω	Period	Mh	SumMh	Mv	SumMv
[-]	[-]	[rad/s]	[s]	[-]	[%]	[-]	[%]
1	18.55	116.55	0.0539	0.425	42.5	0.000	0.0%
2	37.84	237.76	0.0264	0.000	42.5	0.081	8.1%
3	69.18	434.67	0.0145	0.122	54.7	0.000	8.1%
4	92.38	580.44	0.0108	0.000	54.7	0.253	33.3%
5	123.81	777.92	0.0081	0.000	54.7	0.169	50.3%
6	138.14	867.96	0.0072	0.090	63.7	0.000	50.3%
7	176.4	1108.35	0.0057	0.010	64.7	0.000	50.3%
8	198.42	1246.71	0.0050	0.000	64.7	0.000	50.3%
9	252.79	1588.33	0.0040	0.017	66.4	0.000	50.3%
10	275.18	1729.01	0.0036	0.000	66.4	0.089	59.1%

According to the experimental outcomes, the comparison between the unreinforced and the retrofitted vault show that the retrofit improves the

dynamic characteristics of the vault (e.g. the natural frequency). However, the global dynamic response of the vault does not drastically change.

5.4 Static nonlinear analyses

Numerical static nonlinear analyses have been performed on both the unreinforced and the retrofitted vault FE models presented in the section 5.1 and calibrated in the section 5.2. All the nonlinear analyses were performed under force control. In particular applying generalised diffused accelerations (vertical to simulate static conditions and increasing horizontal to simulate seismic response) measuring in-plane displacements. The outcomes of the static nonlinear analyses are presented in terms of force-displacement curves, deformed shapes, crack patterns and contour maps of the principal stresses both in tension and in compression.

5.4.1 Unreinforced vault

The load-displacement curve provided in Figure 5.18 shows an almost linear elastic trend until a load of about 17 kN. After the initial quasi-linear phase the trend becomes clearly nonlinear, and a gradual deterioration of the stiffness is visible. The curve has not sharp levelling off or drop. Therefore it is not possible to clearly recognise the plastic hinge formation. The analysis has been stopped for a horizontal load of about 77 kN, which correspond to an equivalent acceleration of about 3 g. Being the shaking table tests performed at lower acceleration, higher accelerations were not taken into account. The contour maps, of the principal stresses in tension and in compression are shown in Figure 5.19 and Figure 5.20 respectively.

In particular, the map in Figure 5.19 shows that the principal stresses in tension are lower than 1.4 MPa. Therefore the tensile stress state is not causing concern compared to expected strength of materials (see Table 3.1).

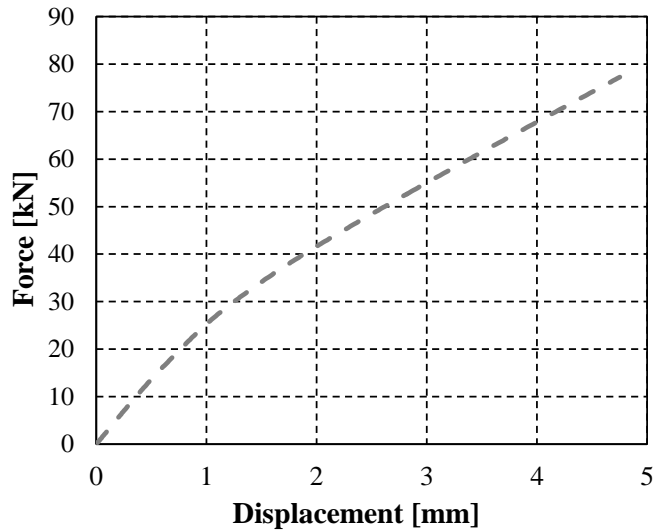


Figure 5.18 Static nonlinear analysis: unreinforced vault load-displacement curve

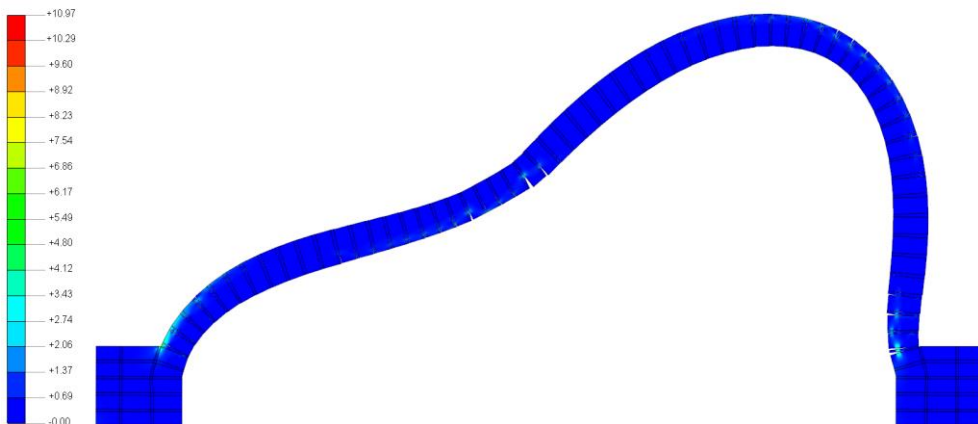


Figure 5.19 Static nonlinear analysis: unreinforced vault principal stresses in tension
(values expressed in MPa)

Similarly, the principal stresses in compression, except for the plastic hinge locations, are rather low and, in particular, lower than expected strength of materials (see Table 3.1). The stress state analysis has shown that only interfaces performed nonlinearly, while bricks and mortar remained in the elastic field.

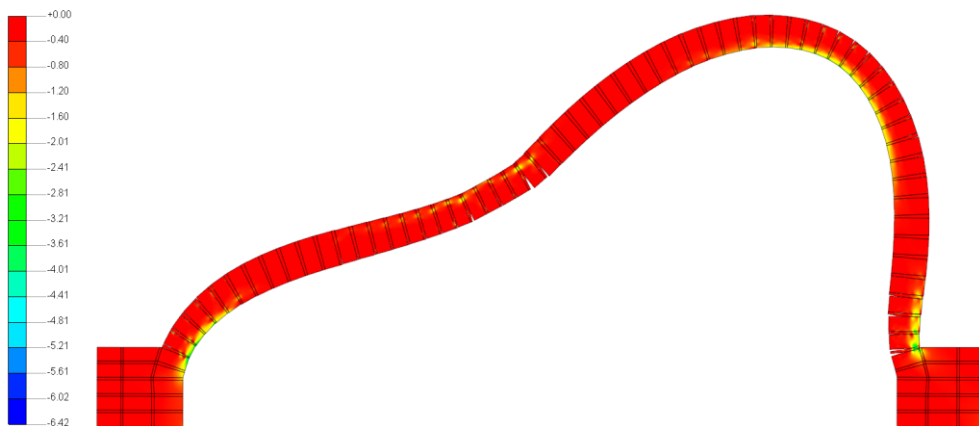


Figure 5.20 Static nonlinear analysis: unreinforced vault principal stresses in compression
(values expressed in MPa)

This result validates the assumption of modelling bricks and mortar as linear isotropic elastic materials. Finally, the joint opening shown in Figure 5.21 (the joint opening is 5X magnified), highlights the interface most critical location. Crack opening occurs at both the intrados and the extrados of the vault.

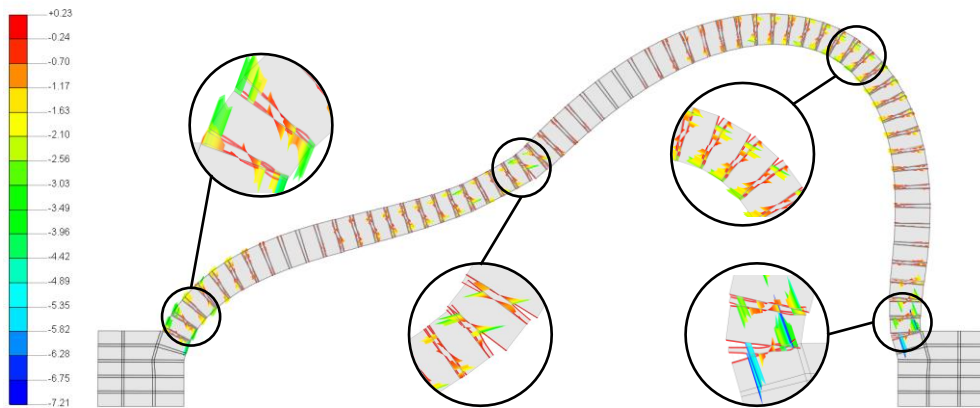


Figure 5.21 Static nonlinear analysis: unreinforced vault stresses and enlargements of joint openings at the interfaces (values expressed in MPa)

5.4.2 Retrofitted vault

The load-displacement curve provided in Figure 5.22 shows an almost linear trend until a load of about 18 kN. The elastic limit in this case is more or less the same as the previous case of unreinforced vault. However, in the case of retrofitted vault, the curve is stiffer. After the initial quasi-elastic phase the trend of the load-displacement curve becomes clearly nonlinear. Then, the curve continues to grow nonlinearly until a load of about 80 kN, after which the curve levels off, highlighting a hinge formation. Then, the curve continues to grow and then level off again in three points, highlighting the development of the classic four hinges mechanism. In particular the formation of the further three hinges occurs at a load of about 90 kN, a load of about 110 kN and a load of about 120 kN. The analysis has been stopped for a horizontal load of about 131 kN, which corresponds to an equivalent acceleration of about 5 g. Being the shaking table tests performed at lower acceleration, higher accelerations were not taken into account.

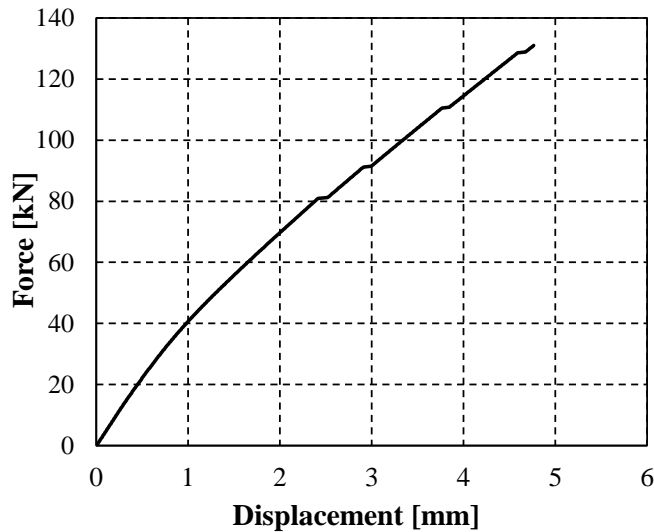


Figure 5.22 Static nonlinear analysis: retrofitted vault load-displacement curve

The contour maps of the principal stresses in tension and in compression are shown in Figure 5.23 and Figure 5.24 respectively. In particular, the map in Figure 5.23 shows that, except for the plastic hinge locations, the principal stresses in tension are lower than 2 MPa. Therefore the tensile stress state is not causing concern compared to the expected strength of materials (see Table 3.1). Similarly, the principal stresses in compression are rather low and, in particular, lower than the expected strength of materials (see Table 3.1).

Therefore, as well as the previous case, only interfaces performed nonlinearly, while bricks and mortar remained in the elastic field. This result validates the assumption of modelling bricks and mortar as linear isotropic elastic materials.

Finally, the joint opening shown in Figure 5.25 (the joint opening is 5X magnified), highlights the interface most critical location.

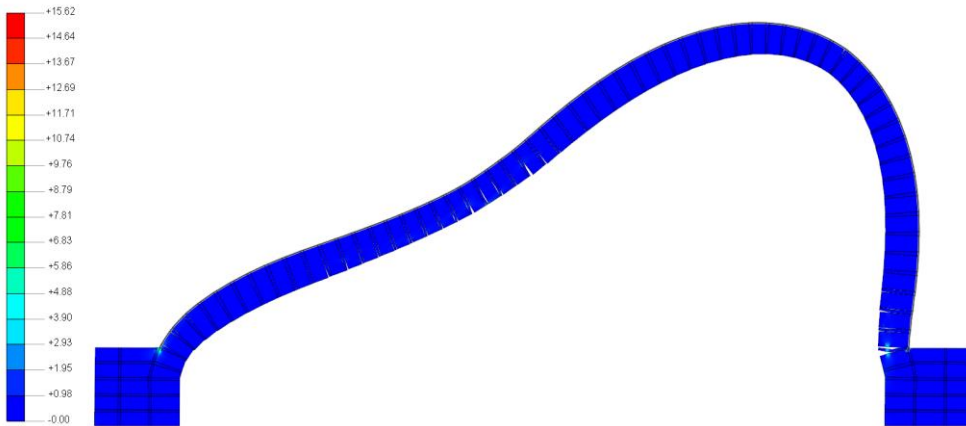


Figure 5.23 Static nonlinear analysis: retrofitted vault principal stresses in tension
(values expressed in MPa)

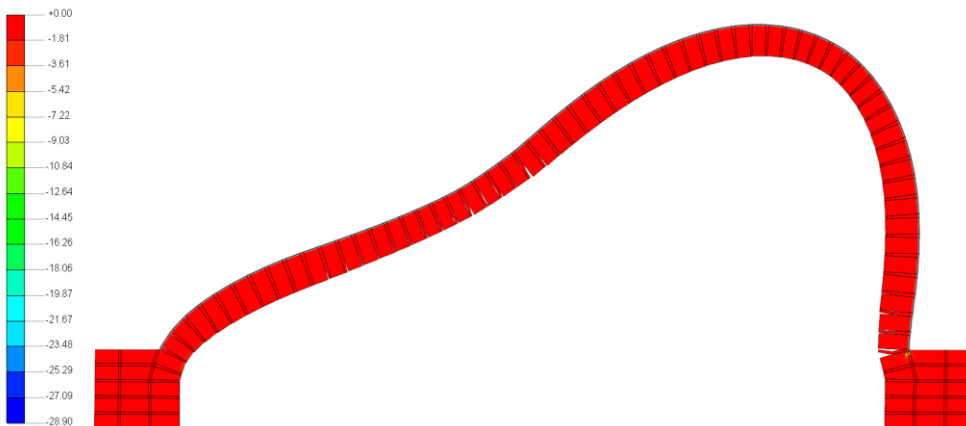


Figure 5.24 Static nonlinear analysis: retrofitted vault principal stresses in compression
(values expressed in MPa)

It is worth noting that, in this case, due to the presence of the IMG at the extrados, the crack opening occurs only at the intrados of the vault. The stress state in the IMG is always low (averagely about 20 MPa), however, at the

extrados in the locations where the plastic hinges occurred on the unreinforced model, stress peak (more than 500 MPa) has been noticed.

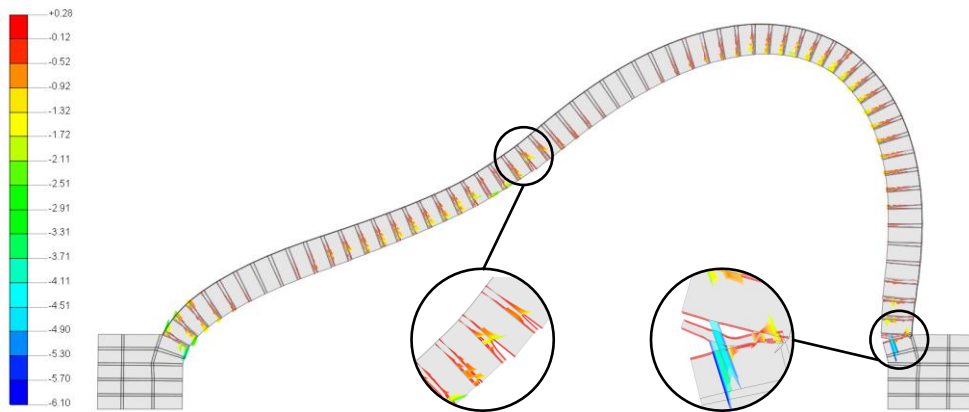


Figure 5.25 Static nonlinear analysis: retrofitted vault stresses and stresses and enlargements of joint openings at the interfaces (values expressed in MPa)

5.5 Dynamic nonlinear analyses

Dynamic nonlinear analyses have been performed on both the reinforced and the unreinforced vault FE models. The analyses are aimed to the validation of both the FE models (i.e. unreinforced and retrofitted vault). Therefore the dynamic nonlinear analyses have been performed on the FE models presented in the section 5.1 and calibrated in the section 5.2. The Newmark time integration scheme, unconditionally stable for the chosen parameters, was adopted with a time step equal to 10 ms (earthquake signal sampling was 100 Hz) to grant accuracy. In the following sections a brief review of the main modelling parameters and outcomes are provided.

The outcomes are presented in terms of maximum acceleration, dynamic amplification profiles and force-displacement graphs.

5.5.1 Rayleigh damping coefficients

The damping plays a crucial role in the structural dynamic nonlinear analysis. Indeed, as it will be discussed in the following section 5.6, it can have a strong influence on the numerical outcomes. In the assumption of proportional viscous damping, an effective way to write the damping matrix is by means of the equivalent Rayleigh damping coefficients. In particular the damping matrix can be written in the form:

$$[C] = \alpha[M] + \beta[K] \quad (5.4)$$

in which $[C]$ is the damping matrix of the physical system, $[M]$ is the mass matrix of the physical system, $[K]$ is the stiffness matrix of the system, α and β are the Rayleigh coefficients. By means of such coefficients a structure having n degrees of freedom (DOF) can be reduced to n -number of uncoupled equations by means of orthogonal transformation. In particular, in order to assess the Rayleigh coefficients, the following equation system can be considered:

$$\begin{cases} \alpha \omega_i + \frac{\beta}{\omega_i} = \zeta_i \\ \alpha \omega_j + \frac{\beta}{\omega_j} = \zeta_j \end{cases} \quad (5.5)$$

where: ζ_i and ζ_j are the damping ratios of the uncoupled modes i and j respectively, and ω_i and ω_j are the natural angular frequency of the system related to the uncoupled modes i and j respectively. Once assessed the Rayleigh coefficients, it is possible to achieve the damping of the further $n-2$ modes of the system.

Therefore, in order to simulate viscous damping, Rayleigh damping coefficients have been assessed for both the unreinforced and retrofitted vault. In particular considering the modes 1 and 3, the damping ratio achieved experimentally (see sections 3.6.1 and 4.4.1) has been assumed equal for both the modes, i.e. $\zeta_1 = \zeta_3 = \zeta$. The natural angular frequencies considered (i.e. ω_1 and ω_2) are those achieved by means of the previous dynamic linear analyses (see section 5.3). Therefore the Rayleigh damping coefficients have been achieved by means of the following relations:

$$\begin{cases} \alpha = 2 \omega_1 \omega_2 b \\ \beta = 2 b \end{cases} \quad (5.6)$$

where:

$$\begin{cases} b = \frac{(1-\delta)}{\omega_3 - \delta\omega_1} \zeta \\ \delta = \frac{\omega_1}{\omega_3} \end{cases} \quad (5.7)$$

It is worth noting that the damped system frequencies have been assumed equal to the undamped system frequencies. This assumption allows uncoupling the system equations. By means of such procedure the mode 2 exhibits a damping lower than modes 1 and the 3 (which were assumed equal).

Otherwise, all the other modes exhibit higher damping. The equivalent damping corresponding to the vibration mode, i , can be achieved as:

$$\zeta_i = \frac{1}{2} \left(\beta \omega_i + \frac{\alpha}{\omega_i} \right) \quad (5.8)$$

In the following Table 5.5 and

Table 5.6, the Rayleigh coefficient achieved for both the unreinforced and the retrofitted vault are reported.

Table 5.5: Unreinforced vault: Rayleigh coefficients

ζ [-]	ω_1 [rad/s]	ω_3 [rad/s]	δ [-]	\mathbf{b} [-]	α [-]	β [-]
0.017	116.55	434.67	0.268141	3.084E-05	3.124892831	6.1680931E-05
0.017	116.55	434.67	0.268141	3.084E-05	3.124892831	6.1680931E-05
0.019	116.55	434.67	0.268141	3.447E-05	3.492527282	6.8937511E-05
0.022	116.55	434.67	0.268141	3.991E-05	4.043978958	7.9822381E-05
0.028	116.55	434.67	0.268141	5.080E-05	5.146882310	1.0159212E-04

Table 5.6: Retrofitted vault: Rayleigh coefficients

ζ [-]	ω_1 [rad/s]	ω_3 [rad/s]	δ [-]	\mathbf{b} [-]	α [-]	β [-]
0.022	82.50	307.69	0.268123	5.638E-05	2.862435931	1.1276679E-04
0.022	82.50	307.69	0.268123	5.638E-05	2.862435931	1.1276679E-04
0.022	82.50	307.69	0.268123	5.638E-05	2.862435931	1.1276679E-04
0.032	82.50	307.69	0.268123	8.201E-05	4.163543172	1.6402442E-04

In Figure 5.26 the variation of the achieved damping ratio with natural angular frequency is reported for both the unreinforced and the retrofitted vault. As expected, the curves show two branches. The first branch is highly nonlinear, while the second branch is linear.

Therefore, for low frequency modes, the structure shows nonlinear damping properties. Otherwise the damping properties become linear when the frequency increases with each subsequent mode.

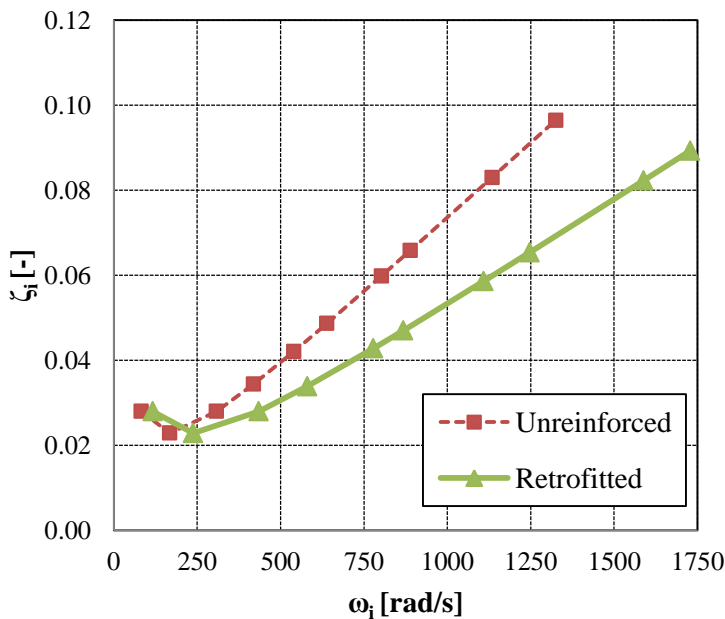


Figure 5.26 Variation of damping ratio with natural frequency

5.5.2 Input signals

The presented dynamic analyses are aimed to the validation of both the FE models (i.e. unreinforced and the retrofitted vault). Therefore, in order to compare the results, two input signals have been selected among the input signal achieved during the experimental shaking table tests (see section 3.5 and

section 4.3). In particular, the selected tests are: ART2 and ART2_R. Such signals are representative of the undamaged vault. Further achieved input signals of the most representative shaking table tests have been used to study the effect of the damping on the numerical analysis outcomes. In particular, the selected tests are: ART7, ART7_R, and ART15_R. In the following: Figure 5.27, Figure 5.28, Figure 5.29, Figure 5.30 and Figure 5.31, the input time histories and the corresponding elastic spectra are shown.

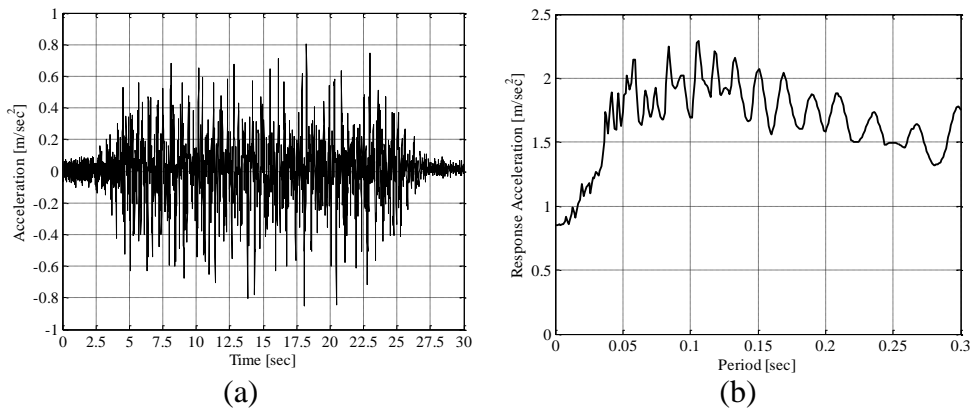


Figure 5.27 ART2: (a) time-history accelerogram; (b) elastic spectrum

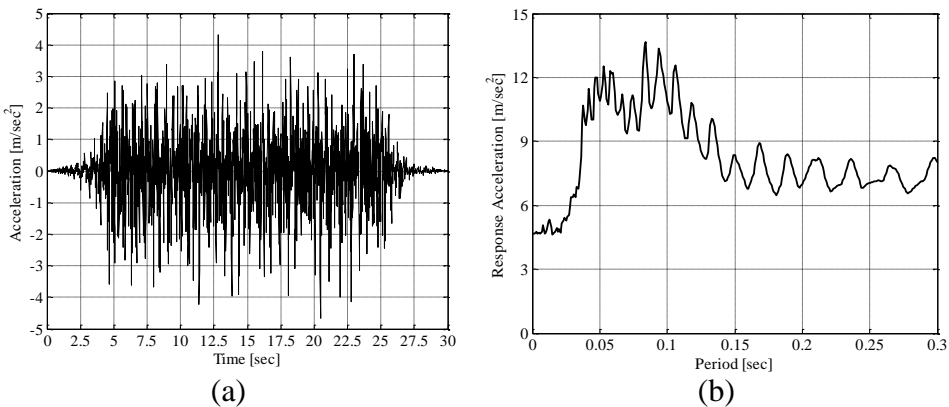


Figure 5.28 ART7: (a) time-history accelerogram; (b) elastic spectrum

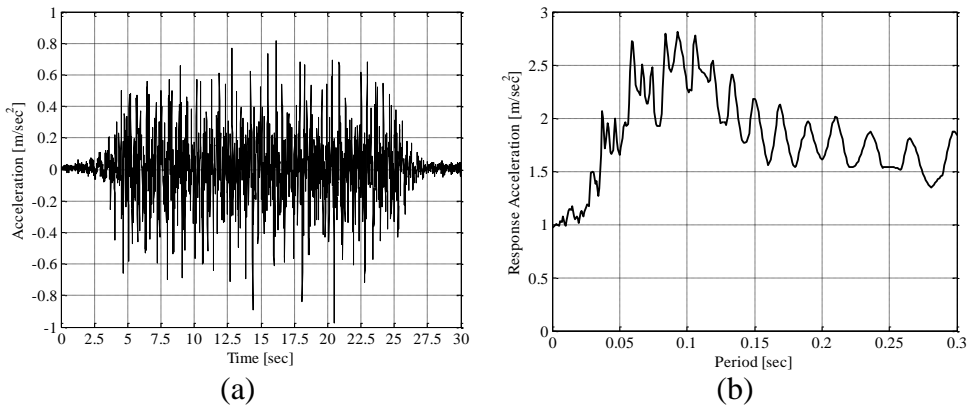


Figure 5.29 ART2_R: (a) time-history accelerogram; (b) elastic spectrum

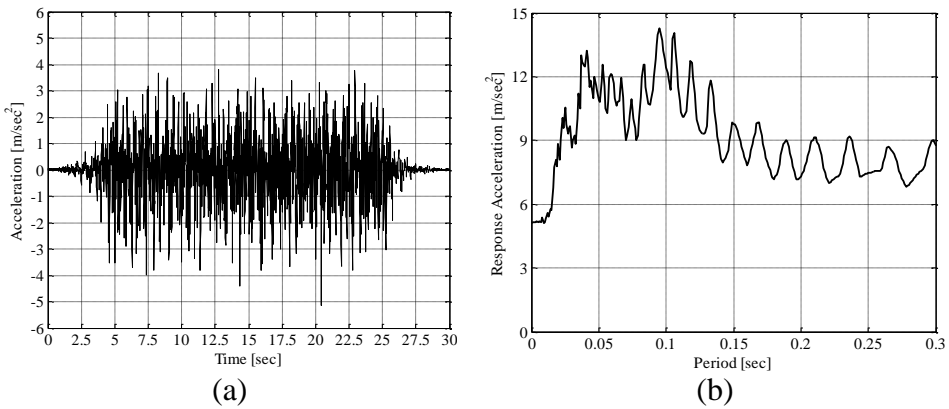


Figure 5.30 ART7_R: (a) time-history accelerogram; (b) elastic spectrum

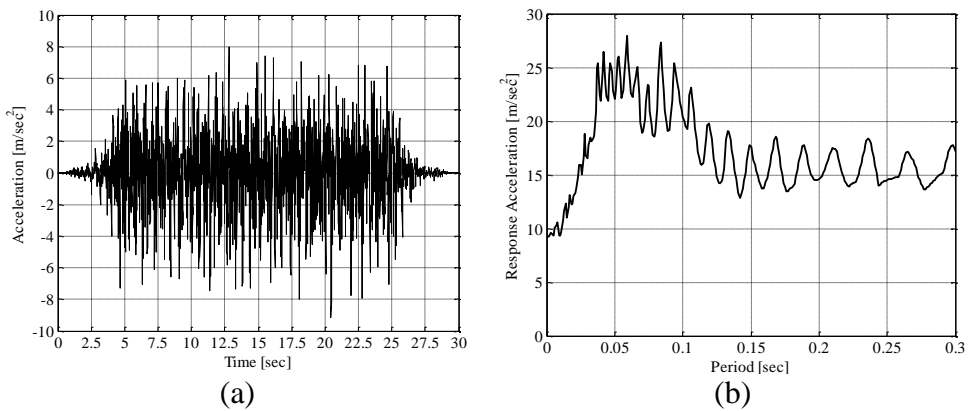


Figure 5.31 ART15_R: (a) time-history accelerogram; (b) elastic spectrum

5.5.3 Unreinforced vault: experimental-numerical comparison

In the case of unreinforced vault, the comparison between the experimental and numerical outcomes has been carried out by considering the test ART2. In particular the comparison, in terms of horizontal and vertical maximum acceleration profiles, is shown in Figure 5.32

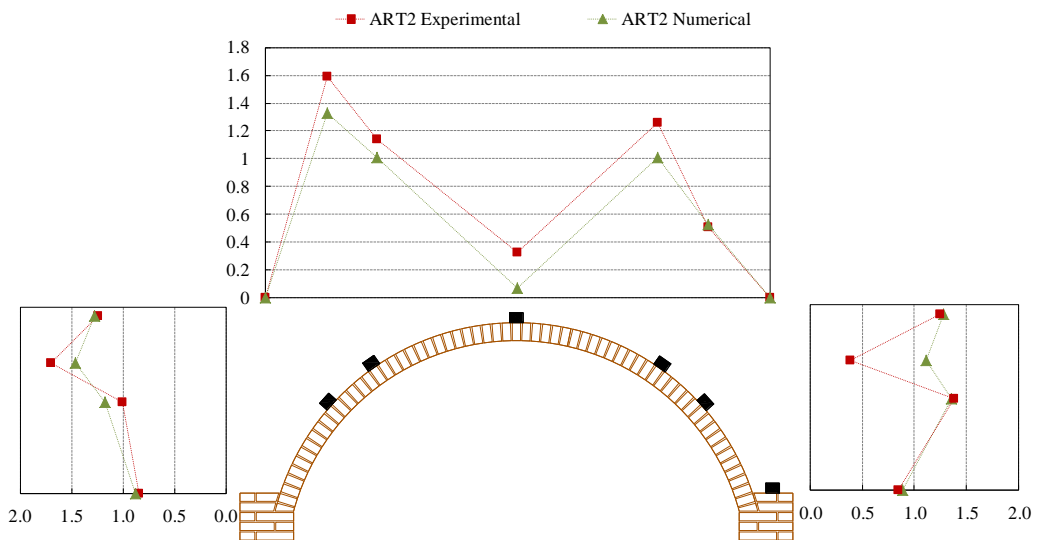


Figure 5.32 Experimental-numerical comparison test ART2: Maximum acceleration profiles (values expressed in m/s^2)

Numerical and experimental profiles, for the test ART2, exhibit the same horizontal maximum acceleration trend. In particular, almost the same maximum horizontal acceleration values have been detected in both the numerical and experimental outcomes. However at the sections at 45° from the keystone (on both the left and the right side) an offset between experimental and numerical values has been noticed. Numerical and experimental profiles exhibit the same vertical maximum acceleration trend.

However, the numerical maximum vertical accelerations values are slightly higher than the experimental. The comparison between the experimental and numerical outcomes of the test ART2 is also shown in terms of dynamic amplification profiles in Figure 5.33.

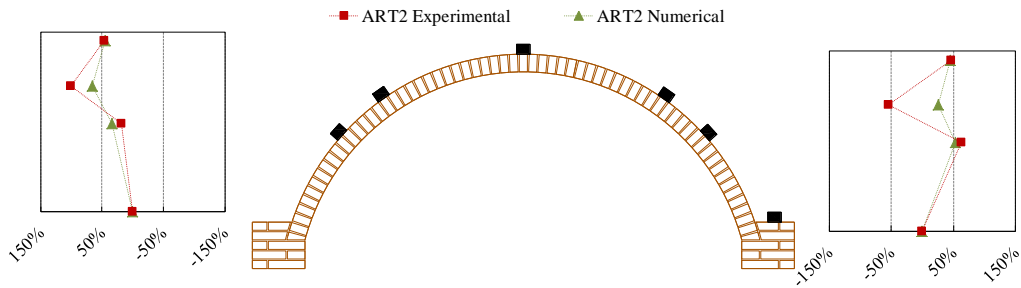


Figure 5.33 Experimental-numerical comparison test ART2: Dynamic amplification profiles (values expressed in %).

The profiles, in terms of dynamic amplification trends, show a good match between numerical and experimental outcomes.

In particular, almost the same dynamic amplification values have been detected in both the cases of numerical and experimental profiles. Nevertheless, at the sections at 45° from the keystone (on both the left and the right side), an offset between experimental and numerical values has been noticed. According to maximum horizontal acceleration profiles this outcome was expected.

Differences between experimental and numerical maximum accelerations in the some sections can be attributed to local workmanship defects which have not been modelled. The numerical force-relative displacement trend, for the test ART2, is shown in Figure 5.34. In particular, the force has been computed as the sum of the vault base reacting forces assessed at each time step; while the relative displacement has been achieved as difference between the impost and the keystone displacement.

The graph highlights several hysteretic cycles. The area subtended by the curve at each cycle can be related to the energy dissipated.

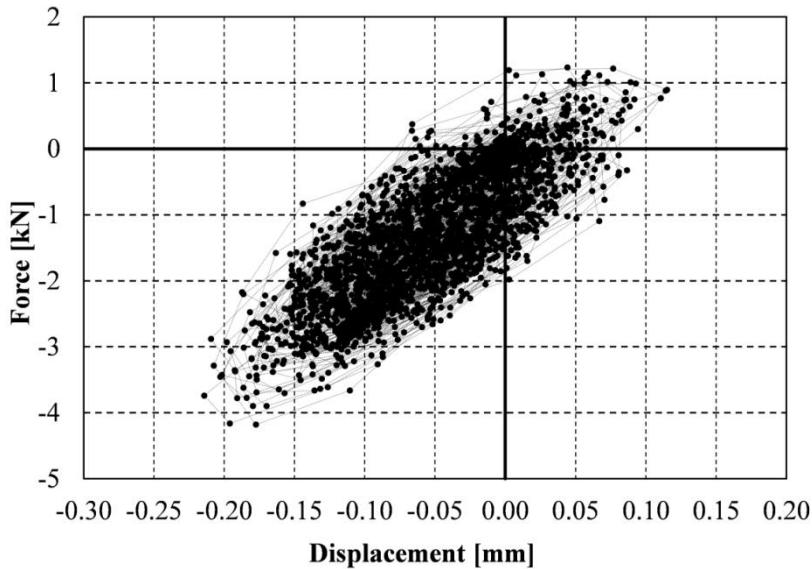


Figure 5.34 ART2: numerical force-displacement trend

5.5.4 Retrofitted vault: experimental-numerical comparison

In the case of retrofitted vault, the comparison between the experimental and numerical outcomes has been carried by considering the test ART2_R. In particular the comparison, in terms of horizontal and vertical maximum acceleration profiles, is shown in Figure 5.35. A good match, in terms of trends, has been detected, in almost all the profiles. In particular, almost the same maximum horizontal acceleration values have been detected in both the numerical and experimental outcomes. However at the section at 45° from the keystone (on the right side) an offset between experimental and numerical values has been noticed resulting in a different profile trend on the right side of the vault.

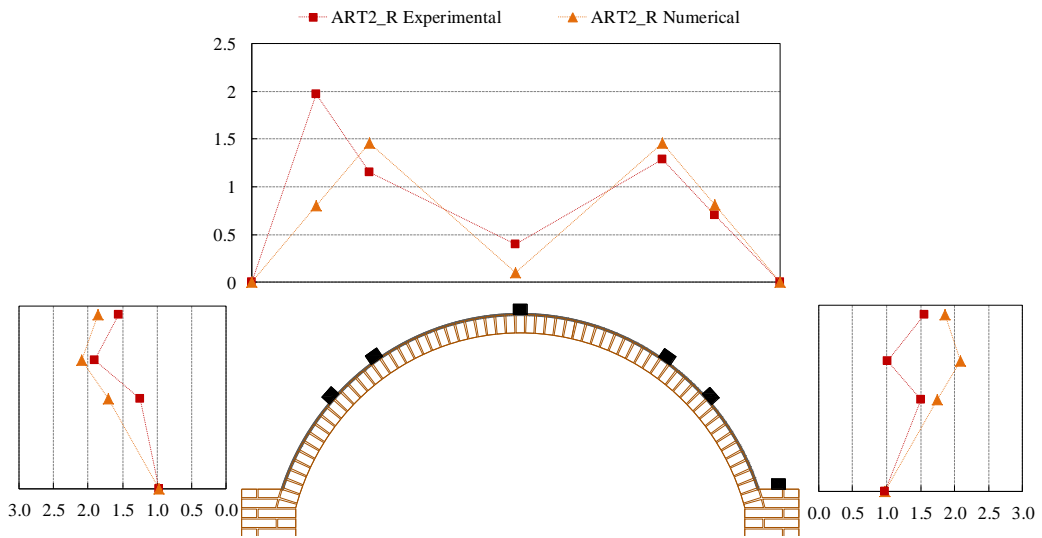


Figure 5.35 Experimental-numerical comparison test ART2_R: Maximum acceleration profiles (values expressed in m/s^2)

Slight differences, in terms of trends, have been noticed by comparing numerical and experimental maximum vertical accelerations. However the numerical simulation still catches the overall experimental behaviour. The experimental-numerical comparison in terms of dynamic amplification profiles is shown in Figure 5.36.

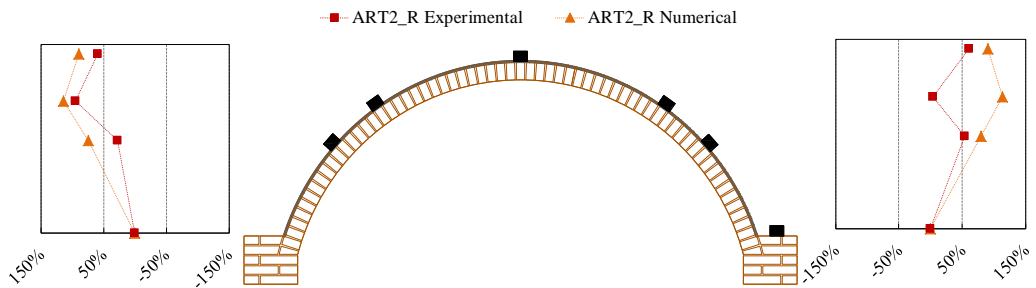


Figure 5.36 Experimental-numerical comparison test ART2_R: Dynamic amplification profiles (values expressed in %).

In particular the profiles catch the overall experimental behaviour almost in all the monitored points. Differences between experimental and numerical maximum accelerations in some points (i.e. at 45° from the keystone) can be attributed to local workmanship defects which have not been modelled.

The numerical force-relative displacement trend, for the test ART2_R, is shown in Figure 5.37. Both the force and the relative displacement have been computed as discussed in the previous section 5.5.3. As well as in the previous numerical simulation, the graph highlights several hysteretic cycles. The area subtended by the curve at each cycle can be related to the energy dissipated.

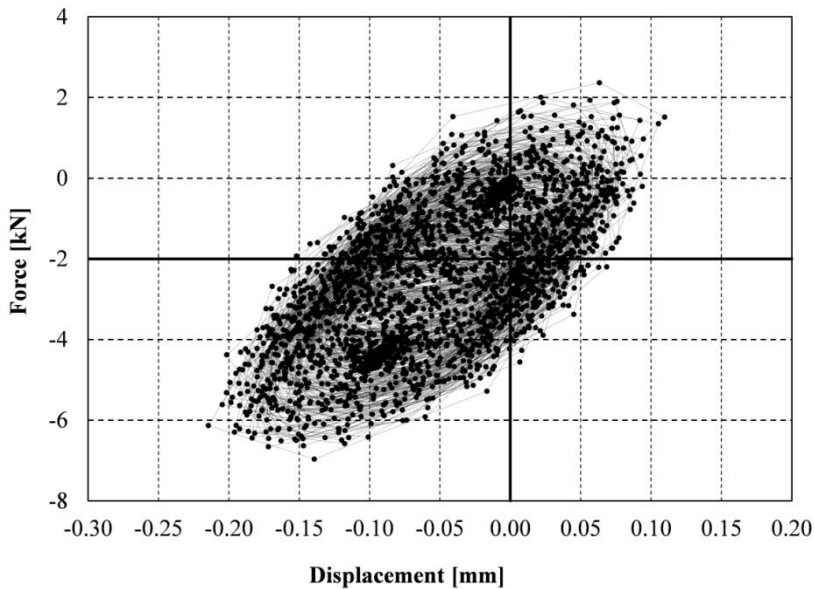


Figure 5.37 ART2_R: numerical force-displacement trend

5.6 Influence of the damage on the numerical results

The outcomes of the numerical simulations have exhibited a good agreement with the experimental outcomes in the case of undamaged vault (i.e. test ART2 and ART2_R). However, further investigations were carried out in the case of damaged vault. In particular, the experimental outcomes of the tests ART7, ART7_R were compared to the corresponding numerical outcomes in the following sections 5.6.1 and 5.6.2. Indeed, the vault was subjected to several shakes before such tests. Both local and global damages have shown to influence the numerical results. In particular, local damages, which are often due to workmanship defects, have shown to influence the behaviour of specific points of the vault. However, due to their unpredictability, it is not possible to specifically take into account, in the modelling phase, of localised workmanship defects. Global damages influence the global behaviour of the structure resulting in a variation of the structure's damping. Therefore, in the modelling phase, it is possible to take into account of the damage by assigning to the structure the proper damping parameters. However, it is not an easy task assessing the proper damping parameters corresponding to each test. A proper procedure would include, before each test, an experimental dynamic identification phase. Nevertheless, performing dynamic identification tests is not always an effective solution in terms of cost and time. Therefore parametric analyses, when varying the damping parameters, can be feasible and effective solutions. In the following section 5.6.3 a parametric analysis varying the damping is provided for a simulation of the test ART15_R.

5.6.1 ART7: experimental-numerical comparison

The comparison between the experimental and numerical outcomes of the test ART7 is shown in Figure 5.38 in terms of horizontal and vertical maximum acceleration profiles. The numerical simulation exhibits higher maximum acceleration values in almost all the points. Furthermore differences, in terms of trends, are noticed.

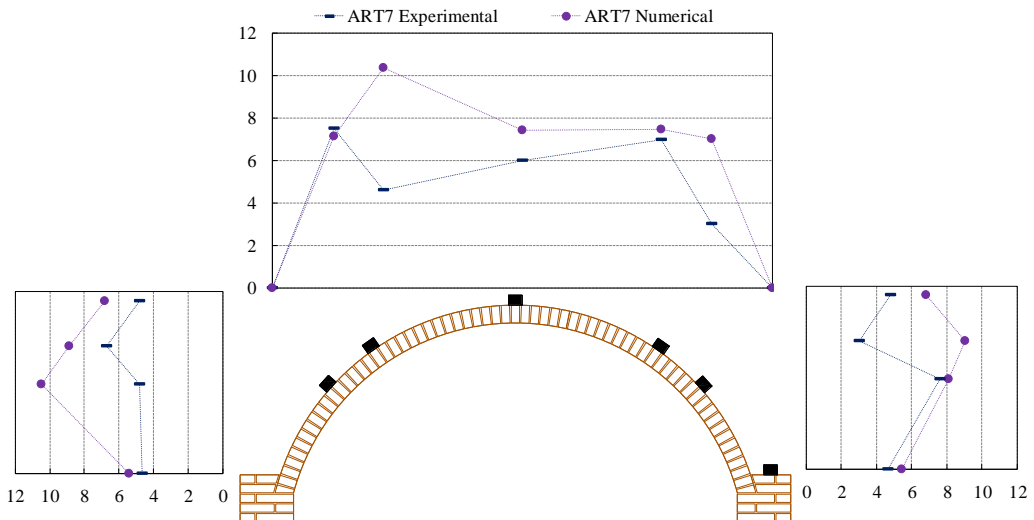


Figure 5.38 Experimental-numerical comparison test ART7: Maximum acceleration profiles (values expressed in m/s^2)

The experimental-numerical comparison in terms of dynamic amplification profiles (shown in Figure 5.39) highlights differences in terms of both trends and values. In particular the numerical simulation achieved dynamic amplifications higher than those assessed in the experimental test almost in all the points. The differences can be mainly attributed to the fact that the vault has been modelled as undamaged (i.e. by using the undamaged damping). This condition was not fully representing the experimental conditions.

Indeed, before the test ART7 the vault was already been subjected to several shakes due to the previous tests.

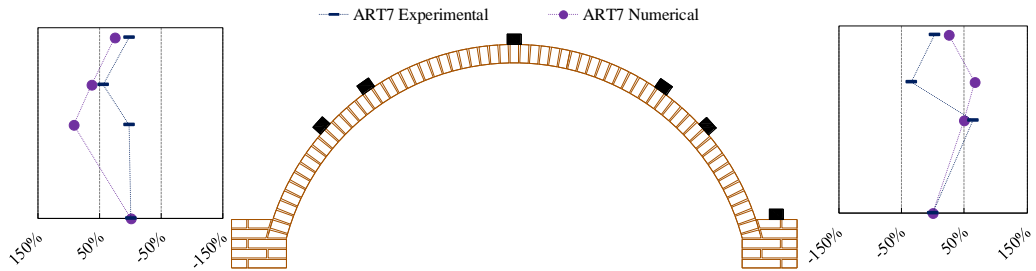


Figure 5.39 Experimental-numerical comparison test ART7: Dynamic amplification profiles (values expressed in %).

The numerical force-relative displacement trend, for the test ART7, is shown in Figure 5.40.

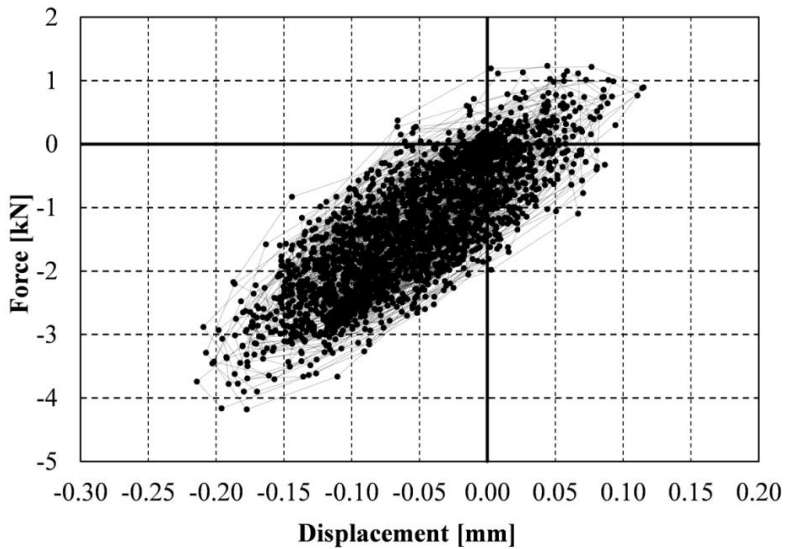


Figure 5.40 ART7: numerical force-displacement trend

Both the force and the relative displacement have been computed as discussed in the previous section 5.5.3.

The graph highlights several hysteretic cycles. The area subtended by the curve at each cycle can be related to the energy dissipated.

5.6.2 ART7_R: experimental-numerical comparison

The comparison between the experimental and numerical outcomes of the test ART7_R is shown in Figure 5.41 in terms of horizontal and vertical maximum acceleration profiles. The numerical simulation exhibits higher maximum horizontal acceleration values in almost all the points. Furthermore, differences, in terms of trends, are noticed. However, a good match, in terms of trend, has been detected on the left side of the vault. Differences, in terms of trend, have been noticed by comparing numerical and experimental maximum vertical accelerations as well. The experimental-numerical comparison in terms of dynamic amplification profiles is shown in Figure 5.42.

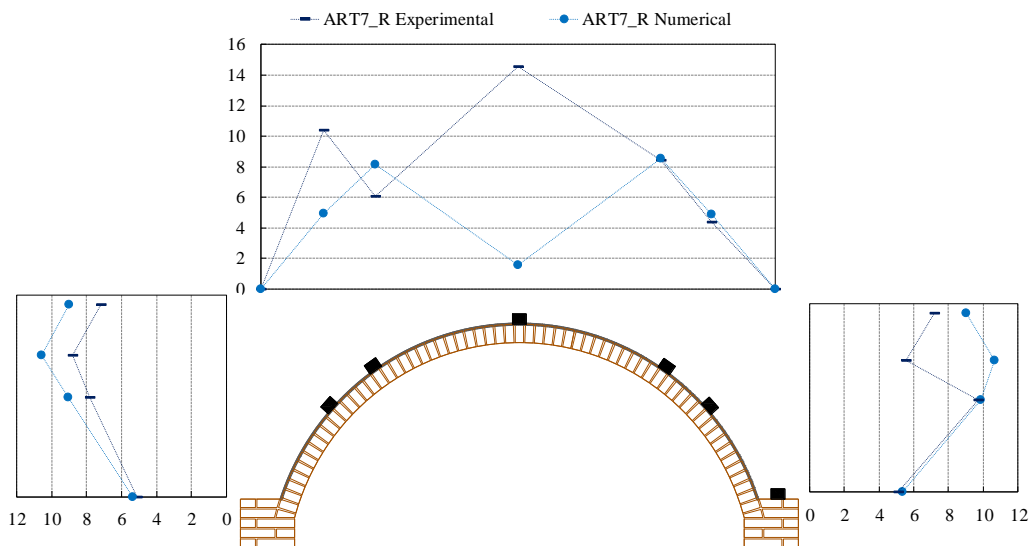


Figure 5.41 Experimental-numerical comparison test ART7_R: Maximum acceleration profiles (values expressed in m/s^2)

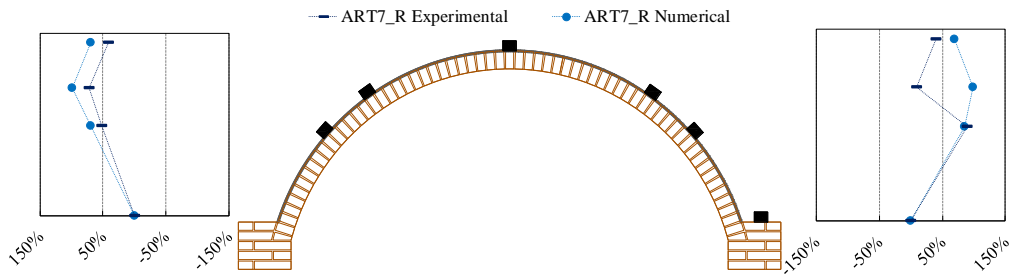


Figure 5.42 Experimental-numerical comparison test ART7_R: Dynamic amplification profiles (values expressed in %).

Analysing the dynamic amplification profiles, the differences between experimental and numerical outcomes are less evident. As well as in the previous case, the vault has been modelled as undamaged (i.e. by using the undamaged damping). Therefore, since in the experimental condition the vault was already damaged, differences between numerical and experimental were expected. The numerical force-relative displacement trend, for the test ART7_R, is shown in Figure 5.43.

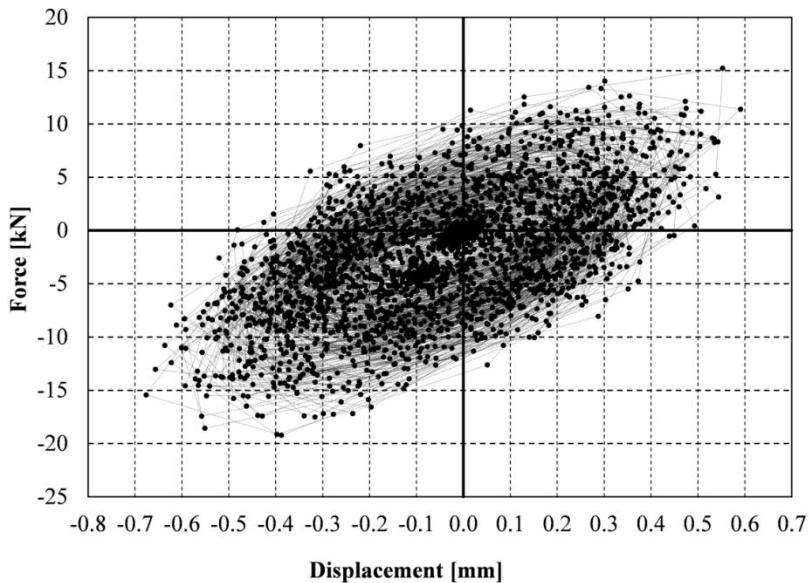


Figure 5.43 ART7_R: numerical force-displacement trend

Both the force and the relative displacement have been computed as discussed in the previous section 5.5.3. The graph highlights several hysteretic cycles. The area subtended by the curve at each cycle can be related to the energy dissipated. The same conclusions were drawn by analysing the experimental-numerical comparisons of the test ART15_R. Plots of the comparisons are available in Appendix C.

5.6.3 Parametric analyses (damping influence)

As shown by the experimental-numerical comparison of the tests ART7, ART7_R and ART15_R, the damage influences the numerical results. Therefore it has to be taken into account in the modelling phase. In particular, in the modelling phase, the damage can be taken into account by means of the damping ratio. However, as discussed in the section 5.6, assessing the proper damping parameters is not an easy task. Therefore, in order to study the influence of such parameters, on the numerical outcomes, parametric analyses have been performed varying the vault's damping ratio. The parametric analyses have been performed considering the test ART15_R (i.e. the test in which the vault was more damaged). In particular three different damping ratios have been considered: 2.8%, 5% and 10%. The results of the parametric study have been presented in terms of comparisons between the experimental and numerical outcomes. The horizontal component of the experimental time-history ART15_R (acceleration recorded at the keystone location) has been compared to the numerical time-histories (achieved at the same location) when varying the damping ratio. In particular, the experimental time-history is compared to: the numerical time-history (2.8% damping) in Figure 5.44, the numerical time-history (5% damping) in Figure 5.45 and the numerical time-history (10% damping) in Figure 5.46.

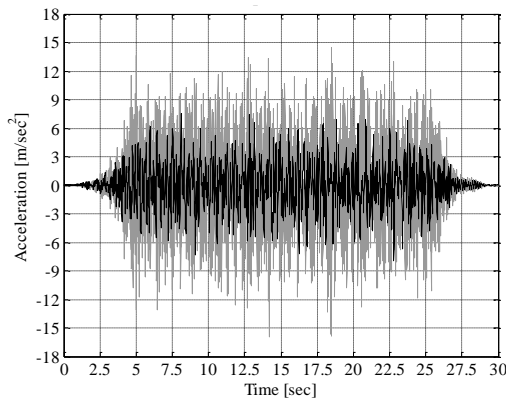


Figure 5.44 ART15_R: experimental (in black) and numerical 2.8% damping (in grey)

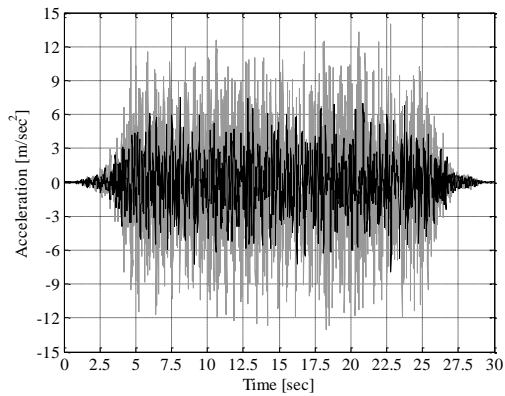


Figure 5.45 ART15_R: experimental (in black) and numerical 5% damping (in grey)

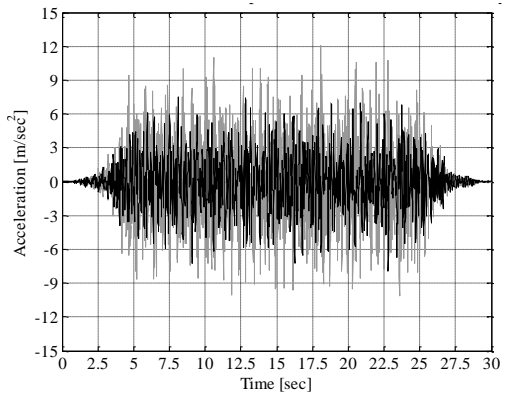


Figure 5.46 ART15_R: experimental (in black) and numerical 10% damping (in grey)

As expected, the comparisons highlight that the numerical time-histories become closer to the experimental ones when increasing the damping ratio. Moreover, according to Figure 5.44, it's clear that the damping 2.8% was not suitable to simulate the test ART15_R. Further comparisons have been provided in terms of maximum accelerations and dynamic amplifications profiles. In particular, the numerical maximum accelerations profiles, when varying the damping ratio, have been compared to the experimental profiles in Figure 5.47.

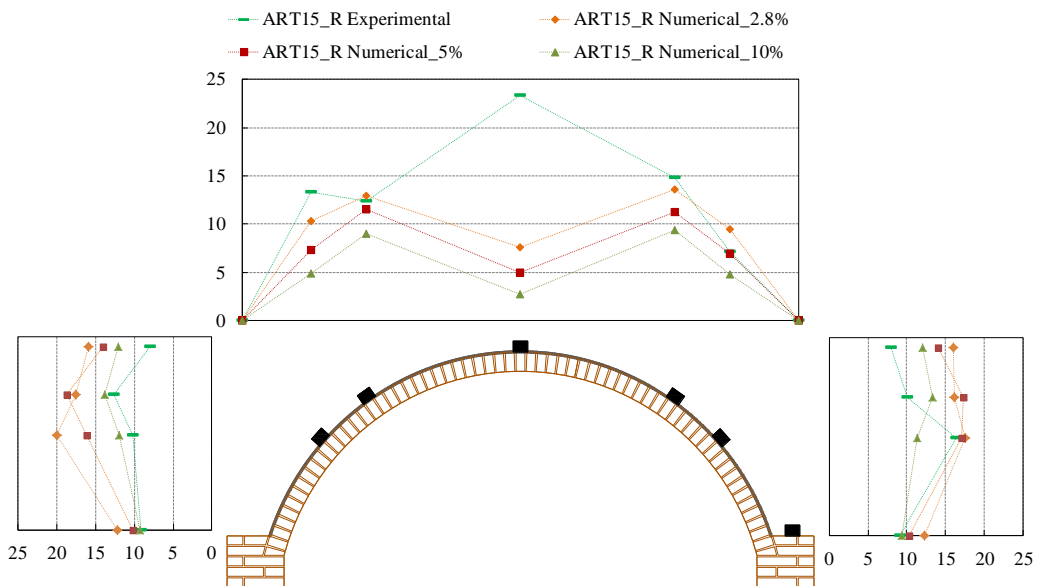


Figure 5.47 Experimental-numerical comparison test ART15_R: Maximum acceleration profiles (values expressed in m/s^2)

By analysing the profiles it is evident that the numerical profiles become closer to the experimental ones when the damping ratio increases. Furthermore, higher damping ratio profiles exhibit trends closer to the experimental trend.

However, at the keystone location, a difference between experimental and numerical values is still marked. Nevertheless, such difference can be attributed to local damage probably due to workmanship defects (which have not been modelled).

The comparison between experimental and numerical outcomes (when varying the damping ratio) in terms of dynamic amplification profiles is provided in Figure 5.48. In this case, when increasing the damping ratio, no major differences have been noticed. Indeed the numerical dynamic amplifications seem to be stable when varying the damping ratio.

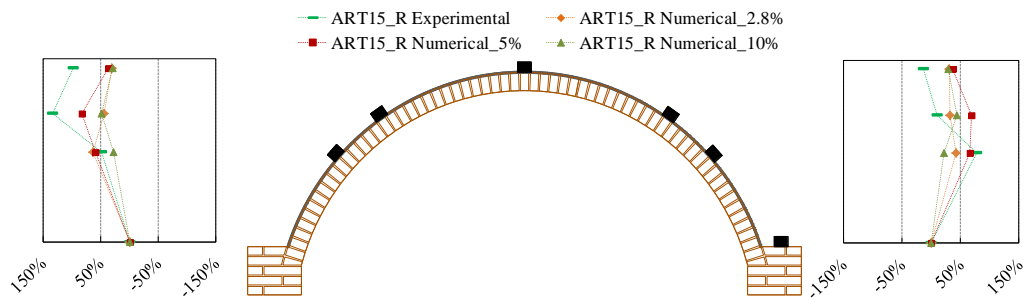


Figure 5.48 Experimental-numerical comparison test ART15_R: Dynamic amplification profiles (values expressed in %)

5.7 Conclusions

Numerical FE models able to predict the dynamic behaviour of masonry vaults (before and after the retrofit), have been developed. The mechanical parameters adopted in the material modelling were achieved by means of previous characterization tests. However, since the experimental outcomes showed that the parameter governing the system was the interface between mortar and bricks, the modelling of such parameter has been refined.

Nevertheless, no direct experimental data were available about the interface behaviour, therefore a calibration was necessary. The calibration of the interface modelling parameters has been carried out by means of best fitting of experimental test outcomes. In particular, the interface linear parameters (i.e. normal and shear stiffness) have been calibrated by comparing the outcomes of the experimental dynamic identification to the numerical dynamic linear analyses. Conversely, the nonlinear parameter (i.e. cohesion) has been calibrated by means of an experimental vertical load test. Further numerical analyses confirmed the reliability of the calibrated parameters.

Additional static nonlinear analyses allowed studying the stress state and validating the modelling assumption of elastic linear material (adopted for both bricks and mortar). Finally dynamic nonlinear analyses completed the validation of the model. In particular, the outcomes of the experimental shaking table tests have been compared to the numerical outcomes showing a good match. Further dynamic-nonlinear analyses highlighted the need to update the models at each test with a proper damping ratio, in order to take into account of the vault damage. Then, parametric dynamic nonlinear analyses confirmed the influence of the damping parameter on the numerical outcomes.

Chapter 6

Conclusions

The vaults represent an artistic valuable element in the historical heritage buildings. Consequently, the understanding of their seismic performance, as well as potential retrofit techniques, meets also the need to protect cultural heritage buildings against earthquakes.

Therefore, aims of this thesis were: to improve the knowledge on the vault dynamic behaviour; to study the effects of innovative retrofit techniques such as IMG; to develop reliable numerical models able to predict the dynamic behaviour of masonry vaults (before and after the retrofit). In order to achieve these goals a multi-scale approach has been adopted. Both experimental tests and numerical analyses have been performed.

The shaking table tests, on the unreinforced vault, were performed by means of two sets of time-history accelerograms (natural and artificial). Preliminarily, a set of random accelerograms were performed on dynamic identification purpose. In particular, a natural frequency of 13.1 Hz and a damping ratio ranging between 2.2% and 3.2% have been evaluated. The outcomes, in terms

of accelerations measured on the structure, highlighted in almost in all the sections a dynamic amplification of the base horizontal excitation. Furthermore, although the shaking is applied only in the horizontal direction, significant vertical accelerations have been detected. The tested structure exhibits good seismic behaviour, showing very slight damage only after the last test performed with an achieved PGA of 4.67 m/s^2 . In particular, only minor cracking at the interface between mortar and brick has been observed at both the intrados and the extrados of the vault.

The shaking table tests on the retrofitted vault were performed by means of a single set of artificial time-history accelerograms. As well as the previous tests, preliminarily, a set of random accelerograms were performed on dynamic identification purpose. In particular, a natural frequency of 19.3 Hz and a damping ratio ranging between 1.7% and 2.8% have been evaluated. Therefore the effect of the retrofit resulted in both a significant increase of stiffness and a decrease of damping ratio. Furthermore, both the stiffness reduction and the damping ratio increase trends, when varying the PGA, are steeper in the case of unreinforced vault. This result remarks an improvement in terms of capacity due to the retrofit interventions.

As well as in the case of unreinforced vault, the outcomes, in terms of accelerations measured on the structure, highlighted in the most of sections a dynamic amplification of the base horizontal excitation. Due to the higher stiffness, the maximum accelerations recorded on the retrofitted vault were higher than those recorded on the unreinforced vault. However, both the maximum acceleration trends and the dynamic amplification trends remained almost the same after the retrofit interventions.

The retrofitted vault exhibits a good dynamic behaviour, showing very slight damage only after the last test performed with an achieved PGA of 11.70 m/s^2 . In particular, cracking at the interface between mortar and brick has been observed only at the intrados of the vault.

These findings suggest that the retrofit improve the stiffness and the seismic capacity of the vault. However the global dynamic behaviour of the vault does not change when the vault is retrofitted.

Numerical FE models able to predict the dynamic behaviour of masonry vaults (before and after the retrofit), have been developed. The mechanical parameters adopted in the material modelling were achieved by means of previous characterization tests. However, since the experimental outcomes showed that the parameter governing the system was the interface between mortar and bricks, the modelling of such parameter has been refined. Nevertheless, no experimental data were available about the interface behaviour, therefore a calibration was necessary. The calibration of the interface modelling parameters has been carried out by means of best fitting of experimental test outcomes. In particular, the interface linear parameters (i.e. normal and shear stiffness) have been calibrated by comparing the outcomes of the experimental dynamic identification to the numerical dynamic linear analyses. Conversely, the nonlinear parameter (i.e. cohesion) has been calibrated by means of an experimental vertical load test. Further numerical analyses confirmed the reliability of the calibrated parameters.

Additional static nonlinear analyses allowed studying the stress state and validating the modelling assumption of elastic linear material (adopted for both bricks and mortar). Finally dynamic nonlinear analyses completed the validation of the model. In particular, the outcomes of the experimental shaking

table tests have been compared to the numerical outcomes showing a good agreement.

Further dynamic-nonlinear analyses highlighted the need to update the models at each test with a proper damping ratio, in order to take into account of the vault damage. Then, parametric dynamic nonlinear analyses confirmed the influence of the damping parameter on the numerical outcomes.

References

- [1] F. Parisi, and N. Augenti, "Earthquake damages to cultural heritage constructions and simplified assessment of artworks," *Engineering Failure Analysis*, vol. 34, no. 0, pp. 735-760, 12//, 2013.
- [2] I. Iovinella, and A. Balsamo, (*Unpublished pictures*), The pictures are reprinted with permission of the authors
- [3] N. Augenti, and F. Parisi, (*Unpublished pictures*), The pictures are reprinted with permission of the authors
- [4] F. Parisi, I. Iovinella, A. Balsamo *et al.*, "In-plane behaviour of tuff masonry strengthened with inorganic matrix-grid composites," *Composites Part B-Engineering*, vol. 45, no. 1, pp. 1657-1666, Feb, 2013.
- [5] G. P. Lignola, A. Prota, and G. Manfredi, "Nonlinear Analyses of Tuff Masonry Walls Strengthened with Cementitious Matrix-Grid Composites," *Journal of Composites for Construction*, vol. 13, no. 4, pp. 243-251, Jul-Aug, 2009.
- [6] A. Prota, G. Marcari, G. Fabbrocino *et al.*, "Experimental in-plane behavior of tuff masonry strengthened with cementitious matrix-grid composites," *Journal of Composites for Construction*, vol. 10, no. 3, pp. 223-233, May-Jun, 2006.
- [7] C. G. Papanicolaou, T. C. Triantafillou, M. Papathanasiou *et al.*, "Textile reinforced mortar (TRM) versus FRP as strengthening material of URM walls: out-of-plane cyclic loading," *Materials and Structures*, vol. 41, no. 1, pp. 143-157, Jan, 2008.
- [8] M. Maalej, V. W. J. Lin, M. P. Nguyen *et al.*, "Engineered cementitious composites for effective strengthening of unreinforced masonry walls," *Engineering Structures*, vol. 32, no. 8, pp. 2432-2439, Aug, 2010.
- [9] W. Wittmann, "Theorie der Gewölbe," *Zeitschrift für Bauwesen*, vol. Bd. 29, pp. 61-74, 1879.
- [10] D. Proske, and P. V. Gelder, *Safety of historical stone arch bridges*, London: Springer, 2009.
- [11] K. E. Kurrer, *Geschichte der Baustatik*, Berlin: Ernst und Sohn Verlag für GmbH, 2002.
- [12] B. Fletcher, and F. B. Fletcher, *A history of architecture on the comparative method*, London: B.T. Batsford, 1896.

-
- [13] P. Couplet, *De la poussé e des voûtes*, p.^pp. 79-117, Paris: Histoire de l'Accadémie royale, 1729-1730.
- [14] J. Heyman, *The stone skeleton. Structural engineering of masonry architecture*, Cambridge: Cambridge University Press, 1995.
- [15] J. Heyman, "The stone skeleton " *International Journal of Solids and Structures*, vol. 2, pp. 249-279, 1966.
- [16] M. J. De Jong, "Seismic Assessment Strategies for Masonry Structures," Ph.D., Department of Architecture, Massachusetts Institute of Technology, 2009.
- [17] S. Huerta, "Mechanics of masonry vaults: the equilibrium approach," in *Historical Constructions*, 2001.
- [18] V. Apreutesei, and D. V. Oliveira, *Strengthening of stone masonry arch bridges three leaf masonry walls-state of the art*, Universidade do Minho, Guimaraes (Portugal), 2005.
- [19] H. Moseley, "On the theory of the arch " *The theory, practice and architecture of bridges of stone, iron, timber and wire with examples on the principle of suspension*, 1843.
- [20] M. Milankovitch, "Theorie der Druckkurven," *Zeitschrift für Mathematik und Physik*, vol. 55, pp. 1-27. , 1907, 1907.
- [21] D. Gregory, "Catenaria," vol. 19, 1697.
- [22] R. Hooke, *A description of helioscopes, and some other instruments*, London., 1675.
- [23] J. Heyman, *The science of structural engineering*, London: Imperial College Press, 1999.
- [24] A. Castigliano, "Formule razionali ed esempi numerici per il calcolo pratico degli archi metallici e delle volte a botte murali " *L'ingegneria civile e le arti industriali*, vol. 2, pp. 129-135; 145-153, 1876.
- [25] E. Winkler, "Lage der Stützlinie im Gewölbe," *Deutsche Bauzeitung*, vol. 13, 14, pp. 117-119; 127-130; 58-60., 1879
- [26] M. A. Howe, *A treatise on arches, designed for the use of engineers and students in technical schools*, New York J. Wiley, 1906.
- [27] A. A. Gvozdev, "The determination of the value of collapse load for statically indeterminate systems undergoing plastic deformation," *International Journal of Mechanical Sciences*, vol. 1, pp. 322-35, 1960.
- [28] J. Heyman, *Structural analysis: a historical approach*, Cambridge: Cambridge University Press, 1998.
- [29] G. Poleni, *Memorie storiche della gran cupola del Tempio Vaticano*, Padova: Stamperia del Seminario, 1748.

-
- [30] F. S. Huerta, *Arcos bóvedas y cúpulas. Geometría y equilibrio en el cálculo tradicional de estructuras de fábrica*, Madrid: Instituto Juan de Herrera, 2004.
- [31] K. Culmann, *Die graphische Statik*, Zurich: Meyer und Zeller, 1866.
- [32] G. Snell, "On the stability of arches," *Minutes and Proceedings of the Institution of Civil Engineers*, vol. 5, pp. 439-476, 1846.
- [33] P. Block, "Equilibrium systems: Studies in masonry structure," M.S., Massachusetts Institute of Technology, Cambridge, Massachusetts, 2005.
- [34] W. Zalewski, and E. Allen, *Shaping Structures: Statics*, New York: John Wiley and Sons, 1999.
- [35] E. Allen, and W. Zalewski, *Form and forces: Designing efficient, expressive structures*, New York: John Wiley and Sons, 2009.
- [36] I. J. Oppenheim, "The masonry arch as a four-link mechanism under base motion," *Earthquake Engineering and Structural Dynamics*, vol. 21, pp. 1005-1017, 1992.
- [37] P. Clemente, "Introduction to dynamics of stone arches," *Earthquake Engineering & Structural Dynamics*, vol. 27, no. 5, pp. 513-522, May, 1998.
- [38] J. Appleton, "Earthquake response of arches," University of Cambridge, Cambridge, UK., 1999.
- [39] J. A. Ochsendorf, "Collapse of Masonry Structures," Ph.D., University of Cambridge, Cambridge, UK, 2002.
- [40] L. De Lorenzis, M. DeJong, and J. Ochsendorf, "Failure of masonry arches under impulse base motion," *Earthquake Engineering & Structural Dynamics*, vol. 36, no. 14, pp. 2119-2136, 2007.
- [41] M. A. Crisfield, *Finite element and mechanism methods for the analysis of masonry and brickwork arches*, Crowthorne (UK): TRL, 1985.
- [42] F. Sawko, and K. Towler, "Structural behaviour of brickwork arches." pp. 160-168.
- [43] L. Pelà, A. Aprile, and A. Benedetti, "Comparison of seismic assessment procedures for masonry arch bridges," *Construction and Building Materials*, vol. 38, no. 0, pp. 381-394, 1//, 2013.
- [44] E. Scheibmeir, "Nonlinear seismic analysis of masonry arch bridge," MSc, Universitat Politècnica de Catalunya 2012.
- [45] ICOMOS, "International Charter for the Conservation and Restoration of Monuments and Sites (Venice Charter)," in IInd International Congress of Architects and Technicians of Historic Monuments, Venice (Italy), 1964.

-
- [46] A. Borri, and G. Castori, "Research on composite strengthening of historical housebuilding: retrofitting intervention for masonry arches and vaults," in VI International Conference on Structural Analysis of Historic Construction, SAHC08, Bath (UK), 2008, pp. 921–929.
- [47] S. Mastrodicasa, *Dissesti Statici Delle Strutture Edilizie*, Milano: Hoepli, 1993.
- [48] G. Cangi, *Manuale del recupero strutturale e antisismico (in Italian)*: DEI Tipografia del Genio Civile, 2012.
- [49] M. Gilbert, "Limit analysis applied to masonry arch bridges: state-of-the-art and recent developments" in 5th International Conference on Arch Bridges, Madeira (Portugal), 2007.
- [50] A. Chakrabarti, D. Menon, and A. K. Sengupta, *Handbook on Seismic Retrofit of Buildings*: Alpha Science International Limited, 2008.
- [51] R. Umbria, *Manuale per la ricostruzione post-sismica degli edifici (in Italian)*: DEI Tipografia del Genio Civile 1999.
- [52] M. A. Pisani, *Consolidamento delle strutture: Guida ai criteri, ai materiali e alle tecniche più utilizzati (in Italian)*, Milano: Hoepli 2012.
- [53] A. L. Pfeister, "Grouting for Caesar: The Vault Complex and High Level Aqueduct at Caesarea After 20 Years," Israel Antiquities Authority and International Conservation Center, Citta di Roma, 2012.
- [54] G. Calvi, and G. Magenes, "Experimental results on unreinforced masonry shear walls damaged and repaired." pp. 509-518.
- [55] S. Perret, K. Khayat, E. Gagnon *et al.*, "Repair of 130-Year Old Masonry Bridge using High-Performance Cement Grout," *Journal of Bridge Engineering*, vol. 7, no. 1, pp. 31-38, 2002.
- [56] M. Corradi, C. Tedeschi, L. Binda *et al.*, "Experimental evaluation of shear and compression strength of masonry wall before and after reinforcement: Deep repointing," *Construction and Building Materials*, vol. 22, no. 4, pp. 463-472, 2008.
- [57] L. Jurina, "L'arco armato: una nuova tecnica di consolidamento di archi e volte in muratura con uso di tiranti metallici," in XVI Convegno CTA, Ancona (Italy), 1997.
- [58] L. Jurina, "Strengthening of masonry arch bridges with "RAM" – Reinforced Arch Method."
- [59] Y. Chen, A. F. Ashour, and S. W. Garrity, "Modified four-hinge mechanism analysis for masonry arches strengthened with near-surface reinforcement," *Engineering Structures*, vol. 29, no. 8, pp. 1864-1871, 2007.

-
- [60] S. K. Sumon, "Repair and strengthening of a damaged arch with built-in ring separation."
- [61] G. Milani, "FE homogenized limit analysis model for masonry strengthened by near surface bed joint FRP bars," *Composite Structures*, vol. 92, no. 2, pp. 330-338, 2010.
- [62] G. P. Lignola, F. Ceroni, A. Balsamo *et al.*, "Externally Bonded Masonry Structures," *Wiley Encyclopedia of Composites*: John Wiley & Sons, Inc., 2011.
- [63] M. Valluzzi, M. Valdemarca, and C. Modena, "Behavior of Brick Masonry Vaults Strengthened by FRP Laminates," *Journal of Composites for Construction*, vol. 5, no. 3, pp. 163-169, 2001.
- [64] A. Barbieri, A. Borri, M. Corradi *et al.*, "Dynamic Behaviour of Masonry Vaults Repaired with FRP: Experimental Analysis," in 6th Int. Masonry Conference, London (UK), 2002.
- [65] G. M. Calvi, G. R. Kingsley, and G. Magenes, "Testing of Masonry Structures for Seismic Assessment," *Earthquake Spectra*, vol. 12, no. 1, pp. 145-162, 1996/02/01, 1996.
- [66] T. E. Boothby, "Analysis of masonry arches and vaults," *Progress in Structural Engineering and Materials*, vol. 3, no. 3, pp. 246-256, 2001.
- [67] P. Block, T. Ciblac, and J. Ochsendorf, "Real-time limit analysis of vaulted masonry buildings," *Computers & Structures*, vol. 84, no. 29-30, pp. 1841-1852, 2006.
- [68] A. Avorio, A. Borri, and M. Corradi, "Comportamento dinamico di volte in muratura rinforzate con FRP-materials: primi risultati" in X Congresso Nazionale "L'ingegneria Sismica in Italia" ANIDIS, Potenza-Matera (Italy), 2001.
- [69] J. Jasienco, A. Di Tommaso, and L. Bednarz, "Experimental investigation into Collapse of Masonry Arches Reinforced Using Different Compatible Technologies," in MuRiCo3: Mechanics of masonry structures strengthened with composite materials, Venice (Italy), 2009.
- [70] S. Briccoli Bati, L. Rovero, and U. Toniatti, "Strengthening Masonry Arches with Composite Materials," *Journal of Composites for Construction*, vol. 11, no. 1, pp. 33-41, 2007.
- [71] P. Girardello, "Rinforzo di volte in muratura con materiali compositi innovativi," Ph.D. Thesis, University of Brescia, 2013.
- [72] N. Taranu, G. Oprisan, M. Budescu *et al.*, "Improving structural response of masonry vaults strengthened with polymeric textile composite strips," in 3rd WSEAS international conference on

- Engineering mechanics, structures, engineering geology, Corfu Island (Greece), 2010.
- [73] A. Baratta, I. Corbi, O. Corbi *et al.*, "Experimental evidence of uncertainty in seismic response of masonry vaults," in 14th World Conference on Earthquake engineering, Beijing (China), 2008.
- [74] M. Valluzzi, D. Oliveira, A. Caratelli *et al.*, "Round Robin Test for composite-to-brick shear bond characterization," *Materials and Structures*, vol. 45, no. 12, pp. 1761-1791, 2012/12/01, 2012.
- [75] UNI, "Prodotti di laterizio per murature. Metodi di prova (in Italian)," 1986.
- [76] EN, "Methods of test for masonry units -Part 1: Determination of compressive strength," 2002.
- [77] UNI-EN, "Specifiche per malte per opere murarie - Parte 2:Malte per muratura (in Italian)," 2010.
- [78] UNI-EN, "Metodi di prova per malte per opere murarie - Parte 11: determinazione della resistenza a flessione e a compressione della malta indurita (in Italian)," 2007.
- [79] UNI, "Prove sui calcestruzzi. Determinazione del modulo elastico secante a compressione (in Italian)," 1976.
- [80] J. Manie, and W. P. Kikstra, *DIANA Finite Element Analysis: User's Manual release 9.4.4*, Delft (NL) TNO Building and Construction Research, 2014.
- [81] IMIT, *D.M. 14.01.2008: Norme Tecniche per le Costruzioni (In Italian)*, Italian Ministry of Infrastructures and Transportation, Rome, 2008.
- [82] CEN, *Eurocode 3: Design of steel structures - Part 1-8: Design of joints*, CEN Technical Committee 250 (CEN/TC250), 2003.
- [83] CSI, "SAP 2000: Linear and Nonlinear Static and Dynamic Analysis of Three Dimensional Structures," 2010.
- [84] G. Maddaloni, K. P. Ryu, and A. M. Reinhorn, "Simulation of floor response spectra in shake table experiments," *Earthquake Engineering & Structural Dynamics*, vol. 40, no. 6, pp. 591-604, 2011.
- [85] J. M. Bracci, A. M. Reinhorn, and J. B. Mander, *Seismic Resistance of Reinforced Concrete Frame Structures Designed Only for Gravity Loads-Part III: Exp Performance and Analytical Study of a Model*, State University of New York at Buffalo, Buffalo, New York (USA), 1992.
- [86] P. B. Lourenço, "Computational strategies for masonry structures," Ph.D., Delft University of Technology, Delft (NL), 1996.
- [87] O. Zienkiewicz, R. Taylor, and J. Zhu, *The Finite Element Method, its Basis and Fundamentals*, 6th Edition ed., Oxford (UK): Elsevier, 20058.

- [88] F. Fouchal, F. Lebon, and I. Titeux, "Contribution to the modelling of interfaces in masonry construction," *Construction and Building Materials*, vol. 23, no. 6, pp. 2428-2441, 6//, 2009.

Appendix A

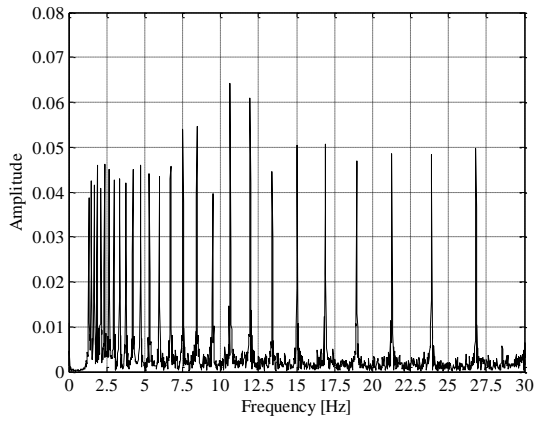


Figure A.1 FFT of the achieved input signals: test ART5

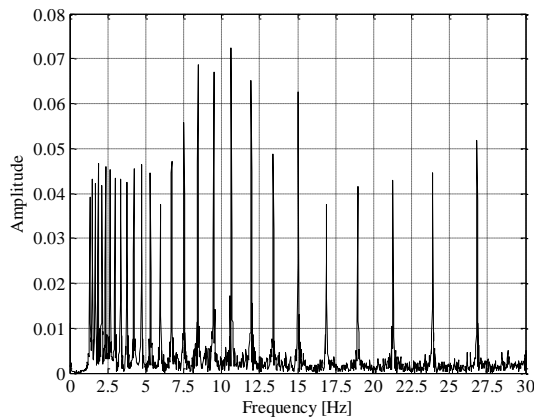


Figure A.2 FFT of the achieved input signals: test ART5_R

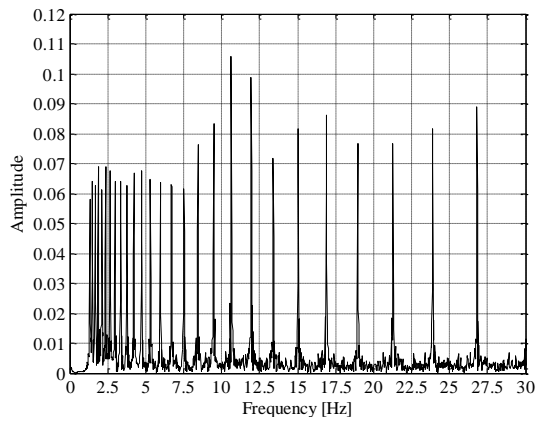


Figure A.3 FFT of the achieved input signals: test ART6

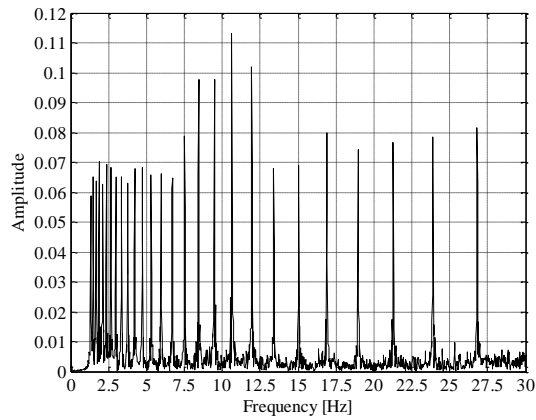


Figure A.4 FFT of the achieved input signals: test ART6_R

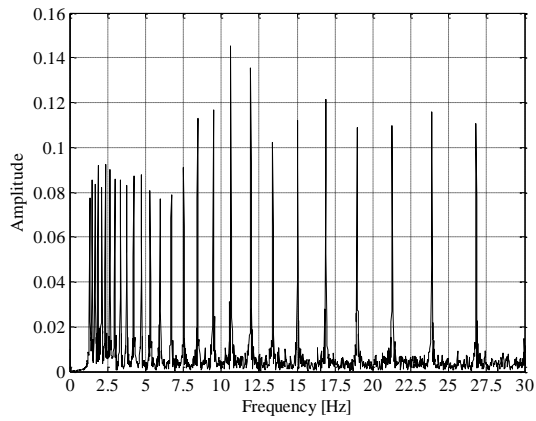


Figure A.5 FFT of the achieved input signals: test ART7

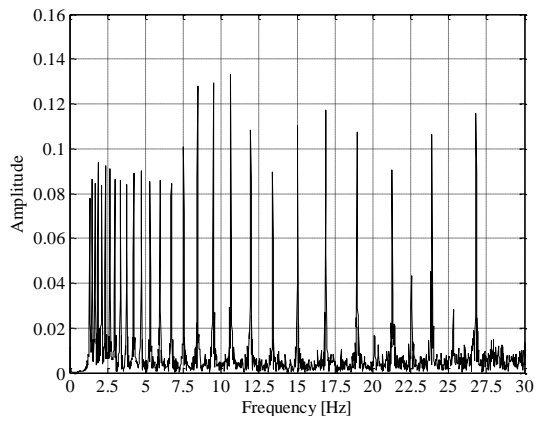


Figure A.6 FFT of the achieved input signals: test ART7_R

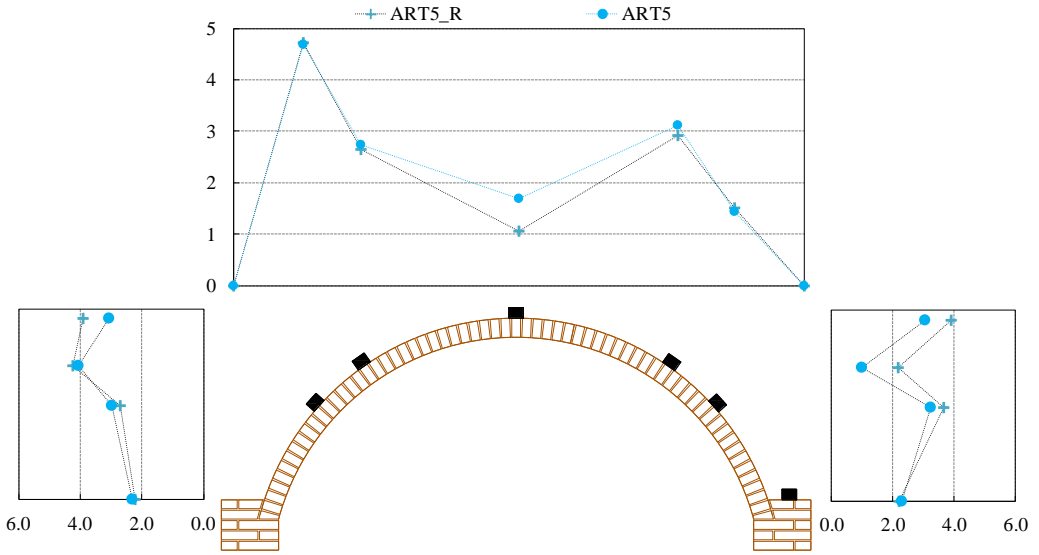


Figure A.7 Maximum acceleration profiles comparison: ART5-ART5_R
(values expressed in m/s^2)

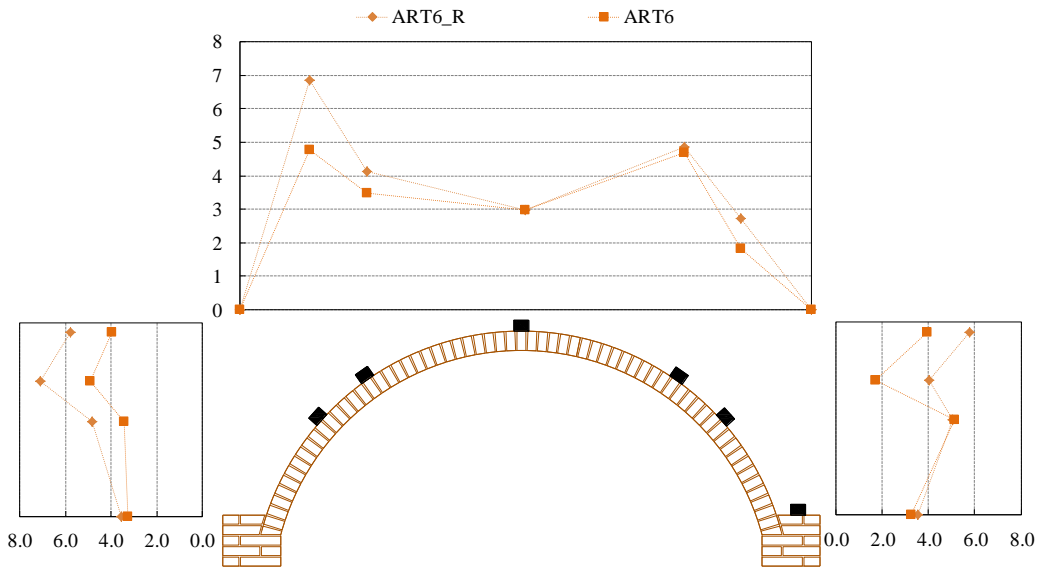


Figure A.8 Maximum acceleration profiles comparison: ART6-ART6_R
(values expressed in m/s^2)

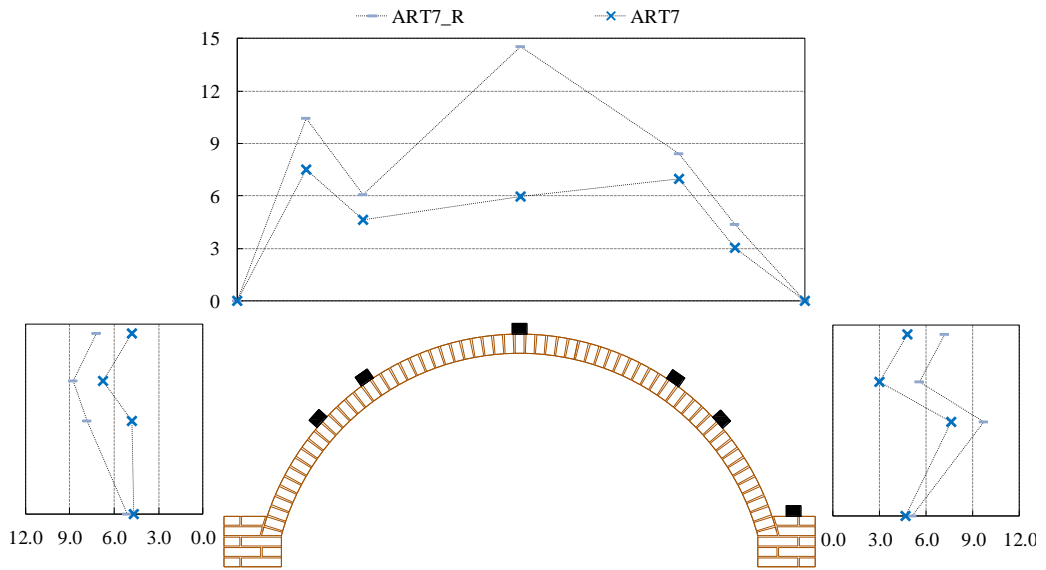


Figure A.9 Maximum acceleration profiles comparison: ART7-ART7_R
(values expressed in m/s^2)

Appendix B

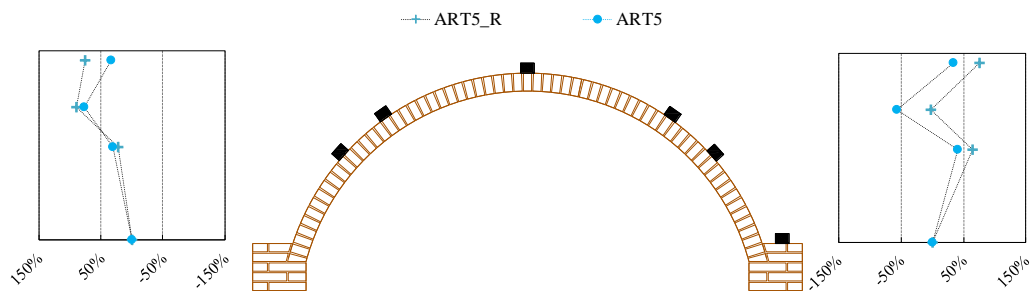


Figure B.1 Dynamic amplification profiles comparison: ART5-ART5_R
(values expressed in %).

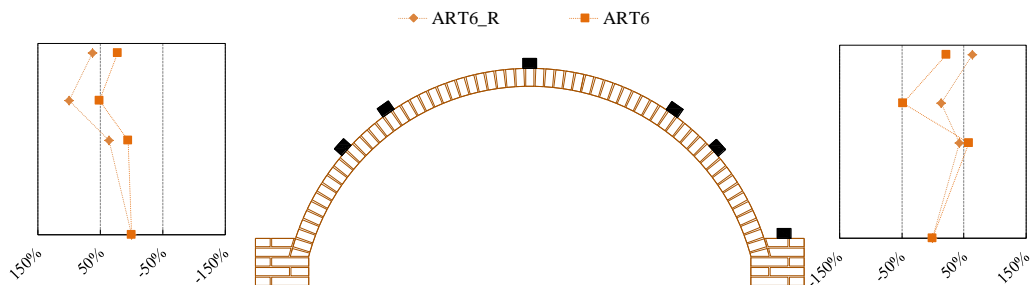


Figure B.2 Dynamic amplification profiles comparison: ART6-ART6_R
(values expressed in %).

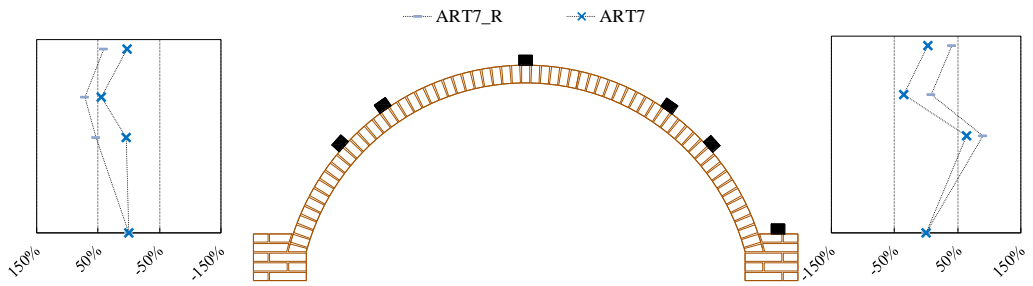


Figure B.3 Dynamic amplification profiles comparison: ART6-ART6_R (values expressed in %).

Appendix C

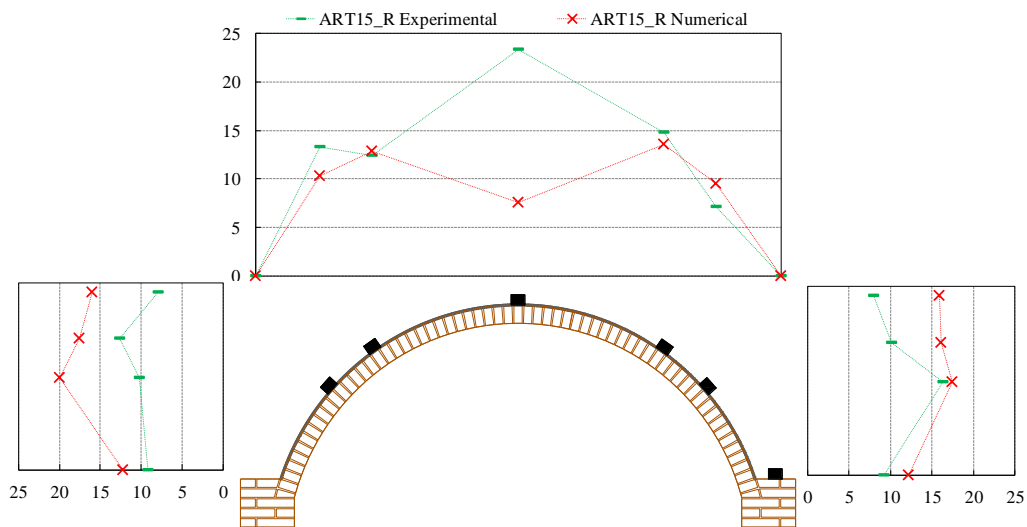


Figure C.1 Experimental-numerical comparison test ART15_R: Maximum acceleration profiles (values expressed in m/s^2)

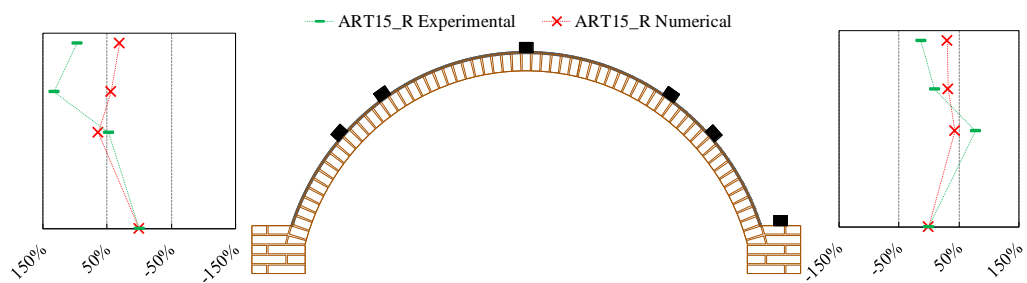


Figure C.2 Experimental-numerical comparison test ART15_R: Dynamic amplification profiles (values expressed in %).

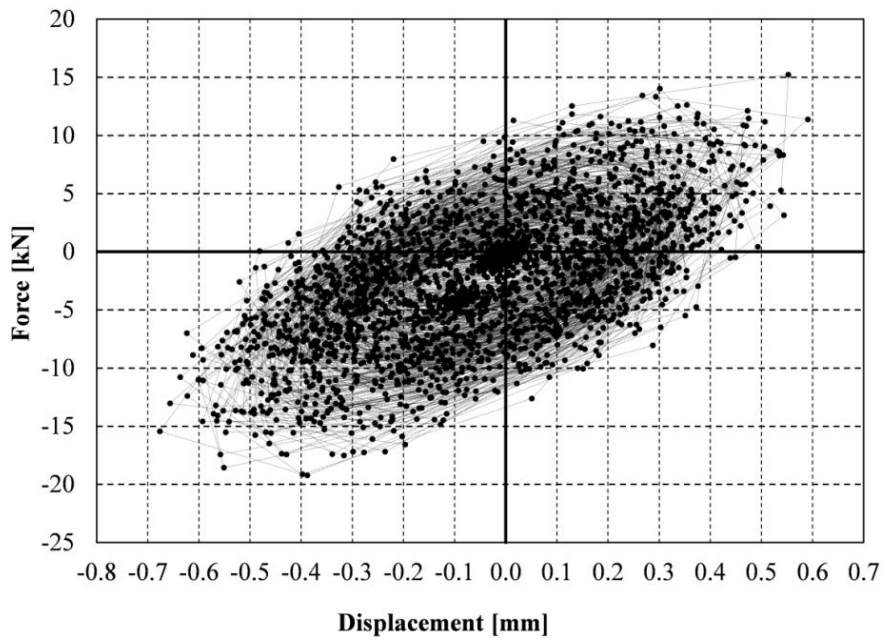


Figure C.3 ART15_R: numerical force-displacement trend